On the rare-earth-based intermetallic compounds for magnetocaloric hydrogen liquefaction: a matter of performance and criticality

zur Erlangung des akademischen Grades Doktoringenieur (Dr. Ing.)
Genehmigte Dissertation von Wei LIU aus Hubei, China
Tag der Einreichung: 17. Mai 2024, Tag der Prüfung: April 29, 2024

1. Gutachten: Prof. Dr. Oliver Gutfleisch
2. Gutachten: Prof. Dr. Hongbin Zhang
Darmstadt, Technische Universität Darmstadt

TECHNISCHE UNIVERSITÄT DARMSTADT

Materials Science
TU Darmstadt
Functional Materials

On the rare-earth-based intermetallic compounds for magnetocaloric hydrogen liquefaction: a matter of performance and criticality

Accepted doctoral thesis by Wei LIU

Date of submission: May 17, 2024
Date of thesis defense: April 29, 2024

Darmstadt, Technische Universität Darmstadt

For my families!

Erklärungen laut Promotionsordnung

§ 8 Abs. 1 lit. c PromO

Ich versichere hiermit, dass die elektronische Version meiner Dissertation mit der schriftlichen Version übereinstimmt.

§ 8 Abs. 1 lit. d PromO

Ich versichere hiermit, dass zu einem vorherigen Zeitpunkt noch keine Promotion versucht wurde. In diesem Fall sind nähere Angaben über Zeitpunkt, Hochschule, Dissertationsthema und Ergebnis dieses Versuchs mitzuteilen.

§ 9 Abs. 1 PromO

Ich versichere hiermit, dass die vorliegende Dissertation selbstständig und nur unter Verwendung der angegebenen Quellen verfasst wurde.

§ 9 Abs. 2 PromO

Die Arbeit hat bisher noch nicht zu Prüfungszwecken gedient.

Darmstadt, 17. Mai 2024

W. Liu

Abstract

Hydrogen energy plays an essential role in transitioning to a climate-neutral society. Although important for the efficient use of hydrogen energy, liquid hydrogen is not economical enough for large-scale energy-related applications such as energy storage and hydrogen-powered vehicles. The reason for this is the low efficiency of the conventional liquefaction technologies that are based on Joule-Thomson expansion. As an emerging liquefaction technology based on the magnetocaloric effect (MCE), magnetocaloric (MC) hydrogen could be a "game changer" for the liquid hydrogen industry for its great potential to achieve higher efficiency. This thesis focuses on the magnetocaloric effects of rare-earth-based MC materials, as they are promising candidates for MC hydrogen liquefaction.

The first part of this work reveals a feature by a study on the heavy rare-earth Laves phases: Second-order MC materials can also achieve a giant MCE at low temperatures. Two trends have been summarized from an extensive literature review: (1) the maximum magnetic entropy change (ΔS_T) increases as the Curie temperature (T_C) decreases; (2) the maximum adiabatic temperature change (ΔT_{ad}) decreases near room temperature as the T_C decreases, but increases in cryogenic temperature range.

Although heavy rare-earth MC materials possess excellent ΔS_T and ΔT_{ad}, heavy rare earths are highly critical, questioning the feasibility of using heavy rare-earth alloys for large-scale MC hydrogen liquefaction applications. In contrast, the lower criticality of light rare-earth elements makes their alloys appealing. Based on the discovery that the maximum MCE becomes more pronounced toward lower T_C in cryogenic temperature range, a method of designing a light rare-earth Laves phase series for hydrogen liquefaction is developed: mixing different light rare-earth elements with different de Gennes factors at the rare-earth sublattice to adjust T_C. Successfully, light rare-earth-based (Pr, Ce)Al_2 and (Nd, Pr)Al_2 materials are developed, showing a competitive MCE that covers the temperature range of $77 \sim 20$ K.

Recognizing that second-order MC materials do not exhibit the same excellent ΔS_T near 77 K as they do near 20 K, studies are carried out on light rare-earth-based intermetallic compounds with a first-order phase transition. A large ΔS_T is discovered in Nd_2In. In particular, this compound demonstrates a first-order phase transition at approximately 108 K, with negligible thermal hysteresis. Further studies on Pr_2In reveal that the Debye temperature plays an important role in achieving a large ΔT_{ad}: materials with a higher Debye temperature tend to exhibit a larger ΔT_{ad}, especially in the cryogenic temperature range.

This thesis studies the MCEs of the heavy rare-earth Laves phases, the light rare-earth Laves phases with a second-order phase transition, and the light rare-earth-based first-order magnetocaloric materials—Nd_2In and Pr_2In. This work shows that maximum MCE becomes more pronounced as the T_C decreases in the cryogenic temperature range. The aim of this work is to reduce the criticality of the raw materials while maximizing the magnetocaloric performance.

Zusammenfassung

Wasserstoffenergie spielt eine wesentliche Rolle bei der Umstellung auf eine klimaneutrale Gesellschaft. Obwohl flüssiger Wasserstoff wichtig für die effiziente Nutzung von Wasserstoffenergie ist, ist er für groß angelegte energierelevante Anwendungen wie Energiespeicherung und wasserstoffbetriebene Fahrzeuge nicht wirtschaftlich genug. Der Grund dafür ist die geringe Effizienz der konventionellen Verflüssigungstechnologien, die auf der Joule-Thomson-Expansion basieren. Als aufkommende Verflüssigungstechnologie basierend auf dem magnetokalorischen Effekt (MCE) könnte magnetokalorischer (MC) Wasserstoff ein "Game Changerfür die Flüssigwasserstoffindustrie sein, aufgrund seines großen Potenzials, eine höhere Effizienz zu erreichen. Diese Arbeit konzentriert sich auf die magnetokalorischen Effekte von seltenerdmetallbasierten MC-Materialien, da sie vielversprechende Kandidaten für die MC-Wasserstoffverflüssigung sind.

Der erste Teil dieser Arbeit enthüllt ein Merkmal durch eine Studie über die schweren seltenerdmetallbasierten Laves-Phasen: MC-Materialien zweiter Ordnung können auch bei niedrigen Temperaturen einen riesigen MCE erreichen. Zwei Trends wurden aus einer umfangreichen Literaturübersicht zusammengefasst: (1) Die maximale magnetische Entropieveränderung nimmt zu, wenn die Curie-Temperatur abnimmt; (2) Die maximale adiabatische Temperaturänderung nimmt in der Nähe der Raumtemperatur ab, wenn die Curie-Temperatur abnimmt, steigt jedoch im kryogenen Temperaturbereich an.

Obwohl schwere seltenerdmetallbasierte MC-Materialien eine ausgezeichnete magnetische Entropieveränderung und adiabatische Temperaturänderung aufweisen, sind schwere Seltenerdmetalle hoch kritisch und stellen die Machbarkeit der Verwendung von Legierungen schwerer Seltenerdmetalle für groß angelegte MC-Wasserstoffverflüssigungsanwendungen in Frage. Im Gegensatz dazu macht die geringere Kritikalität der leichten Seltenerdmetalle ihre Legierungen attraktiv. Basierend auf der Entdeckung, dass der maximale MCE im kryogenen Temperaturbereich bei niedrigerer Curie-Temperatur ausgeprägter wird, wird eine Methode zur Gestaltung einer Laves-Phasen-Serie aus leichten Seltenerdmetallen für die Wasserstoffverflüssigung entwickelt: Mischen verschiedener leichter Seltenerdmetalle mit unterschiedlichen de-Gennes-Faktoren auf der Seltenerdmetall-Teilgitter, um die Curie-Temperatur anzupassen. Erfolgreich wurden Materialien auf Basis leichter Seltenerdmetalle wie $(Pr, Ce)Al_2$ und $(Nd, Pr)Al_2$ entwickelt, die einen wettbewerbsfähigen MCE zeigen, der den Temperaturbereich von 77 bis 20 K abdeckt.

Da Materialien zweiter Ordnung bei etwa 77 K nicht die gleiche ausgezeichnete magnetische Entropieveränderung aufweisen wie bei etwa 20 K, werden Studien an leichten seltenerdmetallbasierten intermetallischen Verbindungen mit einem Phasenübergang erster Ordnung durchgeführt. Eine große magnetische Entropieveränderung wird in Nd_2In entdeckt. Insbesondere zeigt diese Verbindung einen Phasenübergang erster Ordnung bei ungefähr 108 K, mit vernachlässigbarem thermischem Hystereseeffekt. Weitere Studien an Pr_2In zeigen, dass die Debye-Temperatur eine wichtige Rolle bei der Erzielung einer großen adiabatischen Temperaturänderung spielt: Materialien mit einer höheren Debye-Temperatur neigen dazu, eine größere adiabatische Temperaturänderung aufzuweisen, insbesondere im kryogenen Temperaturbereich.

Diese Arbeit untersucht die MCEs der schweren seltenerdmetallbasierten Laves-Phasen, der leichten seltenerdmetallbasierten Laves-Phasen mit einem Phasenübergang zweiter Ordnung und der leichten seltenerdmetallbasierten magnetokalorischen Materialien erster Ordnung — Nd_2In und Pr_2In. Diese Arbeit zeigt, dass der maximale MCE im kryogenen Temperaturbereich ausgeprägter wird, wenn die Curie-Temperatur abnimmt. Ziel dieser Arbeit ist es, die Kritikalität der Rohstoffe zu verringern, während die magnetokalorische Leistung maximiert wird.

Contents

1 Introduction

Discovered by Weiss and Picard in 1917 [1] , magnetocaloric effect (MCE) describes the temperature change of a magnetic material in response to a changing magnetic field [2]. Soon after the discovery, magnetic refrigeration, a cooling technology based on MCE, was developed to attain extremely low temperatures by Giauque [3], who received the Nobel Prize in chemistry in 1949 for this work [4].

In the present 21^{st} century, global climate change caused by greenhouse gas emissions threatens human civilization with grave consequences [5]. In response, the major economies around the world have set their decarbonization goals: EU and USA target the net-zero greenhouse gas emissions by 2050 latest [6, 7], and China by 2060 latest [6]. Driven by these commitments, our world is undergoing a great transition from a society based on fossil energy to a climate-neutral society based on renewable energies.

As an energy carrier [8], hydrogen is believed to be the fuel for the future [9]. When produced from renewable energies, green hydrogen is the cleanest fuel, emitting no carbon and no pollutants [10]. **Figure 1.1** pictures a climate-neutral society, where green hydrogen is used as a medium for energy storage, a chemical feedstock, and a fuel. In this society, hydrogen is critical for the efficient use of renewable energies [8].

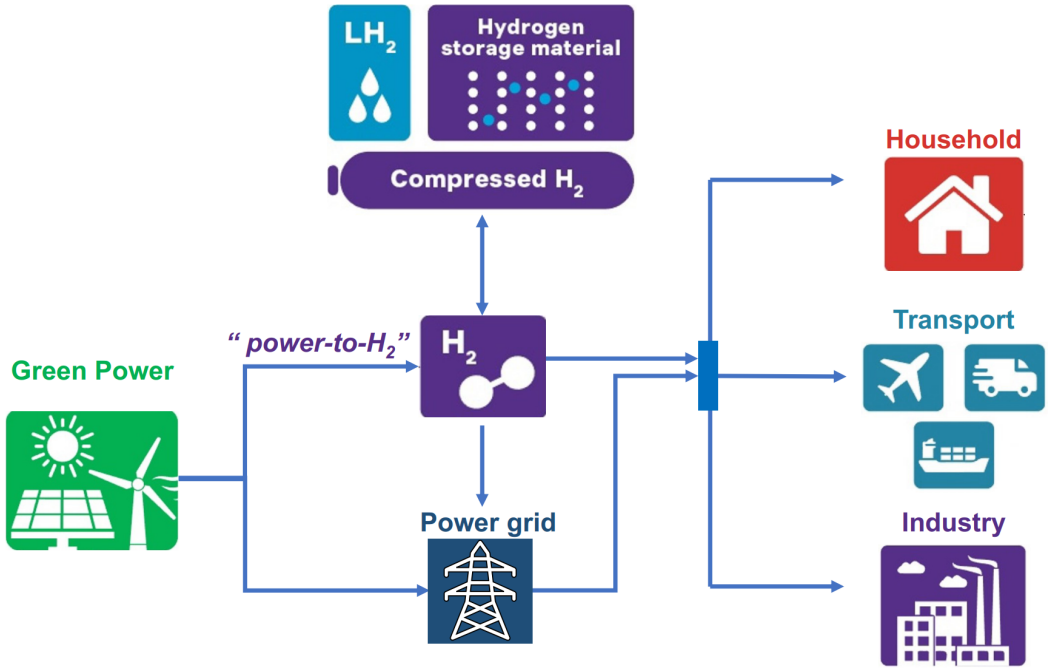

Figure 1.1: A carbon-neutral society where hydrogen plays a key role.

Hydrogen can be stored and transported efficiently in its liquid state [11]. However, liquefying hydrogen is expensive due to the low efficiency of the conventional liquefaction technologies which are based on the Joule-Thomson expansion [12]. The exergy efficiency of the most efficient industrial hydrogen liquefier ever reported is about 23% [13]. The low efficiency of liquefying hydrogen can lead to a loss of the energy content of the hydrogen fuel by up to 40% [14]. A feasibility study on a liquid hydrogen (LH_2) supply chain from Australia to Japan reveals that the highest cost comes from the liquefaction process, accounting for one third of the total cost, while hydrogen production makes up 29% [15].

Magnetocaloric (MC) gas liquefaction, an emerging cooling technology based on MCE, has been under intensive investigation as an alternative to conventional hydrogen liquefaction methods [16–20]. With its potential to significantly improve energy efficiency [21–25], MC hydrogen liquefaction could be a "game changer" for the liquid hydrogen industry. As revealed by Feng *et al.*, magnetocaloric hydrogen liquefaction can achieve an exergy efficiency of more than 60% [26], which is much higher than that achieved by the best industrial hydrogen liquefier mentioned above [13].

MC hydrogen liquefaction holds great promise; meanwhile, its successful implementation is fraught with challenges. **Figure 1.2** lists the requirements that are necessary for magnetic cooling technology [23]. As a subset of magnetic cooling technology, magnetocaloric hydrogen liquefaction technology also needs to meet these requirements. The most fundamental requirement is an affordable magnetocaloric material exhibiting large isothermal magnetic entropy and adiabatic temperature changes (ΔS_T and ΔT_{ad}) in an affordable magnetic field such as 2 T, which can be generated by Nd-Fe-B permanent magnets [27, 28], or 5 T, which can be generated by commercial superconducting magnets [29].

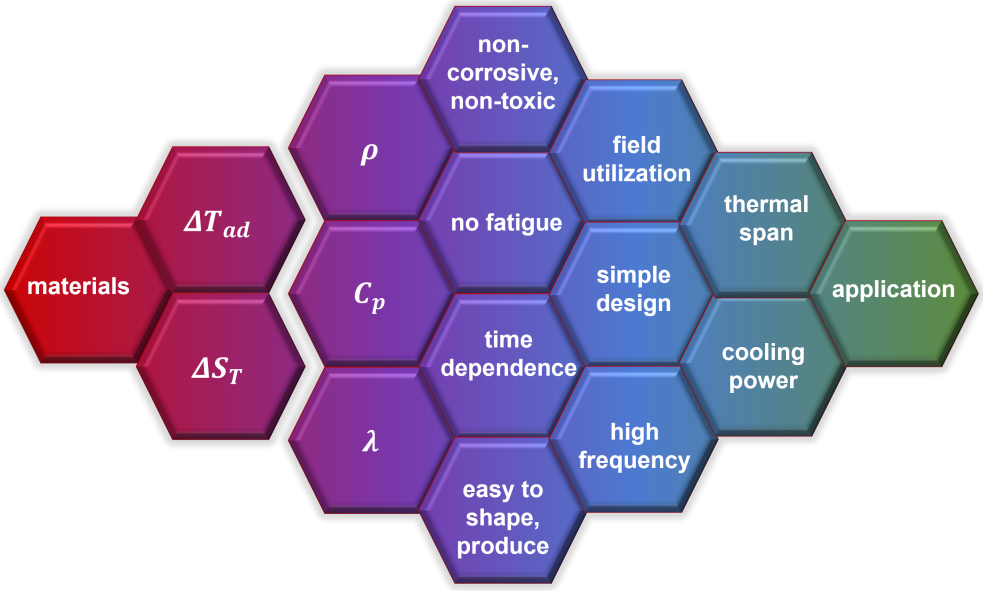

Figure 1.2: Illustration of the major requirements for magnetic cooling. ρ is the density, C_p is the isobaric heat capacity, and λ is the thermal conductivity. The left part denotes the challenges that this work focuses. The plot is adapted from reference [23].

If hydrogen gas is precooled by liquid nitrogen, magnetocaloric hydrogen liquefaction requires a temperature range of 77 $\sim$ 20 K (condensation point of nitrogen to condensation point of hydrogen) [30, 31]. Numerous magnetocaloric materials have been investigated for hydrogen liquefaction [31–36]. Notably, rare-earth-based intermetallic compounds exhibit a particularly promising MCE [37], demonstrating excellent

ΔS_T and ΔT_{ad} under affordable magnetic field changes such as 2 and 5 T.

Rare-earth elements are often classified into two main groups: light rare-earth elements (La, Ce, Pr, Nd, Sm) and heavy rare-earth elements (Y, Gd, Tb, Dy, Ho, Er, Tm. Yb, Lu) [38]. Heavy rare-earth-based alloys such as $ErCo_2$ [29], $HoAl_2$ [12], and $DyAl_2$ [35] are often proposed to be used in an active magnetic regenerator for hydrogen liquefaction due to their excellent MCEs at cryogenic temperatures. Compared to their light rare-earth-based counterparts, the heavy rare-earth-based alloys generally show a stronger MCE. The superior MCEs of the heavy rare-earth-based alloys over their light rare-earth-based counterparts are attributed to the fact that the heavy rare-earth ions from Gd^{3+} to Tm^{3+} possess magnetic moments greater than those of the light rare-earth ions [39].

However, heavy rare-earth elements such as Tb and Dy belong to highly critical metals, posing a challenge for large-scale applications [40]. In contrast, the relatively high abundances of the light rare-earth elements Pr and Nd make their alloys appealing for scaling up the magnetocaloric hydrogen liquefaction technology [40]. Many light rare-earth-based intermetallic compounds such as PrSi [41], NdSi [33] , $PrAl_2$ [42], $NdAl_2$ [42], Pr_2In [43], and Nd_2In [44] with a significant MCE in the temperature range of $20 \sim 77$ K have been successfully developed.

In short, magnetocaloric hydrogen liquefaction technology requires the design and optimization of magnetocaloric materials that meet both performance and price criteria. This thesis primarily investigates rare-earth-based intermetallic compounds for magnetocaloric hydrogen liquefaction, with emphasis on their magnetocaloric performance and the criticality of the rare-earth elements. In the following text, **Chapter 2** provides an overview of the fundamental knowledge for this thesis; **Chapter 3** describes the experimental methods employed in this thesis; Divided into four subsections, **Chapter 4** presents the results with discussions:

- The first subsection explores the MCEs of the heavy rare-earth-based Laves phases RAl_2 and RNi_2 (R: Gd, Tb, Dy, Ho, and Er) for magnetocaloric hydrogen liquefaction, leading to the discovery of the feature that the maximum ΔS_T and ΔT_{ad} can be "giant" in the vicinity of the hydrogen condensation point.

- The second subsection discusses a mean-field approach to demonstrate the feature mentioned above, and two increasing trends: both the maximum ΔS_T and ΔT_{ad} increase as Curie temperature (T_C) decreases.

- The third subsection focuses on designing light rare-earth-based magnetocaloric materials with second-order phase transitions covering the temperature range of $77 \sim 20$ K for hydrogen liquefaction.

- The magnetocaloric properties of the light rare-earth-based Nd_2In and Pr_2In alloys are discussed in the fourth subsection, with emphasis on their peculiar first-order phase transitions.

Chapter 5 sums up the present work and outlines potential directions for future studies on magnetocaloric materials for hydrogen liquefaction.

2 Fundamentals

2.1 Liquid hydrogen and history of gas liquefaction

Hydrogen, being the lightest element, boasts an impressive gravimetric energy density of 143 MJ kg^{-1}, making it the highest among all chemical fuels. This is approximately three times more than gasoline (42 MJ kg^{-1} to 44 MJ kg^{-1}) and diesel fuel (about 43 MJ kg^{-1}) [45]. However, the volumetric energy density of hydrogen gas is low due to its low density. Even compressed at 700 bar, H_2 only achieves a volumetric energy density of 5.6 MJ L^{-1} [46], far less than petrol (32.4 MJ L^{-1}) and diesel (36 MJ L^{-1}) [47]. In liquid form, the energy density of hydrogen is doubled to about 10 MJ L^{-1} [48]. Due to its higher energy density, liquid hydrogen is important for efficient storage and transportation of hydrogen energy.

However, with a condensation point of 20 K which is the second lowest among all the gases, hydrogen is difficult to be liquefied. Air, hydrogen, and helium cannot be liquefied at room temperature solely by compression like ammonia because of their low critical temperatures. This insight was recognized by the Irish physicist Thomas Andrews, who introduced the concept of critical temperature, above which a liquid and its vapor can coexist.

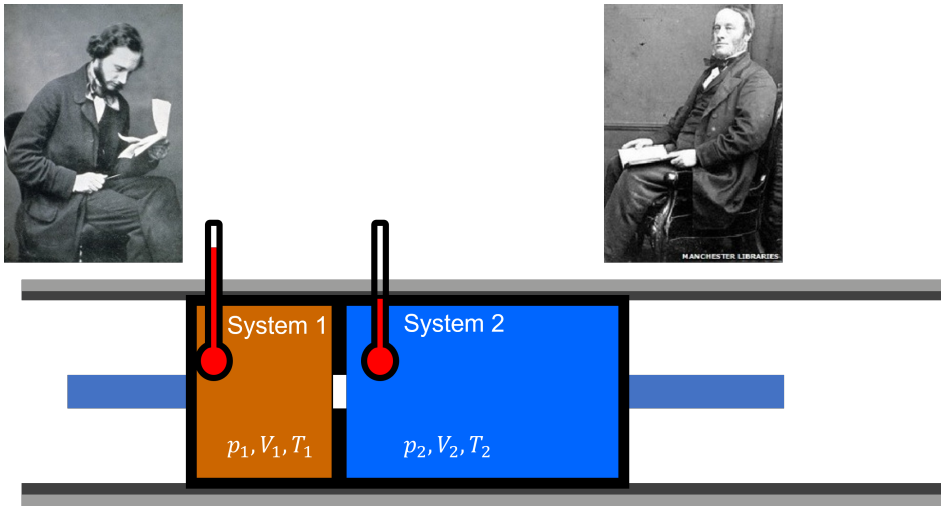

Figure 2.1: A plot illustrating the Joule-Thomson effect. The person on the left is William Thomson (Lord Kelvin), and the person on the right is James Joule. Photos are taken from [49].

As depicted in **Figure 2.1**, gas reduces its temperature when released from a compressed state to an expanded state. This phenomenon is known as the Joule-Thomson effect, discovered in 1852 by two British scientists James Joule and William Thomson (later known as Lord Kelvin). Serving as a fundamental principle

in conventional liquefaction technologies, Joule-Thomson expansion describes a thermodynamic process in which a gas or liquid at high pressure flows into a region of low pressure without a significant change in kinetic energy.

Nitrogen and oxygen, the two main components of Air, show critical temperatures of 126 and 154.4 K, respectively. These two values are much higher than that of hydrogen, which is 33 K, and that of helium, which is 13 K. Using the Joule-Thomson expansion and regenerative cooling, air was firstly liquefied in 1876 by German engineer Carl von Linde, who filed the patents of the Hampson-Linde cycle for the liquefaction of gases independently at the same time with British scientist William Hampson. Based on the Joule-Thomson expansion illustrated in **Figure 2.2**, the Hampson-Linde cycle is a keystone for gas liquefaction. Later in 1905, Linde obtained pure liquid oxygen and nitrogen.

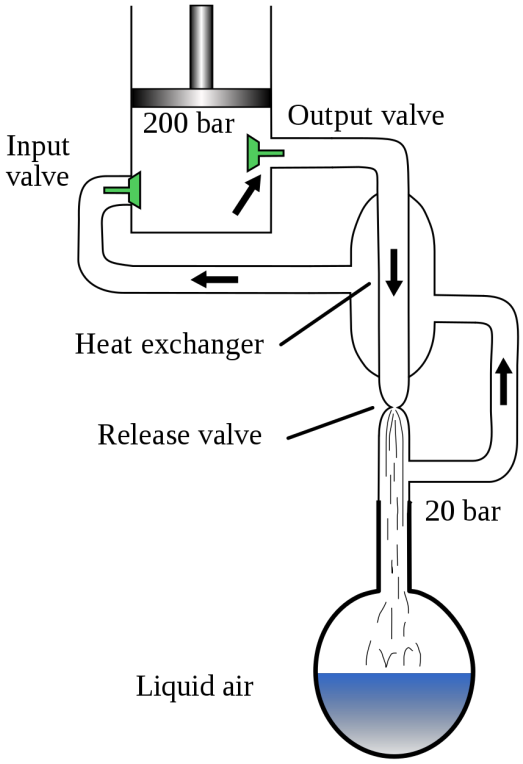

Figure 2.2: Schematic of simple Hampson-Linde cycle. This diagram was created by Martin Kossick and published under the Creative Commons Attribution-Share Alike 2.0 Germany.

More than twenty years after air was liquefied, James Dewar condensed liquid hydrogen by using regenerative cooling and his invention, the Dewar flask. Ten years later, helium was liquefied by Dutch physicist Heike Onnes, who also discovered superconductivity.

2.2 Magnetocaloric effect and magnetocaloric hydrogen liquefaction

Dating back to the year 1860, William Thomson made the prediction based on general thermodynamic considerations that iron at its Curie temperature would experience a cooling effect when moved away from a magnet and conversely a heating effect when moved toward a magnet [1]. About 60 years later, Weiss and his collaborator Picard discovered that Ni experiences a temperature rise of $0.7\,\mathrm{K}$ in a magnetic field of $1.5\,\mathrm{T}$, which they described as magnetocaloric effect [50].

Soon, Debye and Giauque independently realized that magnetocaloric effect could be used to achieve low temperatures using paramagnetic salts [51, 52]. Giauque and MacDougall built the first device that could reach a temperature below 1 K using $Gd_2(SO_4)_3 \cdot 8\,H_2O$ [3], a milestone of both low-temperature physics and magnetic cooling. In 1949, the Nobel Prize went to Giauque for his contributions to the studies on the properties of matter at temperatures close to absolute zero [4]. The next milestone of magnetic cooling was Brown's introduction of the first magnetocaloric demonstrator that worked at room temperature using Gd as refrigerant under a magnetic field of 7 T generated by a superconducting solenoid in 1976 [53]. Later, in 1982, the active magnetic regenerator (AMR), the most prototypical device used nowadays, was built, which developed a temperature gradient in the magnetocaloric materials during operation [54]. In recent years, several prototypes for gas liquefaction were introduced, such as AMR liquefiers for propane by Barclay *et al.* [55], for methane by Archipley *et al.* [56], and for hydrogen by Kamiya et al [29].

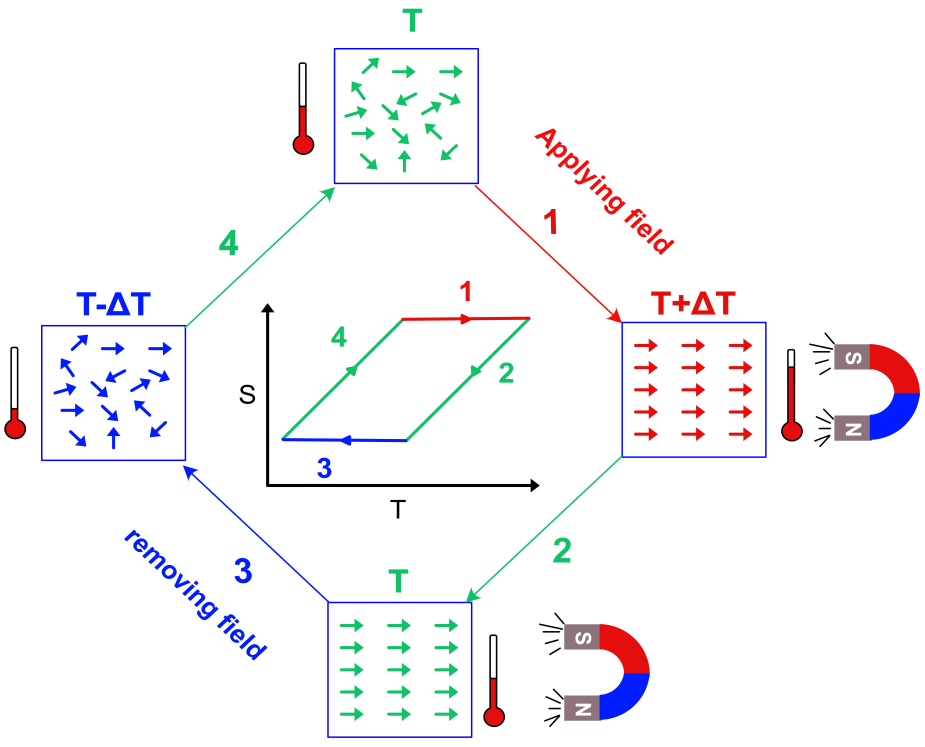

Figure 2.3: Illustration of a magnetic cooling cycle and the entropy curve during cycling.

Figure 2.3 illustrates the operational principle of magnetic refrigeration. A conventional magnetic cooling cycle involves four stages. First, the magnetocaloric materials are magnetized adiabatically by applying a magnetic field. Under adiabatic conditions, the total entropy S_{tot} remains unchanged, but the magnetic

entropy S_M decreases. To compensate the decrease of S_M, lattice entropy S_L increases, leading to a rise of the temperature of the magnetocaloric materials. Next, the heat generated during the adiabatic magnetization process is expelled by the exchanged fluid. Then, the magnetocaloric materials are demagnetized adiabatically by removing the magnetic field. Again, S_{tot} does not change, whereas S_M increases and S_L decreases, causing the temperature of the magnetocaloric materials to decrease. In the final stage, the magnetocaloric materials absorb heat from the surroundings until the system returns to its original state. An inverse magnetic cooling cycle works similarly but in a converse way. The inverse magnetocaloric materials increase their temperatures upon magnetization and decrease their temperatures upon demagnetization.

Magnetocaloric gas liquefaction is a subset of magnetic cooling technology. **Figure 2.4** schematically plots a magnetocaloric hydrogen liquefaction device. Hydrogen gas is firstly cooled down to 77 K by liquid nitrogen. The active magnetic regenerator (AMR) further cools the hydrogen gas below its condensation point (20 K), where liquid hydrogen is formed. Helium is the heat transfer fluid.

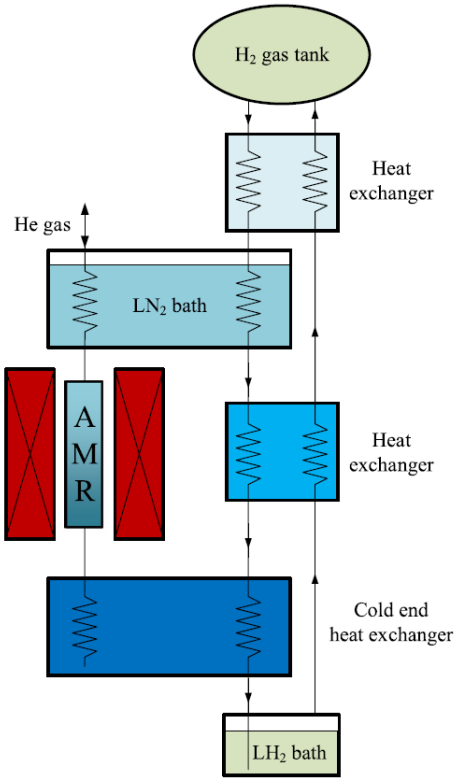

Figure 2.4: Illustration of a magnetocaloric hydrogen liquefaction device. Picture is taken from [57].

2.3 Thermodynamics of magnetocaloric effect

2.3.1 Entropy

Entropy S is one of the most fundamental concepts of a thermodynamic system. The total entropy S_{tot} of a magnetocaloric material is made up of three components: the lattice entropy S_L , the magnetic entropy S_M , and the electronic entropy S_e:

$$S_{tot} = S_L(T) + S_M(T, H) + S_e(T)\,, \tag{2.1}$$

where T is the temperature, H is the magnetic field. S_L and S_e are assumed to be independent on the magnetic fields. By integrating the heat capacity C' over temperature, the corresponding entropy S' can be obtained via:

$$S' = \int_0^T \frac{C'}{T} dT\,. \tag{2.2}$$

The electronic heat capacity C_e can be expressed as:

$$C_e = \gamma T\,, \tag{2.3}$$

where γ is the electronic specific heat coefficient. Therefore, electronic entropy S_e can be obtained by eq. (2.2):

$$S_e = \gamma T\,. \tag{2.4}$$

Under isochoric conditions, the volumetric lattice heat capacity S_L can be estimated using the Debye model, given by:

$$C_L = 9Nk_B \left(\frac{T}{T_D}\right)^3 \int_0^{\frac{T_D}{T}} \frac{x^4 e^x}{(e^x - 1)^2} dx\,, \tag{2.5}$$

where N is the total number of the atoms, k_B is the Boltzmann constant, T_D is the Debye temperature, and x is a variable on the interval $(0, T_D/T)$. Using eq. (2.2), the lattice entropy S_L is given by:

$$S_L = -3Nk_B \ln\left[1 - \exp\left(-\frac{T_D}{T}\right)\right] + 12Nk_B \left(\frac{T}{T_D}\right)^3 \int_0^{\frac{T_D}{T}} \frac{x^3}{\exp(x) - 1} dx\,. \tag{2.6}$$

Considering a canonical ensemble, its partition function is:

$$Z = \sum_n \exp\left(-\frac{E_n}{k_B T}\right)\,, \tag{2.7}$$

where E_n is the eigenvalue of the Hamiltonian $\hat{H}$ of the system. For a system containing one paramagnetic atom, $\hat{H}$ takes the form:

$$\hat{H} = -\hat{M}_J \mu_0 \overrightarrow{H}\,, \tag{2.8}$$

where $\overrightarrow{H}$ is the vector of the magnetic field, μ_o is the vacuum permeability and $\hat{M}$ is the atom magnetic moment operator given by:

$$\hat{M}_J = g_J\, \mu_B \hat{J}\,, \tag{2.9}$$

with g_J being the Landé g-factor, μ_B the Bohr magneton, and $\hat{J}$ the total angular momentum operator. The magnetic moment of an atom is $M_J = g_J \mu_0 \mu_B J$, where J is the total magnetic momentum number. The

projection of J along the magnetic field is m, taking the values $J, J-1, ..., -J$. Therefore, the eigenvalue of $\hat{H}$ is

$$E_m = -g_J \, \mu_B \, m\mu_0 \, H \, . \tag{2.10}$$

Let

$$y = \frac{M_J \mu_0 H}{k_B T} \, , \tag{2.11}$$

then

$$\begin{aligned} Z(y) &= \sum_{m=-J}^{J} \exp\left(\frac{my}{J}\right) \\ &= \frac{\sinh\left(\frac{2J+1}{2J}y\right)}{\sinh\left(\frac{1}{2J}y\right)} \, . \end{aligned} \tag{2.12}$$

Considering a system with N atoms, its partition function is $Z_N(y) = (Z(y))^N$. Knowing the partition function of a canonical system, the free energy F is given by:

$$\begin{aligned} F &= -k_B \, T \ln(Z_N(y)) \\ &= -N \, k_B \, T \ln(Z(y)) \, . \end{aligned} \tag{2.13}$$

The magnetic entropy S_M is given by:

$$\begin{aligned} S_M(T,H) &= -\frac{\partial F}{\partial T} \\ &= N \, k_B \left[\ln \frac{\sinh\left(\frac{2J+1}{2J}y\right)}{\sinh\left(\frac{1}{2J}y\right)} - y B_J(y) \right] \, , \end{aligned} \tag{2.14}$$

where $B_J(y)$ is the Brillouin function.

Now, considering a canonical system containing ferromagnetic atoms, we need to consider the internal contribution of $n_w M$ (n_w is the Weiss coefficient, and M is the magnetization) to the magnetic field. M can be expressed as:

$$\begin{aligned} M &= N M_J B_J(y) \\ &= N g_J \, \mu_B \, J B_J(y) \, . \end{aligned} \tag{2.15}$$

The Weiss coefficient n_w can be calculated via:

$$n_w = \frac{3 k_B \, T_C}{N \mu_0 \, g_J^2 \, \mu_B^2 \, J(J+1)} \, . \tag{2.16}$$

Knowing M and n_w, y can be expressed as:

$$\begin{aligned} y &= \frac{M_J \mu_0 (H + n_w M)}{k_B T} \\ &= \frac{g_J \, J \, \mu_B \, \mu_0 \, H + \frac{3J}{J+1} k_B \, T_C \, B_J(y)}{k_B \, T} \, . \end{aligned} \tag{2.17}$$

2.3.2 Isothermal magnetic entropy change and adiabatic temperature change

The isothermal magnetic entropy and adiabatic temperature changes (ΔS_T and ΔT_{ad}) are two key parameters for MCE. As illustrated in **Figure 2.5** (a) , ΔS_T and ΔT_{ad} can be obtained by constructing the total entropy $S_{tot}(T, H)$ curves, with

$$\begin{aligned} \Delta S_T(T, H) &= S_{tot}(T, H) - S_{tot}(T, 0)\,, \\ \Delta T_{ad}(T, H) &= T(S_{tot}, H) - T(S_{tot}, 0)\,, \end{aligned} \tag{2.18}$$

where $T(S_{tot}, H)$ is the inverse function of $S_{tot}(T, H)$.

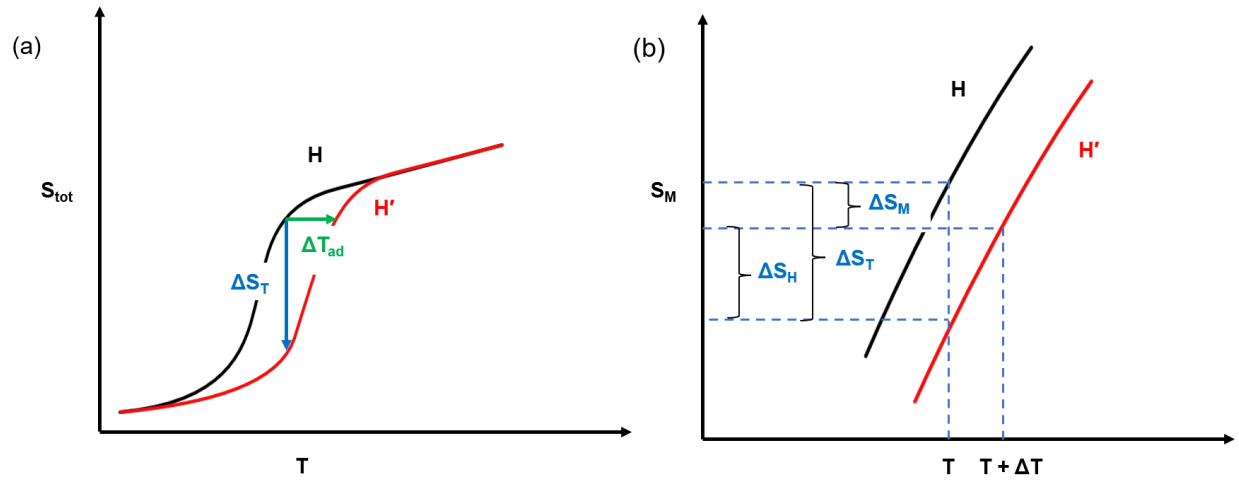

Figure 2.5: Schematic plot of the total entropy S_{tot} (a) and magnetic entropy S_M (b) with respect to T.

Considering a magnetization process, when the magnetic field H changes to H', a magnetocaloric material changes its temperature from T to T' in response. As illustrated in **Figure 2.5** (b), the total magnetic entropy change ΔS_M is:

$$\Delta S_M(T \to T', H \to H') = \Delta S_M(T, H \to H') + \Delta S_M(T \to T', H')\,. \tag{2.19}$$

$\Delta S_M(T, H \to H')$ is nothing but the isothermal magnetic entropy change ΔS_T, and $\Delta S_M(T \to T', H')$ is nothing but the isofield magnetic entropy change ΔS_H. If the magnetic heat capacity C_H is defined as:

$$C_H(T, H) = T\left(\frac{\partial S_M(T, H)}{\partial T}\right)_H\,, \tag{2.20}$$

ΔS_H can be calculated via:

$$\Delta S_H(T, H) = \int_T^{T'} \frac{C_H(T, H)}{T} dT\,. \tag{2.21}$$

Now, let's consider the total entropy change ΔS_{tot}. From 2.1, ΔS_{tot} is given by:

$$\begin{aligned} \Delta S_{tot} &= \Delta S_L + \Delta S_e + \Delta S_H + \Delta S_T \\ &= \int_T^{T'} \frac{C_L(T) + C_e(T) + C_H(T, H)}{T} dT + \Delta S_T \\ &= \int_T^{T'} \frac{C_{tot}}{T} dT + \Delta S_T\,, \end{aligned} \tag{2.22}$$

where C_{tot} is the total heat capacity.

Under isothermal conditions, ΔS_L, ΔS_e, ΔS_H are zero, hence, $\Delta S_T = \Delta S_{tot}$.

Under adiabatic conditions, the total entropy change $\Delta S_{tot} = 0$. Therefore,

$$0 = \frac{C_L(T) + C_e(T) + C_H(T,H)}{T} dT + dS_T \,. \tag{2.23}$$

This leads to

$$dT = -\frac{T dS_T}{C_{tot}(T,H)} \,. \tag{2.24}$$

As a result, adiabatic temperature change ΔT_{ad} can be estimated by

$$\Delta T_{ad} = -\frac{T \Delta S_T}{C_{tot}(T,H)} \,. \tag{2.25}$$

The analyses above built a connection between the total heat capacity C_{tot}, the isothermal magnetic entropy change ΔS_T, and the adiabatic temperature change ΔT_{ad}. Besides eq. (2.18), ΔS_T can also be obtained from magnetization measurement via Maxwell relations. The Gibbs free energy G of a magnetic material can be written as:

$$G = U - TS + pV - \mu_0 m(T,H) H \,, \tag{2.26}$$

where $m(T,H)$ is the magnetic moment at temperature T in magnetic fields of H, and U is the internal energy. The total differential of the Gibbs free energy can be derived as:

$$\begin{aligned} \left(\frac{\partial G}{\partial T}\right)_H &= -S(T,H) \,, \\ \left(\frac{\partial G}{\partial H}\right)_H &= -\mu_0 \, m(T,H) \,, \end{aligned} \tag{2.27}$$

Since the second order partial derivative of G does not depend on the order of T and H, $\partial G/(\partial T \, \partial H) = \partial/(\partial H \, \partial T)$. This gives:

$$\frac{dS(T,H)}{dH} = \frac{\mu_0 \, dm(T,H)}{dT} \,. \tag{2.28}$$

In experiment, conventionally entropy is given in units of $\mathrm{J\,kg^{-1}\,K^{-1}}$, and m is given in units of $\mathrm{A\,m^2\,kg^{-1}}$, which is M. From now on, only the specific variables of entropy and m are considered. From eq. (2.28), we can calculate the isothermal magnetic entropy change ΔS_T by:

$$\Delta S_T(T,H) = \mu_0 \int_0^H \left(\frac{\partial M}{\partial T}\right)_H dH \,. \tag{2.29}$$

From eq. (2.24), adiabatic temperature change ΔT_{ad} can be calculated via:

$$\Delta T_{ad} = -\mu_0 \int_0^H \frac{T}{C_{tot}(T,H)} \left(\frac{\partial M}{\partial T}\right)_H dH \,. \tag{2.30}$$

2.3.3 Clausius-Clapeyron equation

For first-order phase transition (detailed discussion on nature of phase transition is in **Section 2.4.1**), ideally the magnetization during phase transition jumps abruptly. This is to say, the derivative dM/dT does not exist. In this sense, eq. (2.29) is not valid for first-order phase transition. However, since dM/dT is not an ideal step-like jump but a rather smooth increase in reality, this equation is still applicable to first-order phase transition [58].

The magnetocaloric effect of first-order magnetocaloric materials can also be estimated by the Clausius-Clapeyron equation. Under constant H and pressure and neglecting the volume change, G is a continuous function with respect to T. Using the superscript l to denote that the material is in low temperature phase, and superscript h to denote the high temperature phase, at transition temperature T_t,

$$G^l(T_t, H) = G^h(T_t, H)\,. \tag{2.31}$$

Assuming U^l, U^h, S^l, S^h, m^l, and m^h do not change with transition temperature T_t and magnetic field H, which means that the magnetic field only shifts the transition temperature without changing the magnetization, the internal energy, and the entropy, in magnetic field H_1, eq. (2.31) can be written as:

$$U^l - T_t(H_1)\,S^l - \mu_0\,m^l\,H_1 = U^h - T_t(H_1)\,S^h - \mu_0\,m^h\,H_1\,. \tag{2.32}$$

And at magnetic field H_2, the transition temperature shifts from $T_t(H_1)$ to $T_t(H_2)$:

$$U^l - T_t(H_2)\,S^l - \mu_0\,m^l\,H_1 = U^h - T_t(H_2)\,S^h - \mu_0\,m^h\,H_1\,. \tag{2.33}$$

Subtracting the two equations results in

$$(S^l - S^h)(T_t(H_2) - T_t(H_1)) = \mu_0(m^h - m^l)(H_2 - H_1)\,. \tag{2.34}$$

Let $\Delta T_t = T_t(H_2) - T_t(H_1)$, $\Delta H = H_2 - H_1$, and $\Delta S_t = S^l - S^h$, this equation can be simplified into

$$\Delta S_t = -\mu_0 \Delta M \frac{\Delta H}{\Delta T_t}\,. \tag{2.35}$$

The assumptions made to obtain eq. (2.35) imply that the Clausius-Clapeyron equation can only estimate the magnetocaloric effect since U^l, U^h, S^l, S^h, m^l, and m^h change with H and T_t in reality. Besides, first-order phase transition usually associates with large volume changes, which is against the assumption that V stays constant across the phase transition. It should be emphasized that ΔS_t is the total isothermal entropy change, not the isothermal magnetic entropy change.

2.3.4 Figure of merit

To properly assess the suitability of magnetocaloric materials, a reliable figure of merit is required. A number of performance parameters, namely the refrigerant capacity (RC) [59], the materials efficiency (η) [60], relative cooling power (RCP) [61], and the temperature averaged entropy change (TEC) [62], the transferable heat (Q_{rev}) [23], are proposed as figure of merits.

As illustrated by **Fig. 2.6**, Proposed as the figure of merit for MCE by Wood and Potter, RC is defined as:

$$RC = \Delta S_C \, \Delta T \,, \tag{2.36}$$

where ΔS_C is the entropy absorbed per cycle by the refrigerant at the cold end, and ΔT is the temperature span over which the heat is pumped [59].

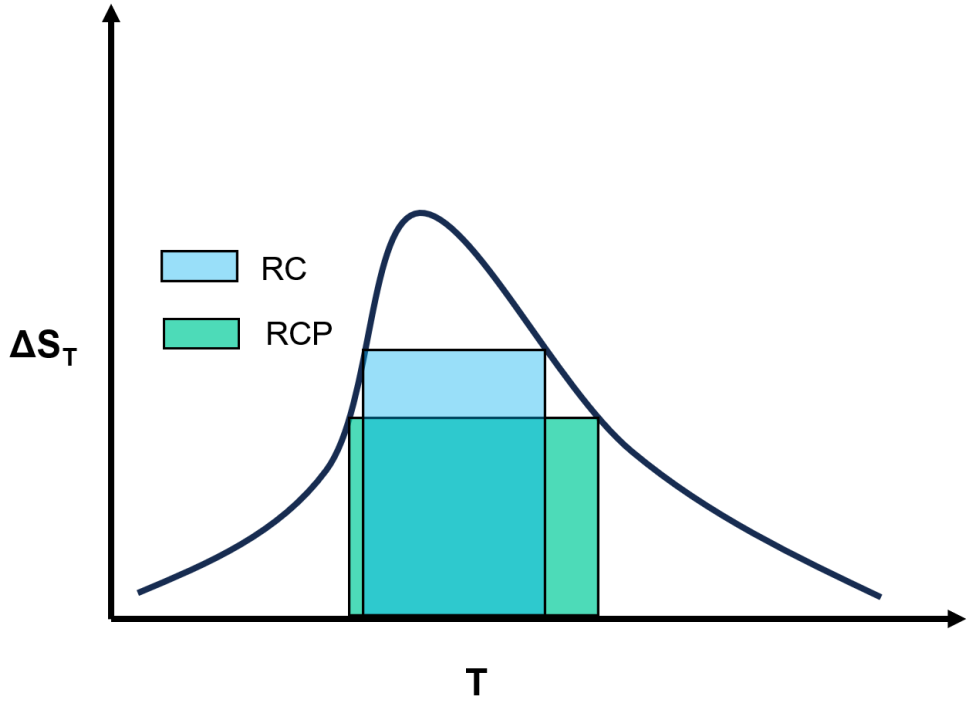

Figure 2.6: Schematic plot illustrating RC and RCP.

A similar concept is the RCP, which is

$$RCP = \Delta S_T^{max} \, \delta_{FWHM} \,, \tag{2.37}$$

where ΔS_T^{max} is the maximum isothermal magnetic entropy change, and δ_{FWHM} is the full width at half maximum of the $\Delta S_T(T)$ curve [63]. These two parameters, however, assume that the entire magnetocaloric material is at the same temperature, making it impossible to employ them directly in describing the performance of a magnetic regenerator, where there is a temperature gradient across the materials [63]. Another drawback of these two parameters is that they falsely suggest magnetocaloric materials with a $\Delta S_T(T)$ in a flat shape, making it a question whether they can sustain a cycle requiring a large temperature span [63].

The definition of the magnetocaloric efficiency is

$$\eta = \left| Q/W \right| , \tag{2.38}$$

where Q is the heat flowing from the cold bath to the hot bath in a thermodynamic cycle, and W is the work done to drive highly reversible caloric effects in an isothermal body [60]. As η undergoes a trivial increase with decreasing $|Q|$, it is only meaningful to make a comparison of η under similar values of $|Q|$ [60].

TEC and Q_{rev} are the newest performance parameters that are proposed as figure of merits for magnetocaloric materials. **Figure 2.7** (a) and (b) schematically plot these two figures of merit, respectively. The definition of TEC over a range of temperature ΔT_{lift} is

$$TEC(\Delta T_{lift}) = \frac{1}{\Delta T_{lift}} \underset{T_{mid}}{max} \left\{ \int_{T_{mid}-\frac{\Delta T_{lift}}{2}}^{T_{mid}-\frac{\Delta T_{lift}}{2}} \Delta S_T(T,H)\, dT \right\}, \tag{2.39}$$

where T_{mid} is the center of the average and is chosen to maximize TEC(ΔT_{lift}) for the given ΔT_{lift} [62]. The advantage of TEC over RC and RCP is to avoid overestimate the merit of materials with a very broad shape of $\Delta S_T(T)$ curve but a small peak values [59].

However, RC, RCP and TEC do not consider ΔT_{ad}, a magnetoclaoric parameter which is as important as ΔS_T. Meanwhile, the performance parameter Q_{rev} combines both ΔS_T and ΔT_{ad} by the equation

$$Q_{rev}(T, H, T_{hot} - T_{cool}) = \left| [S_{tot}(T_{cool}, 0) - S_{tot}(T_{hot}, H)] T_{cool} \right|, \tag{2.40}$$

where T_{hot} and T_{cool} are the temperatures of the hot and cold bathes, respectively [23].

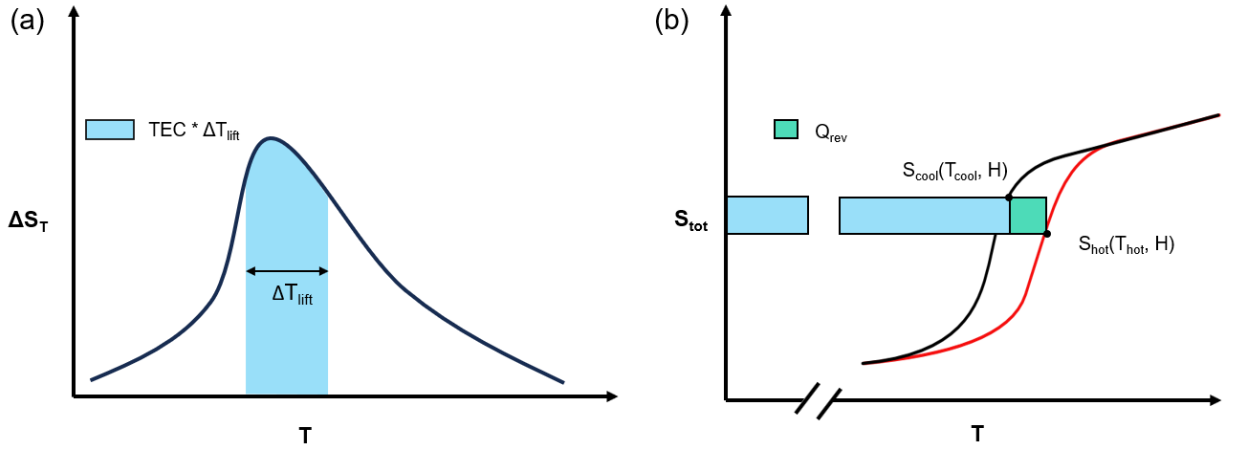

Figure 2.7: (a) Illustrations of TEC. Predefining a temperature width ΔT_{lift}, TEC is defined as the division of area in cyan under the $\Delta S_T(T)$ curves and ΔT_{lift}. (b) Illustration of reversible heat Q_{rev}, which is the area of the long rectangle in light blue.

2.4 Nature of phase transition in magnetocaloric materials

2.4.1 Phase transition order

Based on the behavior of the thermodynamic free energy as a function of other thermodynamic variables such as temperature or volume, phase transitions are classified by Ehrenfest into first-order phase transition and second-order phase transition. First-order phase transition exhibits a discontinuity in the first derivative of the free energy with respect to the other thermodynamic variables, while second-order phase transition shows a discontinuity in the second derivative. Based on the order of the magnetic phase transitions, magnetocaloric materials are categorized into first-order magnetocaloric materials and second-order magnetocaloric materials.

First derivative of Gibbs free energy G with respect to temperature under constant pressure gives the additive inverse of entropy

$$\left(\frac{\partial G}{\partial T}\right)_p = -S\,. \tag{2.41}$$

And the second derivative of G with respect to T under constant pressure gives heat capacity over T:

$$\left(\frac{\partial^2 G}{\partial T^2}\right)_p = -\frac{dS}{dT} = -\frac{C_p}{T}\,. \tag{2.42}$$

In a word, first-order phase transition exhibits a discontinuity in entropy while second-order phase transition shows a discontinuity in heat capacity. In an ideal case, the heat capacity of the first-order phase transition at transition temperature should go to infinity due to the discontinuity in entropy.

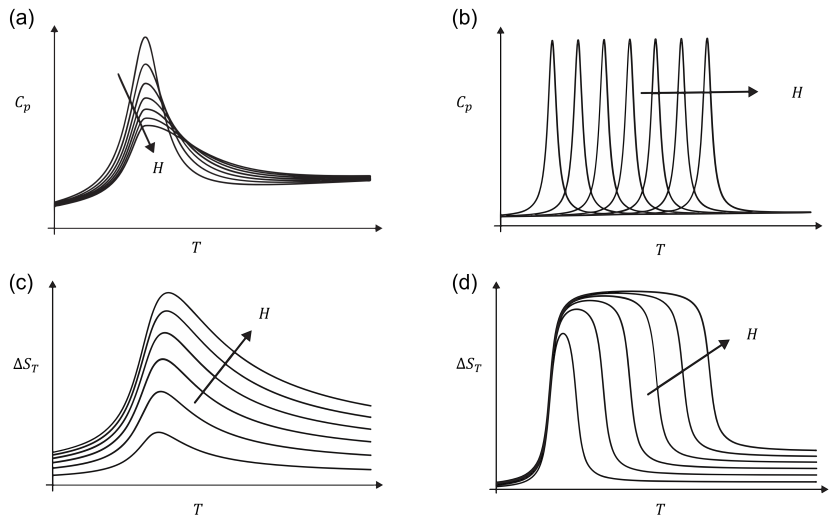

Figure 2.8: Illustrations of magnetic heat capacity C_H vs. T for second-order magnetocaloric materials (a) and first-order magnetocaloric materials (b), and magnetic entropy change ΔS_T vs. T for second-order magnetocaloric materials (c) and first-order magnetocaloric materials (d).

Figure 2.8 compares C_{tot}, ΔS_T , and ΔT_{ad} curves of first- and second order magnetocaloric materials. Generally speaking, first- and second- order magnetocaloric materials exhibit different characters in their

$C_p(T, H)$ and $\Delta S_T(T, H)$ curves [63]. For second-order magnetic phase transitions, C_p decreases gradually from a sharp peak in zero field to a flat peak in high fields, with the peak position weakly shifting to higher temperatures [63]. Meanwhile, C_p of first-order phase transitions usually shifts its peak significantly towards higher temperatures with increasing magnetic fields because magnetic fields stabilize ferromagnetic states [63]. $\Delta S_T(T)$ curve of second-order phase transitions increases in height and width, with the peak position weakly shifting to higher temperatures, whereas the peak of $\Delta S_T(T)$ curve of first-order phase transitions in high fields is not sensitive to field changes, but its width scales with magnetic fields [63].

However, in real cases, impurities and spatial variations in the stoichiometry spread out the transition and blur the first- and second- order phase transitions [63]. These features described above may not be enough to distinguish the nature of a phase transition. What constitutes a reliable experimental evidence of a first-order phase transition is still under debate [63]. Different methods may end up in different conclusions. A typical example is $PrCo_2$, Herrero-Albillos *et al.* state that this material undergoes a second-order phase transition based on calorimetry study [64, 65], whereas Forker *et al.* hold a different opinion that the phase transition of $PrCo_2$ is of first-order according to the measurements of the magnetic hyperfine interaction [66, 67].

2.4.2 Landau theory of phase transition

Landau theory is a theoretical framework used in condensed matter physics to describe the behavior of a system near phase transition. Free energy F as a function of order parameter can be determined by using symmetry arguments in Landau theory. For second-order phase transitions, F near phase transition temperature can be expanded as a function of an order parameter η in an external field μ as:

$$F = F_0 + \alpha\,\eta^2 + \beta\,\eta^4 - \mu\,\eta \tag{2.43}$$

α and β are temperature-dependent parameters with $\beta > 0$. α can be written as $\alpha = \alpha_0\,(T - T_C)$, where α_0 is a positive constant. A stable system requires $\delta F/\partial\eta = 0$, which gives

$$T = \frac{1}{2\alpha_0}\frac{\mu}{\eta} - \frac{2\beta}{\alpha_0}\eta^2 + T_C \tag{2.44}$$

For first-order phase transitions, F is expanded to η^6 as:

$$F = F_0 + \alpha\,\eta^2 + \beta\,\eta^4 + \gamma\,\eta^6 - \mu\,\eta \tag{2.45}$$

In this equation, α, β, and γ are temperature-dependent parameters with $\gamma > 0$. Again, for a stable system, the requirement of $\partial F/\partial\eta = 0$ leads to:

$$T = \frac{1}{2\alpha_0}\frac{\mu}{\eta} - \frac{2\beta}{\alpha_0}\eta^2 - \frac{3\gamma}{\alpha_0}\,\eta^4 + T_C \tag{2.46}$$

Figure 2.9 illustrates the order parameter as a function of temperature for first-order and second-order phase transitions. The order parameter of a first-order phase transition exhibits a thermal hysteresis, while no thermal hysteresis exists for a second-order phase transition.

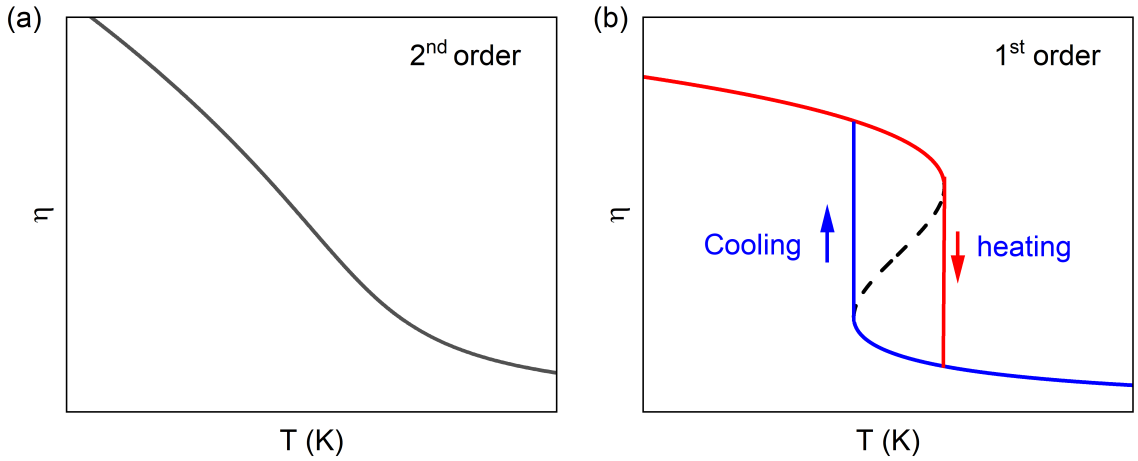

Figure 2.9: Schematic plots of order parameter η as a function of temperature for second-order phase transition without hysteresis (a) and first-order phase transition with thermal hysteresis (b).

2.4.3 Thermal hysteresis

As discussed above, thermal hysteresis is one of the characters of first-order phase transitions that distinguishes it from second-order phase transitions. Thermal hysteresis has a negative impact on the magnetocaloric properties, as it decreases the cyclic performance of first-order magnetocaloric materials. An example is $Ni_{45.7}Co_{4.2}Mn_{36.6}In_{13.5}$ reported by Gottschall *et al.* [68]. Upon first cycling, this material has an excellent ΔT_{ad} of -8 K near its ordering temperature under a magnetic field change of 1.95 T. However, ΔT_{ad} decreases to about -4 K upon second cycling. This severe deterioration of ΔT_{ad} for $Ni_{45.7}Co_{4.2}Mn_{36.6}In_{13.5}$ is due to its large thermal hysteresis of about 10 K.

Figure 2.10 illustrates how thermal hysteresis influences ΔS_T and ΔT_{ad} of first-order magnetocaloric materials, with second-order magnetocaloric materials as a comparison. As demonstrated in **Figure 2.10** (a), for second-order magnetocaloric materials, decreasing the temperature below T_C, a paramagnet becomes a ferromagnet. The magnetization increases because of the gradually ordered magnetic moments. Magnetic moments can also be aligned by the external magnetic field, resulting in increased magnetization. The magnetic moments become more ordered, relating to a decrease in magnetic entropy change. As a result, a decrease in the total entropy change is expected, as illustrated in **Figure 2.10** (b).

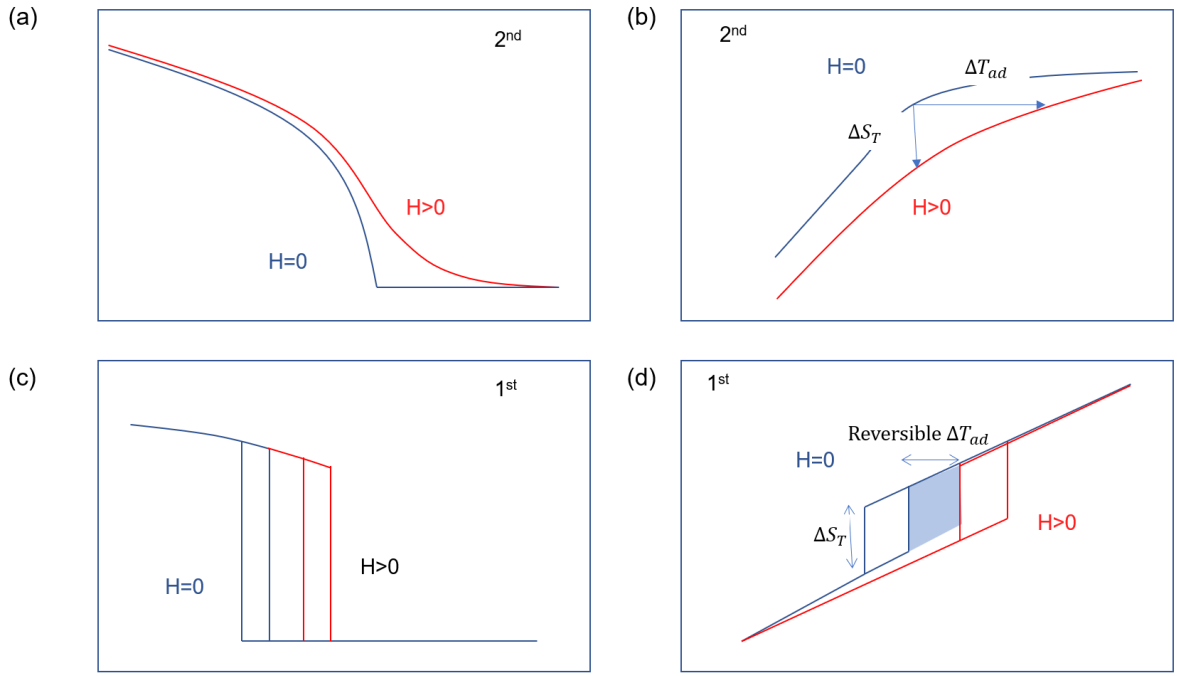

Figure 2.10: Schematic of the magnetization and total entropy change vs. T in magnetic fields of 0 and H for second-order phase transition (a, b), and for first-order phase transition (c, d). The light blue area in (d) marks the reversible region.

Unlike the gradually increasing magnetization for second-order phase transitions, decreasing the temperature below T_C or applying an external magnetic field results in an abrupt increase in magnetization, as illustrated in **Figure 2.10** (c). For conventional first-order magnetocaloric materials, their heat capacities shift to higher temperatures, as illustrated in **Figure 2.10** (d). Only in the region between the thermal hysteresis loops, MCE is fully reversible.

2.4.4 Numerical determination of phase transition order

Phase transition order can be determined by Arrott plot. Named after American physicist Anthony Arrott, an Arrott plot is a plot of the square of the magnetization (M^2) of a substance against the ratio of the applied magnetic field to magnetization (H/M) at one (or several) fixed temperature(s). Taking M as order parameter, and μ as magnetic field H, eq. (2.44) and eq. (2.46) can be re-written as

$$M^2 = \frac{1}{4\beta}\frac{H}{M} - \frac{\alpha_0}{2\beta}(T - T_C), \tag{2.47}$$

$$M^2 + \frac{3\gamma}{2\beta}M^4 = \frac{1}{4\beta}\frac{H}{M} - \frac{\alpha}{2\beta}(T - T_C). \tag{2.48}$$

Figure 2.11 (a) and (b) schematically show the Arrott plots of second-order phase transitions and first-order phase transitions. One of the feature of first-order phase transitions that distinguishes it from second-order phase transitions is the negative slope appearing in the Arrott plot, as displayed in **Figure 2.11** (b) for Arrott plot at T_0 and T_3. Although Arrott plot is widely used to determine the order of phase transitions, this method does not work well for the phase transitions near the boundary of first-order and second-order phase transitions.

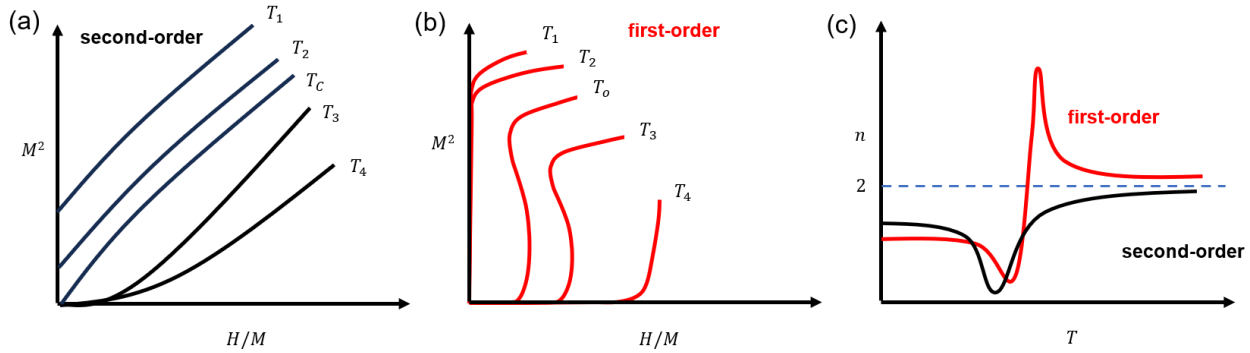

Figure 2.11: Schematic of the Arrott plots of the second-order phase transition (a) and the first-order phase transition (b). T_O is ordering temperature. (c) exponential n as a function of temperature for first-order and second-order magnetocaloric materials.

To avoid ambiguity in determining the order of the phase transition for magnetocaloric materials, Law *et al.* developed a quantitative criterion based on the scaling rule [69]:

$$\Delta S_T \propto H^n \tag{2.49}$$

For first-order phase transition, there is an overshot of n to 2, while for second-order phase transition, n is always below 2, as illustrated in **Figure 2.11** (c).

3 Experimental methods

3.1 Sample preparation

All the samples in this work were synthesized by arc melting. **Table 3.1** lists the compositions and the heat treatment methods of all the samples which are classified into second-order heavy rare-earth-based Laves phases, second-order light rare-earth-based Laves phases, and first-order light rare-earth-based R_2In (R: Pr, Nd) intermetallic compounds. Because the ingots of the heavy rare-earth RAl_2 and RNi_2 (R: Gd, Tb, Dy, Ho, and Er) and the light rare-earth (R, R')Al_2 (R, R': Ce, Pr, and Nd) Laves phases split into pieces under the arc, they were melted three times. The R_2In samples were melted five times. After each melting, the ingots were flipped for the next melting to ensure good homogeneity.

Table 3.1: List of samples synthesized in the present work.

Heavy rare-earth Laves phases with second-order phase transition			
Sample	Heat treatment	Sample	Heat treatment
$GdAl_2$	as-casted	$GdNi_2$	as-casted
$TbAl_2$	as-casted	$TbNi_2$	as-casted
$DyAl_2$	as-casted	$DyNi_2$	as-casted
$HoAl_2$	as-casted	$HoNi_2$	as-casted
$ErAl_2$	as-casted	$ErNi_2$	as-casted
Light rare-earth Laves phases with second-order phase transition			
$NdAl_2$	as-casted	$PrAl_2$	as-casted
$Nd_{0.75}Pr_{0.25}Al_2$	as-casted	$Pr_{0.75}Ce_{0.25}Al_2$	as-casted
$Nd_{0.5}Pr_{0.5}Al_2$	as-casted	$Pr_{0.5}Ce_{0.5}Al_2$	as-casted
$Pr_{0.75}Nd_{0.25}Al_2$	as-casted		
Light rare-earth based R_2In intermetallic compounds with first-order phase transition			
Nd_2In	as-casted	Pr_2In	as-casted

3.2 Crystallographic characterization

The crystal structure of all the samples were investigated by room-temperature X-ray powder diffraction (XRD). The XRD measurement is based on the Bragg's Law of $n\,\lambda = 2d\,sin\theta$, as illustrated in **Figure 3.1** (a). A constructive interference of monochromatic radiation (neutron, electron, x-ray) occurs when the scattered radiations satisfy Bragg's law. A schematic illustration of the powder XRD is shown in **Figure 3.1** (b). If the accumulated phase difference of two waves elastically reflected from the crystal planes is equal to an integer number of the wavelength, the diffraction patterns show a maximum due to the constructive interference. For X-ray powder diffraction, monochromatic radiation reflects from the randomly oriented crystal faces. The randomly oriented crystal faces leads to the formations of the symmetric Bragg cones.

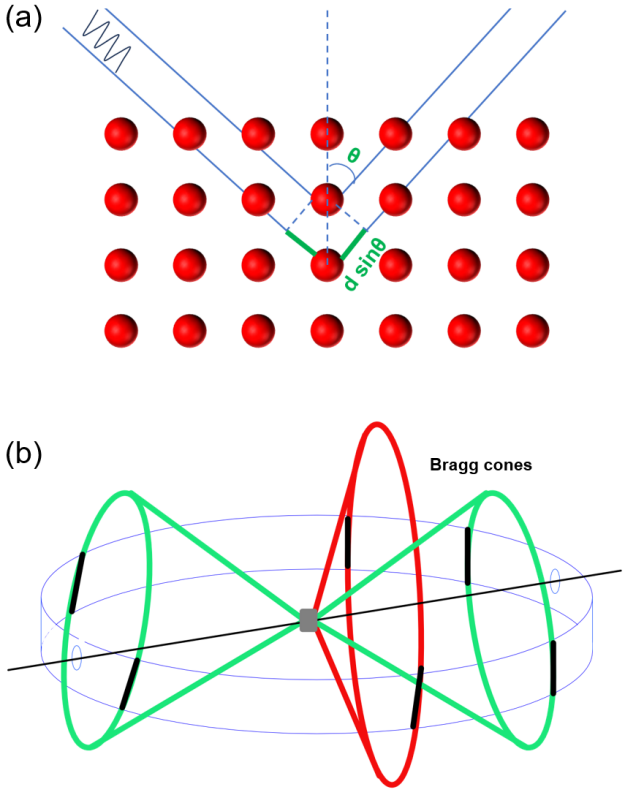

Figure 3.1: (a) Illustration of Bragg diffraction. (b) Illustration of Bragg Cone.

The X-ray machine STADIP from STOE was used in Debye-Scherrer geometry with a MoK$_{\alpha_1}$ radiation source ($\lambda = 0.70930\mathring{A}$). $\theta - 2\theta$ scans were performed between 5 and 50° with a step size of 0.01°. For the measurement, the material was crushed into fine powder. For the light rare-earth-based R_2In samples, their surfaces decompose in air and moisture. Therefore, hermetically sealed capillaries filled with ground powders for X-ray diffraction were prepared in an Ar- filled glovebox (p(O_2) < 0.1 ppm, MBraun) to avoid oxidation and decomposition.

3.3 Microstructure characterization

The microstructures of the samples were investigated using a Tescan Vega 3 scanning electron microscope (SEM). A scanning electron microscope is a type of electron microscope that uses a focused beam of electrons to produce images of a sample surface. **Figure 3.2** illustrates the electrons and X-rays produced by an electron beam hitting a sample surface. When electrons penetrate a sample surface, they undergo both elastic scattering and inelastic scattering. Some primary electrons are elastically scattered with a small fractional loss of energy. Those elastically scattered electrons with high kinetic energy are called backscattered electrons, carrying the backscattered electron (BSE) signals. Some primary electrons are inelastically scattered, and therefore, generate secondary electrons with low kinetic energy, carrying the secondary electron signals. Secondary electron imaging provides more surface information, while backscattered electron imaging shows a higher sensitivity to differences in atomic number.

Energy-dispersive X-ray spectroscopy (EDX, also abbreviated EDS) uses the characteristic X-rays to analyze the chemical characterization of materials. A sample excited by the incident electron beam dissipates some of the absorbed energy by ejecting a core-shell electron, leaving an electron hole. The electron hole will be refilled by an electron from the outer-shell electron with a higher energy. The difference in energy is released as an X-ray that has a characteristic spectrum depending on its atom of origin. The characteristic X-ray carries the compositional information, with the position of its peak identifying the element and the intensity corresponding to the concentration of the element.

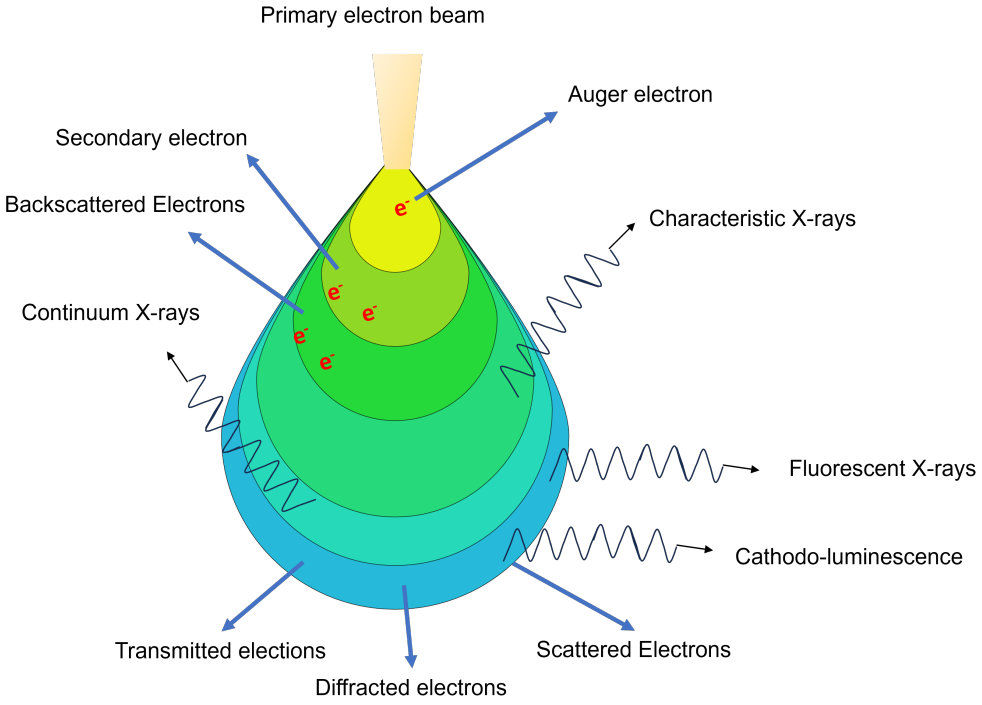

Figure 3.2: (a) Illustration of the backscatterred and secondary electrons.

3.4 Magnetic characterization

Magnetic measurements were performed in a physical property measurement system from Quantum Design (PPMS). In the VSM (vibrating sample magnetometer) mode of the PPMS, the magnetization measurements are based on Faraday's law. The electromotive force ϵ in a pickup coil is the changing rate of magnetic flux Θ_B with respect to time (t), and its vertical sinusoidal oscillation along the z axis is:

$$\epsilon = -\frac{d\Theta_B}{dT} = -\frac{d\Theta_B}{dz}\frac{dz}{dt} = 2\pi\, f\, C\, m\, A\, sin(2\pi f t)\,, \tag{3.1}$$

where A and f are the amplitude and frequency of the oscillation, and C is a coupling constant. For a VSM, the induced voltage in a pickup coil is related to the sample magnetic moment m, and its vertical sinusoidal oscillation along the z axis

A needle-shaped bulk piece with a mass between 10 and 50 mg was produced by mechanically crushing a sample. The needle-shaped piece was mounted into the sample holder. The needle-shaped piece is aligned in parallel with the magnetic field to reduce the demagnetizing field. By sweeping temperature in a constant magnetic field, magnetizations as a function of temperature ($M(T)$) were measured. By sweeping magnetic field at a constant temperature, magnetizations as a function of magnetic field ($M(H)$) were measured. Based on eq. (2.29) from Maxwell relation, there are two ways to measure the isothermal magnetic entropy change ΔS_T from magnetization measurements: (1) $M(T)$ measurements; (2) $M(H)$ measurements.

The numerical equation to calculate ΔS_T from $M(T)$ measurement is:

$$\Delta S_T(T,H) = \frac{\mu_0\, dH}{2}\left(\frac{dM_1}{dT} + 2\sum_{k=2}^{n-1}\frac{dM_k}{dT} + \frac{dM_n}{dT}\right), \tag{3.2}$$

where M_n is the magnetization of the n field step.

The numerical equation to calculate ΔS_T from $M(H)$ measurement is:

$$\Delta S_T(T,H) = \int_0^H \frac{M(T_f) - M(T_i)}{T_f - T_i}\, dH = \frac{\int_0^H M(T_f)\, dH - \int_0^H M(T_i)\, dH}{T_f - T_i}\,, \tag{3.3}$$

where T_f and T_i are two different temperatures that remain constant during magnetization and demagnetization.

There are two protocols for using the $M(H)$ method to obtain ΔS_T: (1) continuous cooling or heating, (2) discontinuous cooling or heating. For the continuous protocol, after each measurement, the sample is cooled or heated directly to the next temperature for the next measurement. For the discontinuous protocol, the sample is cooled or heated well above or well below the transition temperature before being cooled or heated to the next measurement temperature. Both protocols work well for the second-order phase transition. However, for the first-order phase transition associated with large hysteresis, it has been proven that using the continuous protocol can give an unreasonable value of ΔS_T because of the coexistence of two phases.

3.5 Heat capacity

The heat capacity C_p at constant pressure was also obtained using PPMS as well. The measurement is based on the equation $Q = C_p \Delta T$ where Q is the input heat and ΔT is the temperature change of a given system. The measurement is based on thermal relaxation calorimetry. **Figure 3.3** (a) shows the setup for the heat capacity measurement in the PPMS. The sample is attached to the platform by a thin layer of grease. A heater and a thermometer are attached to the backside of the platform with thin wires connecting to the thermal bath. If the thermal contact is good enough, the temperatures of the sample and the platform should be the same. **Figure 3.3** (b) shows the time dependence for heater power and temperature. **Figure 3.3** (c) illustrates the workflow and the equivalent circuit in this case. From the workflow and the equivalent circuit, the equation to calculate the heat capacity is as follows:

$$C_S \frac{dT}{dt} = -K_w(T - T_{bath}) + P(t)\,, \tag{3.4}$$

where C_S is the total heat capacity of the platform and the sample, K_w is the thermal conductance between the sample and the bath, T is the temperature of the platform, T_{bath} is the thermal bath temperature, and $P(t)$ is the input power. If we define a constant $\tau = C_S/K_w$, the solution takes the form of :

$$\Delta T(t) = \begin{cases} (\tau P_0/C_S)[1 - e^{-t/\tau}] & t_0 \geq t \geq 0\,; \\ ((\tau P_0/C_S)[1 - e^{-t_0/\tau}])[e^{-(t-t_0)/\tau}] & x \geq t_0\,. \end{cases} \tag{3.5}$$

However, in most cases, the sample and the platform are not well-coupled and the temperatures of the sample and the platform are not the same. **Figure 3.3** (d) illustrates the workflow and the equivalent circuit in this case. This method is the so-called 2τ method. The equation to calculate the heat capacity is:

$$\begin{aligned} C_{platform} \frac{dT_{platform}}{dt} &= -K_w(T_{platform} - T_{bath}) + P(t) + K_g(T_{sample} - T_{platform})\,, \\ C_{sample} \frac{dT_{sample}}{dT} &= -K_g(T_{sample} - T_{platform})\,, \end{aligned} \tag{3.6}$$

where $C_{platform}$ and C_{sample} are the heat capacities of the platform and sample, $T_{platform}$ and T_{sample} are their temperatures, and K_g is the thermal conductance of the used grease.

After obtaining the $C_{tot}(T, H)$ from the heat capacity measurement, the $S(T, H)$ curves can be constructed, and ΔS_T and ΔT_{ad} can be calculated using eq. (2.18).

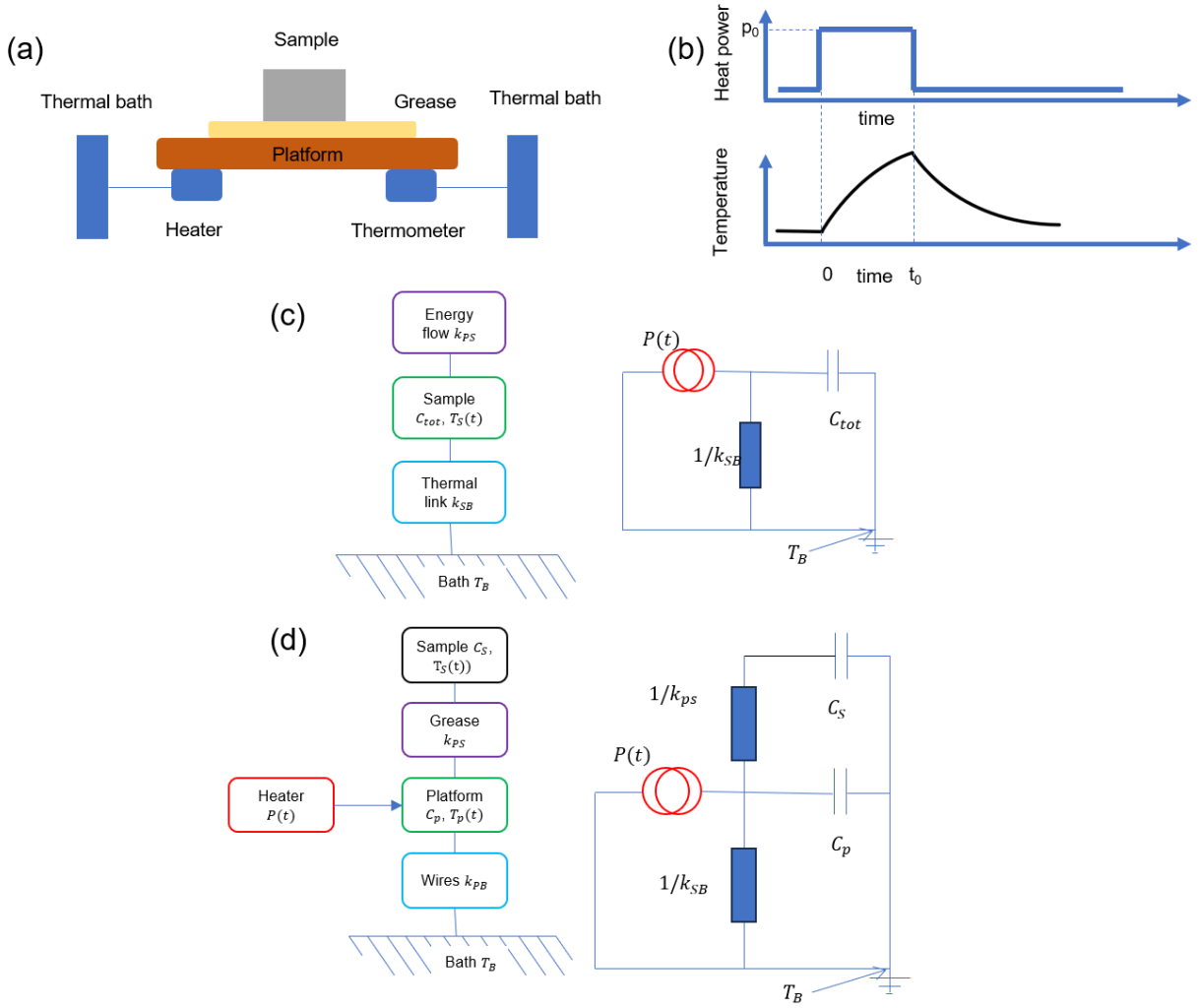

Figure 3.3: (a) Schematic diagram of the experimental setup for heat capacity measurements. (b) Time dependence for heater power and temperature. (c) Workflows for the one τ and two τ methods, and their corresponding equivalent circuits.

3.6 Adiabatic temperature change measurement

3.6.1 Adiabatic temperature change measurement in static fields

A home-built experimental setup is used to perform the direct ΔT_{ad} measurements. A Halbach-cylinder assembly produces a magnetic field of up to 1.95 T in the bore center. A Hall probe measures the external magnetic field. The magnetic field changes at a speed of 0.5 T/s, which is fast enough to neglect the heat losses from the specimen to the environment upon measurement. A Copper-Constantan thermocouple (T-type) in direct contact with the sample controls the temperature changes with an accuracy better than ± 0.01 K.

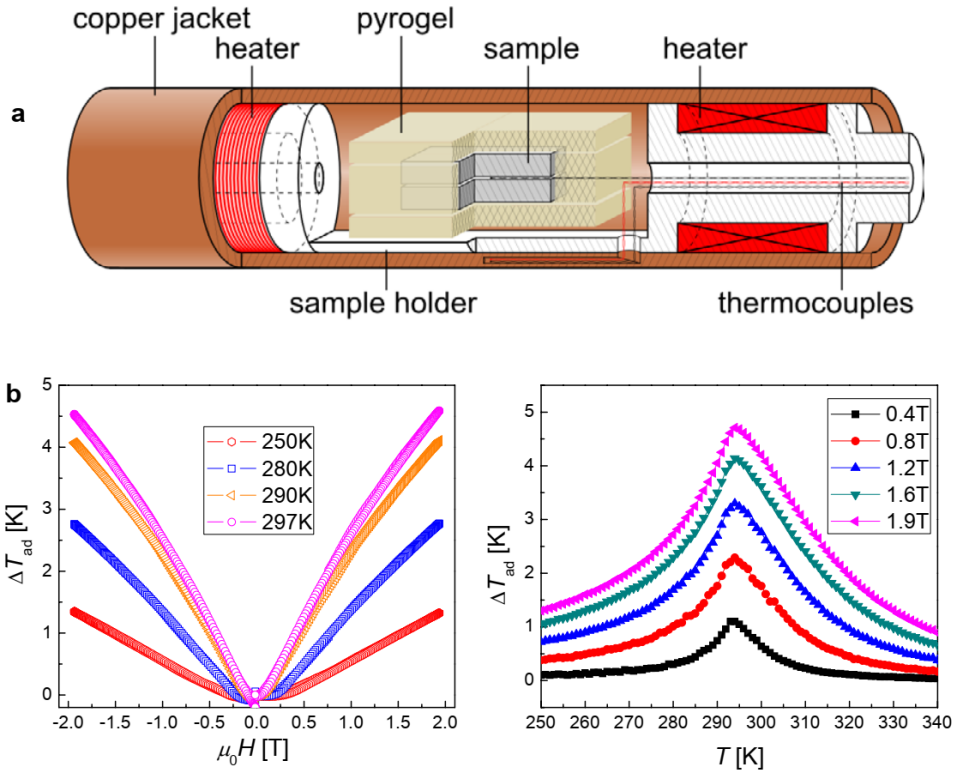

Figure 3.4: (a) Schematic of adiabatic temperature change (ΔT_{ad}) measurement cell in magnetic fields generated by Halbach magnet. (b) Magnetic field and temperature dependence of adiabatic temperature change (ΔT_{ad}) of a polycrystalline Gd sample. The figure is adopted from [70].

Figure 3.4 (a) shows the measurement cell schematically. Two plates with an approximate size of 4 $\times$ 2$\times$ 1 mm are cut from the sample to be measured. A thermocouple is placed between the two plates. To improve the thermal conduct, a small amount of thermo-conductive silver-based glue is used. The specimen is heated by the sample holder equipped with a resistive electric heater. The sample chamber connected to a pump providing a vacuum 10^{-6} mbar is inserted into a liquid nitrogen Dewar. An analogue-to-digital converter with a sampling time of 1000 points/s collects the pre-amplified signals from the thermocouple and the Hall probe. ΔT_{ad} is measured at a certain temperature as a function of the magnetic field H. The device shows excellent adiabatic conditions, as confirmed by the measurements on a polycrystalline Gd sample shown in **Figure 3.4** (b).

3.6.2 Adiabatic temperature change measurement in pulsed fields

Figure 3.5 schematically plots the setup of the ΔT_{ad} measurement in pulsed fields. ΔT_{ad} directly measured under pulsed fields were performed at the High Magnetic Field Laboratory (address: Helmholtz-Zentrum Dresden-Rossendorf, Dresden, Germany). With the non-destructive solenoids in the laboratory, a high magnetic field up to 95 T can be achieved. Pulsed fields as the magnetic field source help to approach the adiabatic condition. The short duration of the pulsed fields reduces the time it takes for the specimen to exchange heat with the environment.

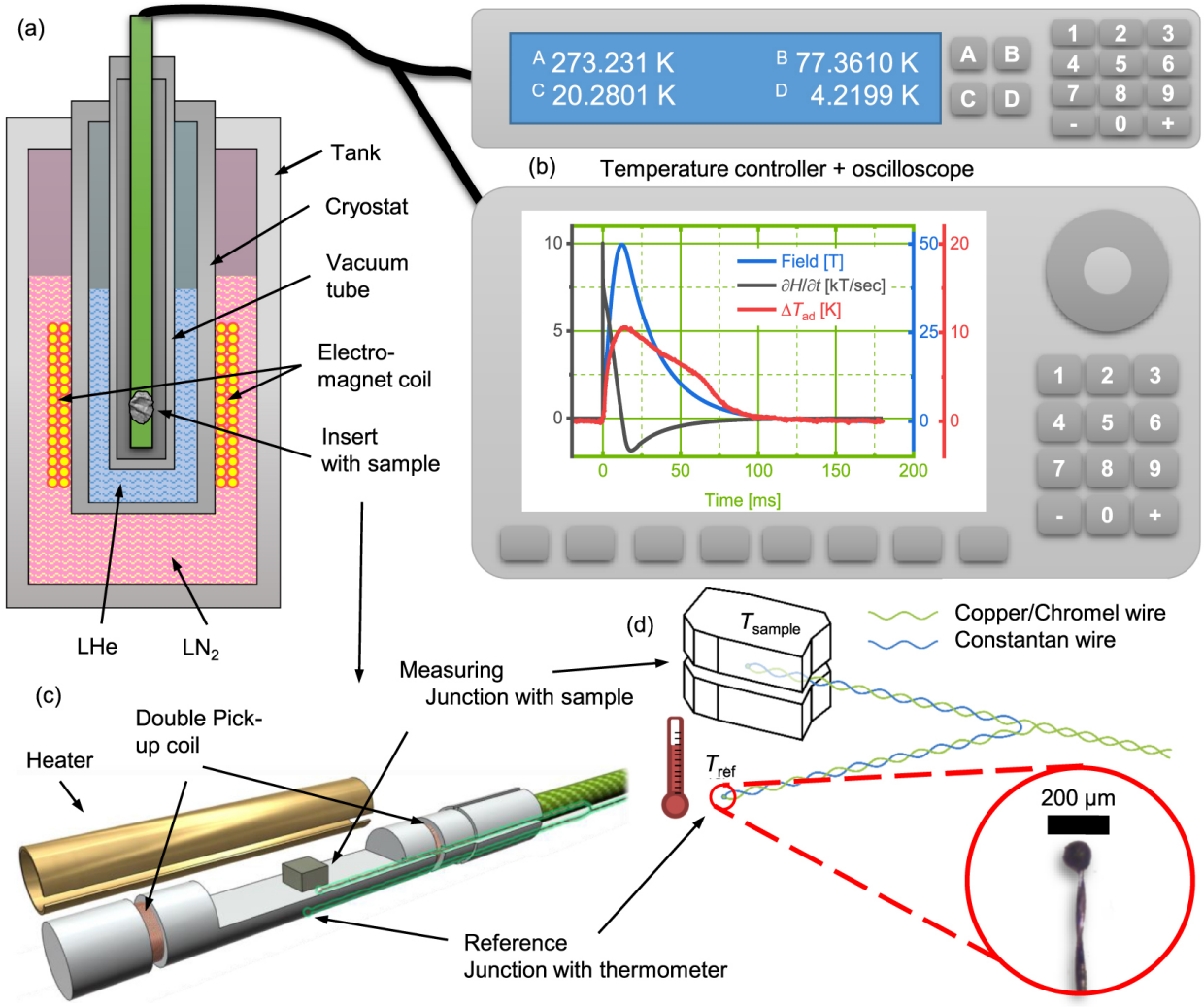

Figure 3.5: Experimental set-up for direct measurements of adiabatic temperature change in pulsed fields. (a) Measurement chamber. (b) Temperature sensor and oscilloscope sampling the signals of the pick-up coil and the thermocouple signals. (c) Sample holder. (d) "Sandwich" structured specimen and a zoomed image of the thermocouple junction. The picture is taken from [71].

For the measurements of the samples in this thesis, a KS11 coil was used to generate the pulsed fields. To prevent overheating due to ohmic resistance, which can damage the magnetic coil, the magnetic coil is placed in a tank of liquid nitrogen, as shown in **Figure 3.5** (a). With a bath cryostat filled with liquid helium located at the center of the coil, a temperature of as low as 4.2 K can be achieved. The sample is inside the

cryostat. **Figure 3.5** (b) demonstrates the spatial dependence of the field along the axial direction of the magnetic coil. The blue curve shows the time profile of the magnetic field, and the black curve displays the changing rate of the magnetic field. The magnetic field reaches the maximum value quickly in the first 13 ms and then decreases at a relatively slower rate. The total duration of the pulse is about 150 ms.

As shown in **Figure 3.5** (d), two plates with an approximate size of $4 \times 2 \times 1$ mm cut from a sample are fixed onto the sample holder by a small amount of GE varnish. The temperature of the sample is controlled by a cylinder heater with a manganin wire, which is placed around the specimen without a direct contact to it. The temperature of the sample is measured using a differential thermocouple fixed between two plates cut from the sample using a small amount of heat-conducting silver epoxy paste. **Figure 3.5** (c) illustrates the sample holder made of PEEK material with a low thermal conductivity. The reference thermocouple is attached to Cernox CX-SD thermistor at the backside of the sample holder. The sample holder is installed in a stainless steel vacuum tube. A high vacuum of about 10^{-5} mbar is created in the tube. The heater and thermometer are connected to a Lake Shore 350 temperature controller, as shown in **Figure 3.5** (b). The signals from the thermocouple and the double pick-up coil are collected by an oscilloscope with a time step of 2 µs.

3.7 Simultaneous measurement setup

To measure the magnetization, strain, and electrical resistivity simultaneously, which are important for the understanding of the magnetoelastic, magnetostructural, magnetoelectric couplings, a purpose-built experimental setup was designed and built. This instrument enhances the measurement capacity of the VSM option of the PPMS device from Quantum Design.

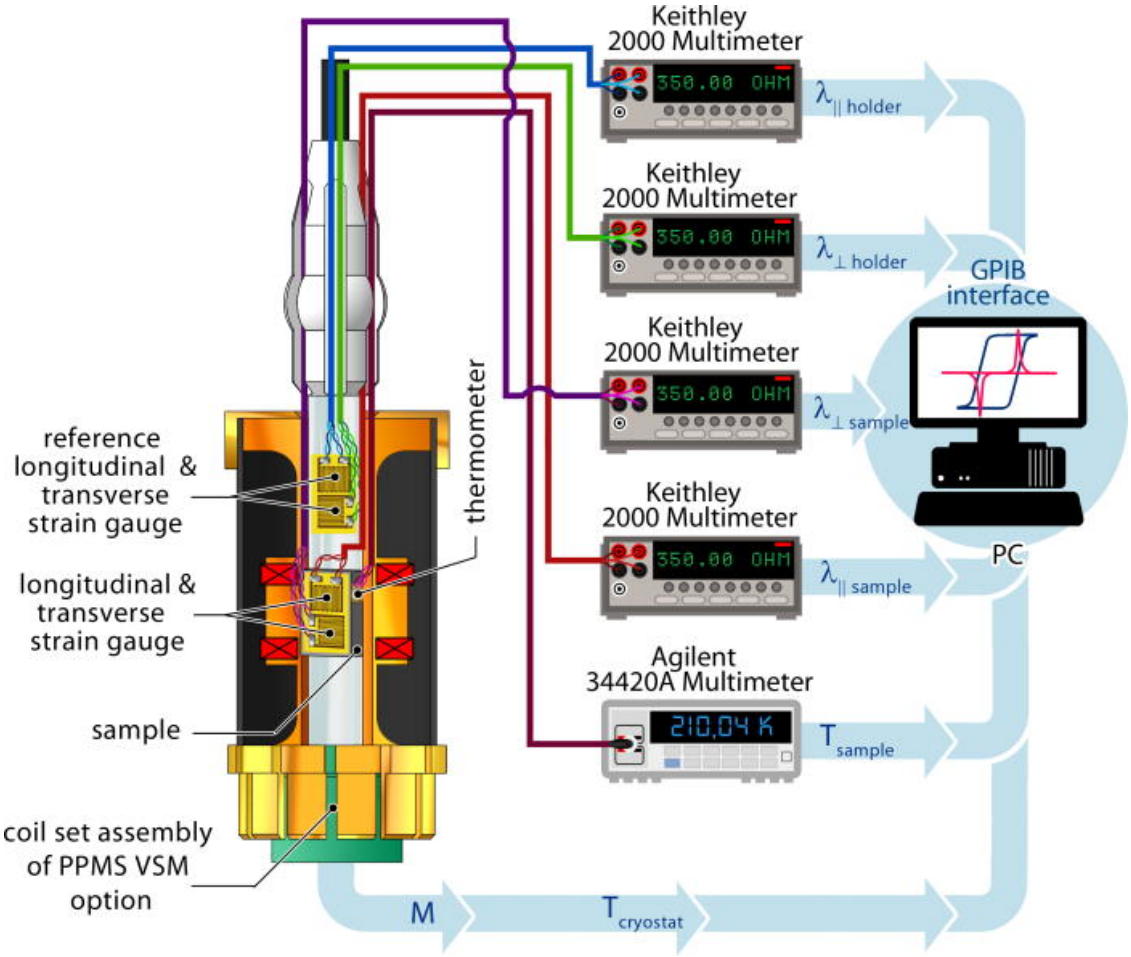

Figure 3.6: A Purpose-built experimental setup for the simultaneous measurements of magnetization, magnetostriction, electrical resistivity, and temperature change. The picture is taken from [72].

Figure 3.6 illustrates the experimental setup. To conduct the measurement, a cube of about 2 mm $\times$ 1 mm $\times$ 3 mm was cut from the sample to be measured. Two strain gauge were glued on the sample surface with the M-Bond 610 adhesive. To ensure accurate measurement, the entire surface of the specimen was covered by the strain gauge grids. Two additional strain gauges were glued on a sapphire plate and were placed near the sample to correct the changes of the resistivities induced by the external magnetic field and temperature in the strain gauges. The resistive sensors Cernox CX-1050-BC welded to the specimen with indium were used to measure the temperature of the specimen.

4 Results and discussion

4.1 A study on heavy rare-earth Laves phases

4.1.1 "Giant" second-order MCE at cryogenic temperatures

Since the discovery of the giant MCE in $Gd_5Si_2Ge_2$ by Pecharsky *et al.* in 1997 [73], room-temperature MCE has been in the spotlight [74]. Impressive progress has been made, such as the discoveries of the giant first-order MCEs in $La(Fe, Si)_{13}$ [75] alloys, NiMn-based Heusler alloys [70, 76–79], Fe_2P-based alloys [80], and MnAs [81]. The giant first-order MCE dominates the research on room-temperature MCE, because, other than Gd and $La(Fe, Co, Si)_{13}$, the rest of the second-order magnetocaloric materials often show an insufficient magnetocaloric effect near room temperature [23]. It is often written that second-order magnetocaloric materials have small magnetocaloric effects, while "giant" is often a label attached to the first-order magnetocaloric materials [82].

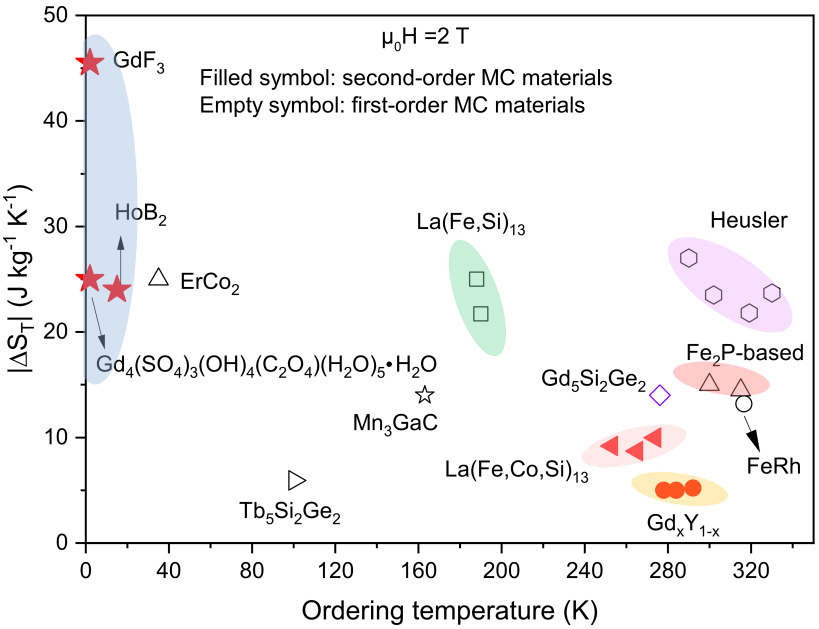

Figure 4.1: Comparing the ΔS_T of the selected first-order and second-order magnetocaloric materials. Data are taken from [23, 73, 80, 83–95].

But, is the statement "second-order MCE is small" really true? In **Figure 4.1**, the ΔS_T of the second-

order magnetocaloric materials $[Gd_4(SO_4)_3(OH)_4(C_2O_4)(H_2O)_5]_n \cdot nH_2O$ [94], GdF_3 [94], and HoB_2 [92] in magnetic fields of 2 T are compared with some typical giant first-order magnetocaloric materials, and the second-order magnetocaloric materials Gd_xY_{1-x} [23] and $La(Fe, Co, Si)_{13}$ [93]. GdF_3 shows a maximum ΔS_T of $45.5\,J\,K^{-1}\,kg^{-1}$ at 2 K [94]. For $[Gd_4(SO_4)_3(OH)_4(C_2O_4)(H_2O)_5]_n \cdot nH_2O$, the value is $25\,J\,K^{-1}\,kg^{-1}$ [94]. These two second-order magnetocaloric materials clearly break the "stereotype" that the second-order magnetocaloric materials show small magnetocaloric effects. To compare with, giant first-order material $Gd_5Si_2Ge_2$ shows a ΔS_T of $14\,J\,K^{-1}\,kg^{-1}$ [73].

Even near the condensation point of hydrogen, the second-order magnetocaloric material HoB_2 still shows an impressive ΔS_T in magnetic fields of 2 T of $25\,J\,K^{-1}\,kg^{-1}$ [92], surpassing most of the first-order magnetocaloric materials listed in **Figure 4.1**, including $ErCo_2$, a magnetocaloric material that is often proposed to be used in an active magnetic regenerator for hydrogen liquefaction [12]. However, near room temperature, such impressive values are not found in the second-order magnetocaloric materials. Gd, one of the most outstanding second-order magnetocaloric materials near room temperature, shows the smallest ΔS_T in the plot.

Adiabatic temperature change ΔT_{ad} is a parameter that is as important as ΔS_T for MCE. **Figure 4.2** displays the ΔT_{ad} of TmCoSi, $ErCr_2Si_2$, HoB_2, some of the typical giant first-order magnetocaloric materials, and the second-order magnetocaloric materials Gd_xY_{1-x} and $La(Fe, Co, Si)_{13}$ in magnetic fields of 2 T. Unlike the ΔS_T where we see that the second-order magnetocaloric materials can show a significantly larger value at low temperature than the first-order giant magnetocaloric materials, the first-order giant magnetocaloric material FeRh exhibits the largest value of ΔT_{ad} near room temperature, reaching 12.9 K [96]. Nevertheless, TmCoSi and $ErCr_2Si_2$ still show the second and third largest ΔT_{ad} respectively [97, 98]. And the ΔT_{ad} of HoB_2 is comparable to that of La-Fe-Si [92].

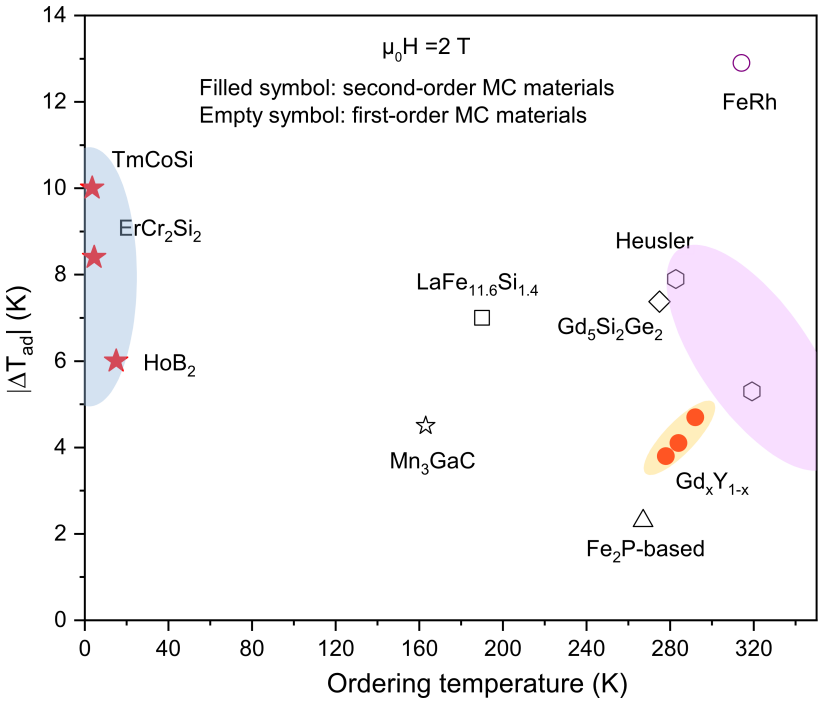

Figure 4.2: Comparing the ΔT_{ad} of the selected first-order and second-order magnetocaloric materials. Data are taken from [23, 73, 85, 91, 92, 96–100].

The above discussion addresses a feature that second-order magnetocaloric material can even show larger magnetocaloric effect than giant first-order magnetocaloric materials in cryogenic temperature range, pointing out that the statement "second-order magnetocaloric materials show small magnetocaloric effects" is not completely correct. The discovery of this feature lead to a physical question: how does cryogenic temperature influence the maximum magnetic entropy and adiabatic temperature changes? Considering that most second-order magnetocaloric materials show the maximum ΔS_T and ΔT_{ad} near T_C [101], this question can be rephrased as: how does Curie temperature act on the maximum magnetic entropy and adiabatic temperature changes?

4.1.2 Laves phases for studying correlation between MCE and Curie temperature

To answer the question raised above experimentally, a material system that only varies in Curie temperature with the other properties such as the total magnetic moment and the microstructure staying constant is needed. Such an ideal system does not exist, since the magnetic entropy and adiabatic temperature changes are influenced by many factors, such as intrinsic factors like magnetic ordering and electronic structure, and extrinsic factors such as grain size and phase coexistence [12]. A compromise needs to be made here: a material system that varies in Curie temperature with the other properties staying similar is needed.

Table 4.1: Spin quantum number S, azimuthal quantum number L, total angular momentum quantum number J, g-factor g_J, $g_J\,J$, theoretical and experimental effective magnetic moments μ_{eff} and μ_{eff}^{exp}, and de Gennes factor G of the rare-earth ions. Data are taken from [39].

ions	S	L	J	g_J	$g_J\,J$	μ_{eff} (μ_B)	μ_{eff}^{exp} (μ_B)	G
Ce^{3+}	1/2	3	5/2	6/7	2.14	2.54	2.5	0.18
Pr^{3+}	1	5	4	4/5	3.20	3.58	3.5	0.80
Nd^{3+}	3/2	6	9/2	8/11	3.27	3.52	3.4	1.84
Pm^{3+}	2	6	4	3/5	2.40	2.68	-	-
Sm^{3+}	5/2	5	5/2	2/7	0.71	0.85	1.7	4.46
Eu^{3+}	3	3	0	0	0	0	3.4	-
Gd^{3+}	7/2	0	7/2	2	7.0	7.94	8.9	15.75
Tb^{3+}	3	3	6	3/2	9.0	9.72	9.8	10.50
Dy^{3+}	5/2	5	15/2	4/3	10.0	10.65	10.6	7.08
Ho^{3+}	2	6	8	5/4	10.0	10.61	10.4	4.5
Er^{3+}	3/2	6	15/2	6/5	9.0	9.58	9.5	2.55
Tm^{3+}	1	5	6	7/6	7.0	7.56	7.6	1.17
Yb^{3+}	1/2	3	7/2	8/7	4.0	4.53	4.5	0.29

Speaking of similarity, the rare-earth elements are physically and chemically similar. **Table 4.1** shows the magnetic properties of the rare-earth ions. Within the heavy rare-earth ions, Gd^{3+}, Tb^{3+}, Dy^{3+}, Ho^{3+}, and Er^{3+} have effective magnetic moments around 10 μ_B, with Gd^{3+} showing the smallest magnetic moment of 8.9 μ_B, and Dy^{3+} showing the largest magnetic moment of 10.6 μ_B.

So, can these rare-earth elements form a material system that fulfills the aforementioned requirement? The heavy rare-earth Laves phases RAl_2, RNi_2, and RCo_2 (R: Gd, Tb, Dy, Ho, Er, and Tm) belong to the intensively studied material systems due to their excellent magnetocaloric effects covering a large temperature range. $GdCo_2$ has the highest Curie temperature of about 404 K [102], while $TmNi_2$ has the lowest Curie temperature of about 1 K [103]. The rest of the materials exhibit a Curie temperature within these two temperatures [12, 103–105]. The similarities of the heavy rare-earth Laves phases and the large temperature range covered by their Curie temperatures make them potential material systems for studying the correlations between magnetocaloric effect and Curie temperature [12].

Named for the German crystallographer Fritz Laves, Laves phases are intermetallic phases that have the composition of AB_2. More than 1200 binary and ternary Laves phases have been characterized, of which the rare-earth-based alloys make up about 60 % [102]. **Figure 4.3** displays the crystal structure of Laves phases [106]. The rare-earth elements that occupy the A site are highlighted in red, while the metals that take the B site are marked in cyan. As shown in **Figure 4.3**, there are three classes of Laves phases: cubic $MgCu_2$ (C15), hexagonal $MgZn_2$ (C14), and hexagonal $MgNi_2$ (C36). About 60% of the Laves phases crystallize in the cubic C15 structure type, about 35% in the C14 structure crystallize in the hexagonal C14 structure type, while only 3% crystallize in the hexagonal C36 type [102]. Laves phases find their applications in many areas, including magnetomechanical sensors and actuators, hydrogen storage, superconductivity, wear- and corrosion materials, etc [106]. Magnetic refrigeration is one of the subjects.

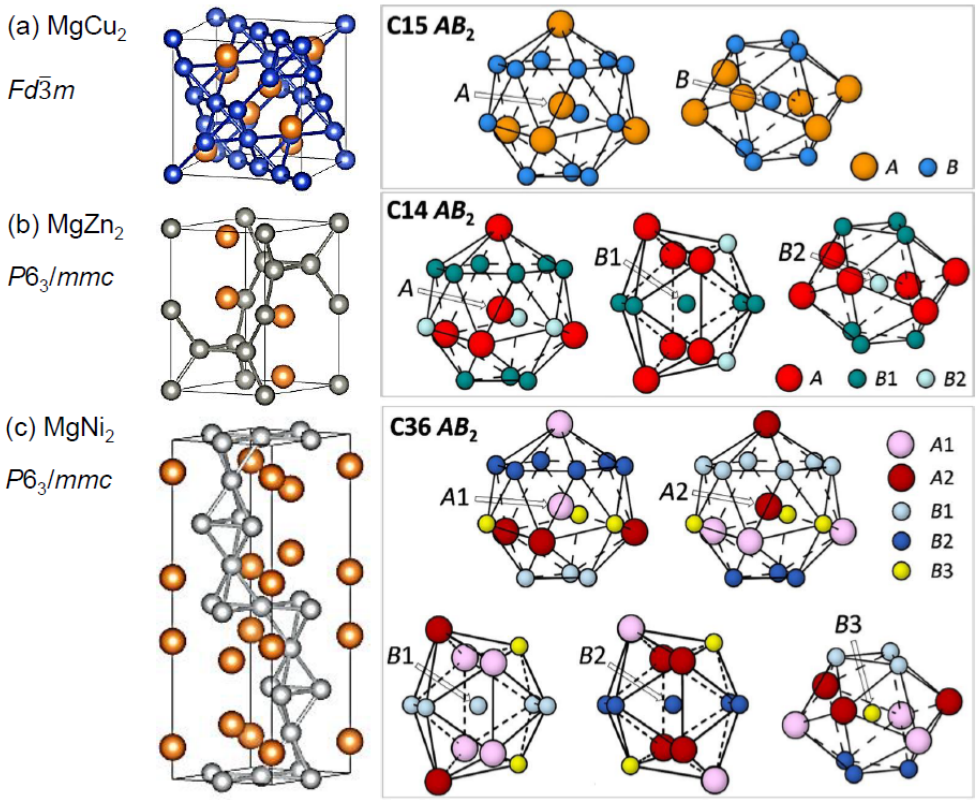

Figure 4.3: Crystal structures of Laves phases: (a) Cubic $MgCu_2$-type (C14), (b) Hexagonal $MgZn_2$-type (C15), (c) $MgNi_2$-type (C36). The left pictures are the corresponding coordination polyhedral for each atomic site in the structure. Picture is taken from [106].

Figure 4.4 shows the possible binary rare-earth-based Laves phases and their crystal structure type [102]. Rare-earth elements can form Laves phases with alkaline earth metal Mg, post-transition metals, and transition metals including the precious metals (Ru, Rh, Pd, Re, Os, Ir, and Pt) and Mn, Fe, Co, Ni, Tc. All the RAl_2, RNi_2, and RCo_2 Laves phases (if existing) belong to the cubic C15 structure type, except $EuNi_2$ crystallizing in the hexagonal C36 structure type.

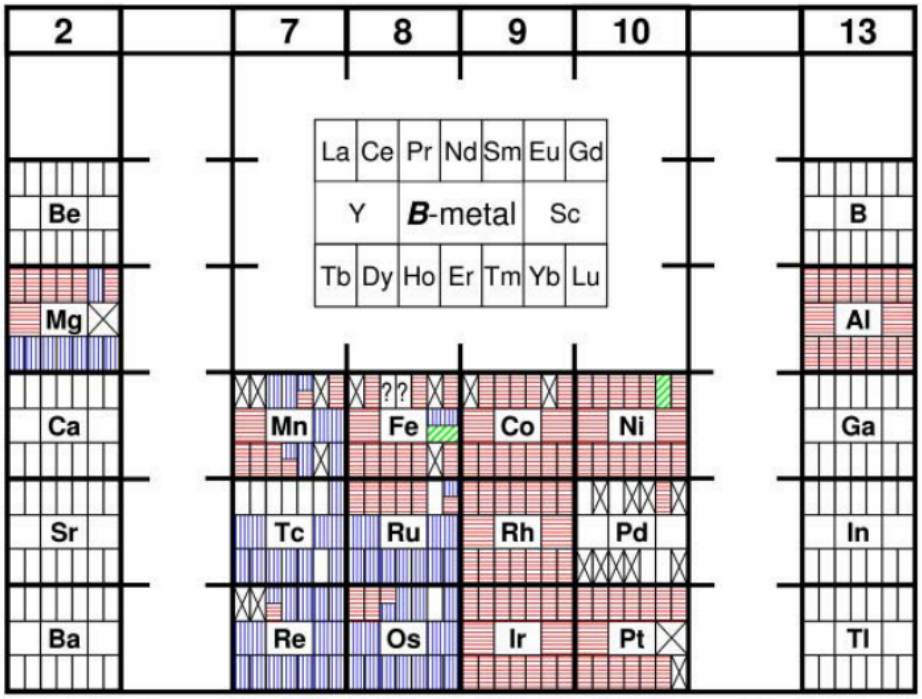

Figure 4.4: Possible Laves phases and their crystal structures. Picture is taken from [102].

Both the RAl_2, RNi_2 (R: Pr, Nd, Sm, Gd, Tb, Dy, Ho, Er, Tm, Yb) Lave phases undergo a second-order magnetic phase transition. Compared to RAl_2 and RNi_2, the order of the phase transitions of the Laves phases RCo_2 is complicated. The light rare-earth-based Laves phases $NdCo_2$ and $SmCo_2$ undergo second-order magnetic phase transitions. As discussed in **Section 2.4.1**, it is still under debate whether the light rare-earth-based Laves phase $PrCo_2$ shows a first-order phase transition or not.

For the heavy rare-earth-based Laves phases, $GdCo_2$, $TbCo_2$, and $TmCo_2$ show second-order magnetic phase transitions at T_C, while $DyCo_2$, $HoCo_2$, $ErCo_2$ undergo first-order magnetic phase transitions. It should be emphasized that a recent study support the first-order phase transition of $TbCo_2$ at T_C, evidenced by the detected thermal hysteresis, latent heat, structural transition, and the Banerjee criterion [107].

In this work, the heavy rare-earth-based Laves phases RCo_2 are not chosen to study the correlations between MCE and T_C because of the controversial nature of phase transition in RCo_2. Instead, the heavy rare-earth Laves phases RAl_2 (R: Gd, Tb, Dy, Ho, and Er), with their T_C ranging from around 165 K for $GdAl_2$ to around 13 K for $ErAl_2$, and RNi_2, with their T_C ranging from around 77 K for $GdNi_2$ to 6 K for $ErNi_2$, are chosen.

4.1.3 Microstructure and Crystallography of RAl_2 and RNi_2

The heavy rare-earth-based Laves phases RAl_2 and RNi_2 (R: Gd, Tb, Dy, Ho, and Er) were synthesized by arc melting, as introduced in **Chapter 3**. The quality of the samples were examined by BSE and powder XRD. The results of BSE imaging are displayed in **Figure 4.5** and **Figure 4.6** for RAl_2 and RNi_2, respectively. Rare-earth rich impurities are observable in these samples, as they appear in bright color in the images. The samples $GdAl_2$, $TbAl_2$, $DyAl_2$, $ErAl_2$, $DyNi_2$, and $ErNi_2$ have rather small amounts of impurities, while $GdNi_2$, $TbNi_2$, $HoNi_2$, and $HoAl_2$ show evident amounts of impurities.

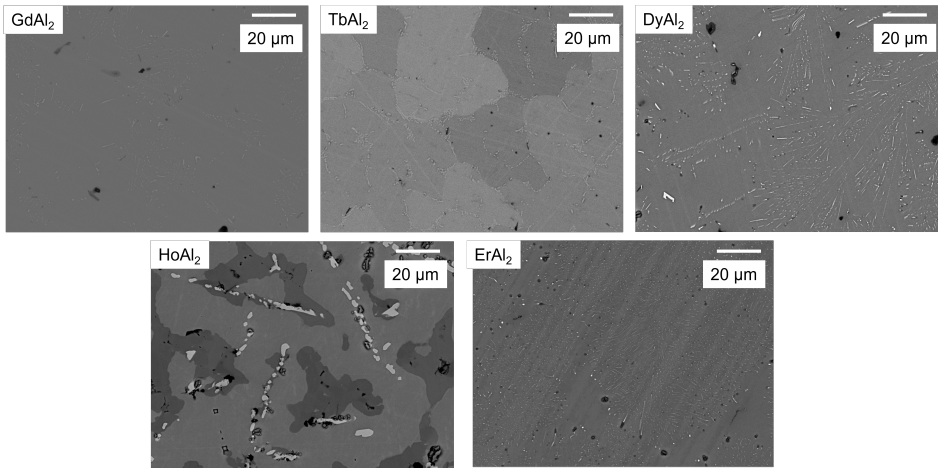

Figure 4.5: BSE images of $GdAl_2$, $TbAl_2$, $DyAl_2$, $HoAl_2$, $ErAl_2$.

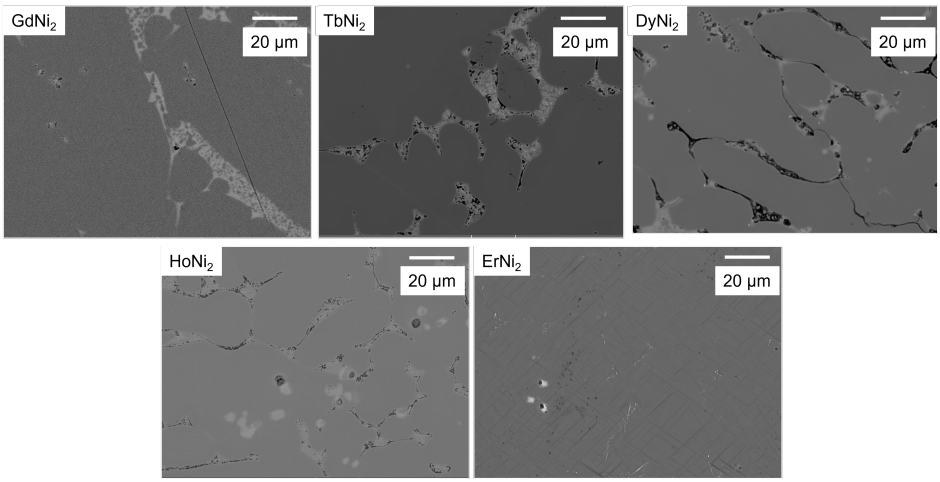

Figure 4.6: BSE of $GdNi_2$, $TbNi_2$, $DyNi_2$, $HoNi_2$, $ErNi_2$.

To further confirm the quality of the samples, powder X-ray diffraction experiments were conducted, as described in **Chapter 3**. The Rietveld refinements on the powder X-ray diffraction patterns were performed using the FullProf software. The XRD patterns of the RNi_2 series and RAl_2 series are plotted in **Figure 4.7** (a) and **Figure 4.8** (a), respectively. **Figure 4.7** (b) and **Figure 4.8** (b) show the results of the Rietveld refinements of $DyAl_2$ and $DyNi_2$ respectively. The XRD measurements confirm that all the samples crystallizing in the Cubic $MgCu_2$ type. The phase fraction analyses are listed in **Table 4.2**.

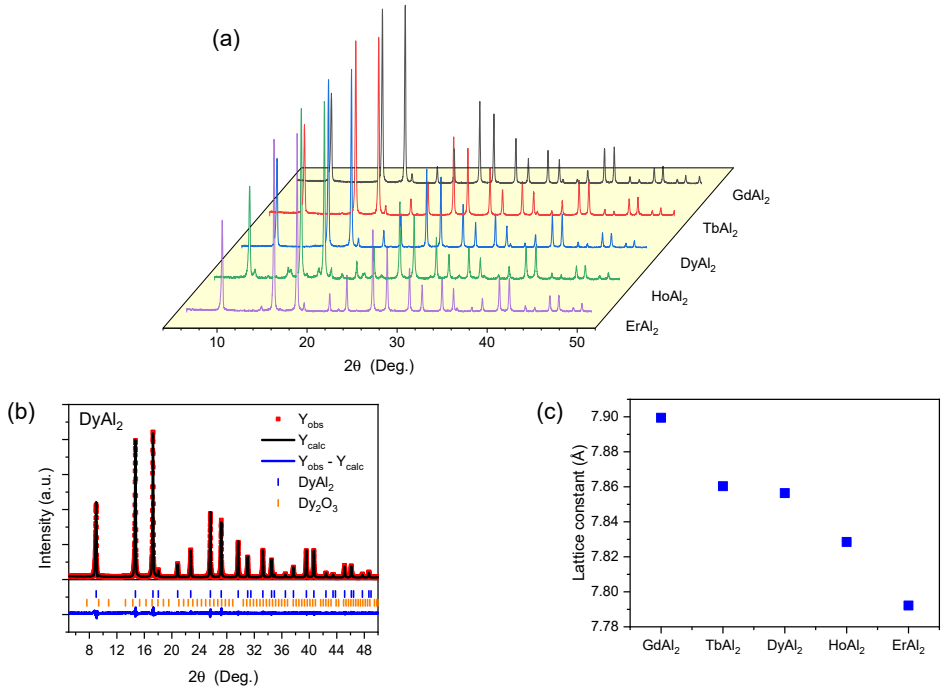

Figure 4.7: (a) XRD patterns of RAl_2. (b)Rietveld refinement of $DyAl_2$. (c) Lattice constants of RAl_2.

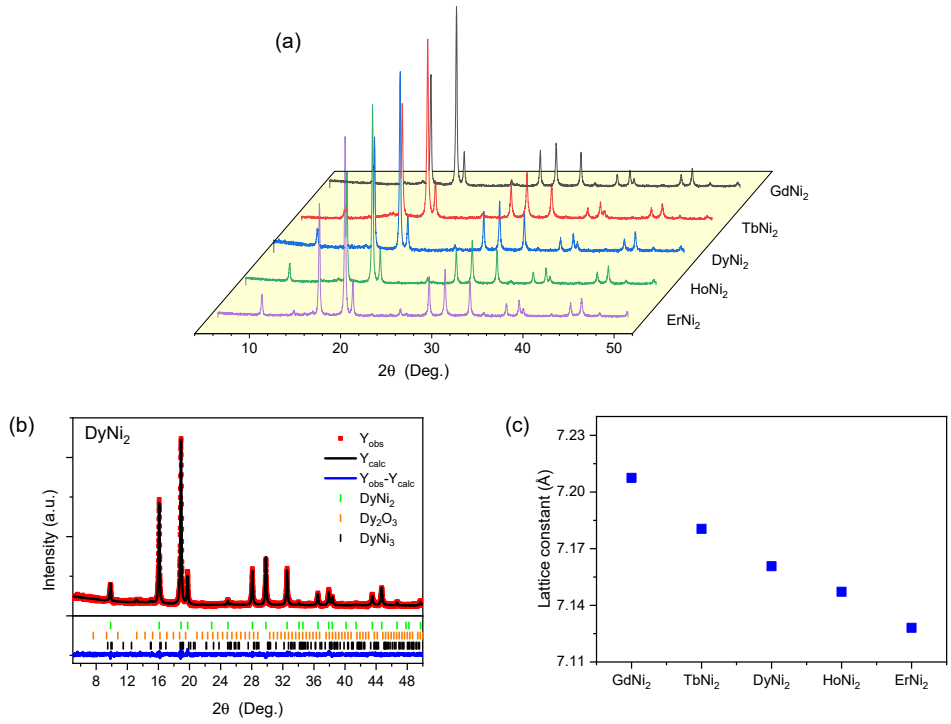

Figure 4.8: (a) XRD patterns of RNi_2. (b)Rietveld refinement of $DyNi_2$. (c) Lattice constants of RNi_2.

Agreeing with the BSE measurements, $GdAl_2$, $TbAl_2$, $DyAl_2$, $ErAl_2$, $DyNi_2$, and $ErNi_2$ samples exhibit high purities. The purities of $GdAl_2$, $TbAl_2$, and $DyAl_2$ samples are close to 100%, and the purities of $DyNi_2$ and $ErNi_2$ samples are above 95%. The purity of $HoNi_2$ sample is slightly smaller than 95%, with Ho_2O_3 and $HoNi_3$ impurities confirmed. Impurities of $TbNi_3$, Tb_2Ni_{17} are found in $TbNi_2$ sample, showing a purity of 91%. Impurities of Ho_2O_3 and $HoAl_3$ are observed in $HoAl_2$ sample, exhibiting a purity of 87.5%. $GdNi_2$ shows a purity of 83%, with impurities of Gd_2O_3, Gd_2Ni_{17}, and Ni confirmed. The BSE and powder X-ray diffraction measurements confirm the sufficient quality of all the samples.

Table 4.2: Contents of main phase and impurities for RAl_2 and RNi_2 Laves phases (R: Gd, Tb, Dy, Ho, Er) from XRD and EDX analysis.

Sample	**Laves phase content** (%)	**Impurities**	**Impurity content** (%)
$GdAl_2$	100	-	-
$TbAl_2$	99.5	-	-
$DyAl_2$	99.5	-	-
$HoAl_2$	87.5	Ho_2O_3	3.4
		$HoAl_3$	9.1
$ErAl_2$	97.9	Er_2O_3	2.1
$GdNi_2$	83	Gd_2O_3	1.1
		Gd_2Ni_7	9.5
		Gd_2Ni_7	4.4
		Ni	1.8
$TbNi_2$	91	$TbNi_3$	5.0
		Tb_2Ni_{17}	3.9
$DyNi_2$	95.9	Dy_2O_3	1.2
		$DyNi_3$	2.9
$HoNi_2$	94.5	Ho_2Ni_3	1.1
		$HoNi_3$	3.3
		Ho_2Ni_7	1.1
$ErNi_2$	96	Er_2O_3	2
		$ErNi_3$	2

In addition to the phase fraction analyses, the lattice constants are also obtained from the Rietveld refinements and are shown in **Figure 4.7** (c) for the RAl_2 series, and **Figure 4.8** (c) for the RNi_2. $GdAl_2$ has the largest lattice constant in the RAl_2 series, and $GdNi_2$ has the largest lattice constant in the RNi_2 series. In both material systems, it is observed that the lattice constant decreases almost linearly with the atomic number of the rare-earth elements increasing, except that the lattice constant of $DyAl_2$ shows a noticeable deviation from the linear relationship. This is coherent with the fact that Gd has the largest atom size among the rare-earth series (Gd, Tb, Dy, Ho, Er), while Er has the smallest atom size.

4.1.4 Magnetic properties

As discussed above, the heavy rare-earth ions Gd^{3+}, Tb^{3+}, Dy^{3+}, Ho^{3+}, and Er^{3+} possess large magnetic moments. Large magnetic moment is a precondition to achieve a larger magnetization. **Figure 4.9** (a) and (b) plot the magnetization as a function of temperature for the RAl_2 Laves phase series in magnetic fields of 2 and 5 T. At 20 K, all the alloys achieve a magnetization above 150 A m^2 kg^{-1} and above 175 A m^2 kg^{-1} in magnetic fields of 2 and 5 T, respectively. **Figure 4.9** (c) and (d) plot the magnetizations as a function of magnetic fields and temperature for $DyAl_2$, respectively. The saturation magnetization at 32.5 K is about 200 A m^2 kg^{-1}. These analyses show that these alloys exhibit large magnetizations in their ferromagnetic state. Large magnetizations in the ferromagnetic state of the Laves phase series RNi_2 are also observed, as shown in **Figure 4.10** (a) (b) (c) and (d).

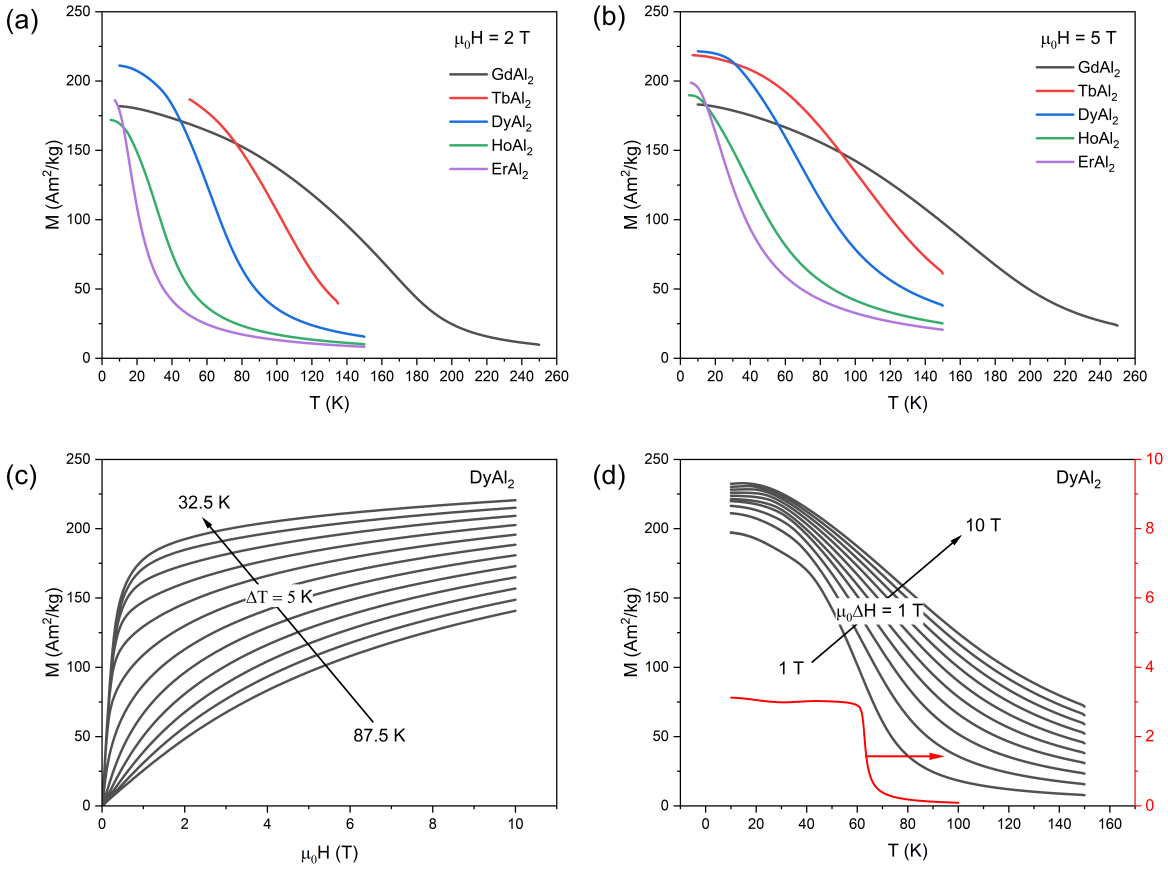

Figure 4.9: (a) (b) Magnetization as a function of temperature for RAl_2 samples in magnetic fields of 2 and 5 T, respectively. (c) (d) Magnetization as a function of magnetic fields and temperature for $DyAl_2$, respectively.

To confirm the similarity of the magnetic moments of the heavy rare-earth-based Laves phases, the Curie-Weiss fit was applied to determine the effective magnetic moment. According to Curie-Weiss law, the mass susceptibility χ of a material under small magnetic fields is:

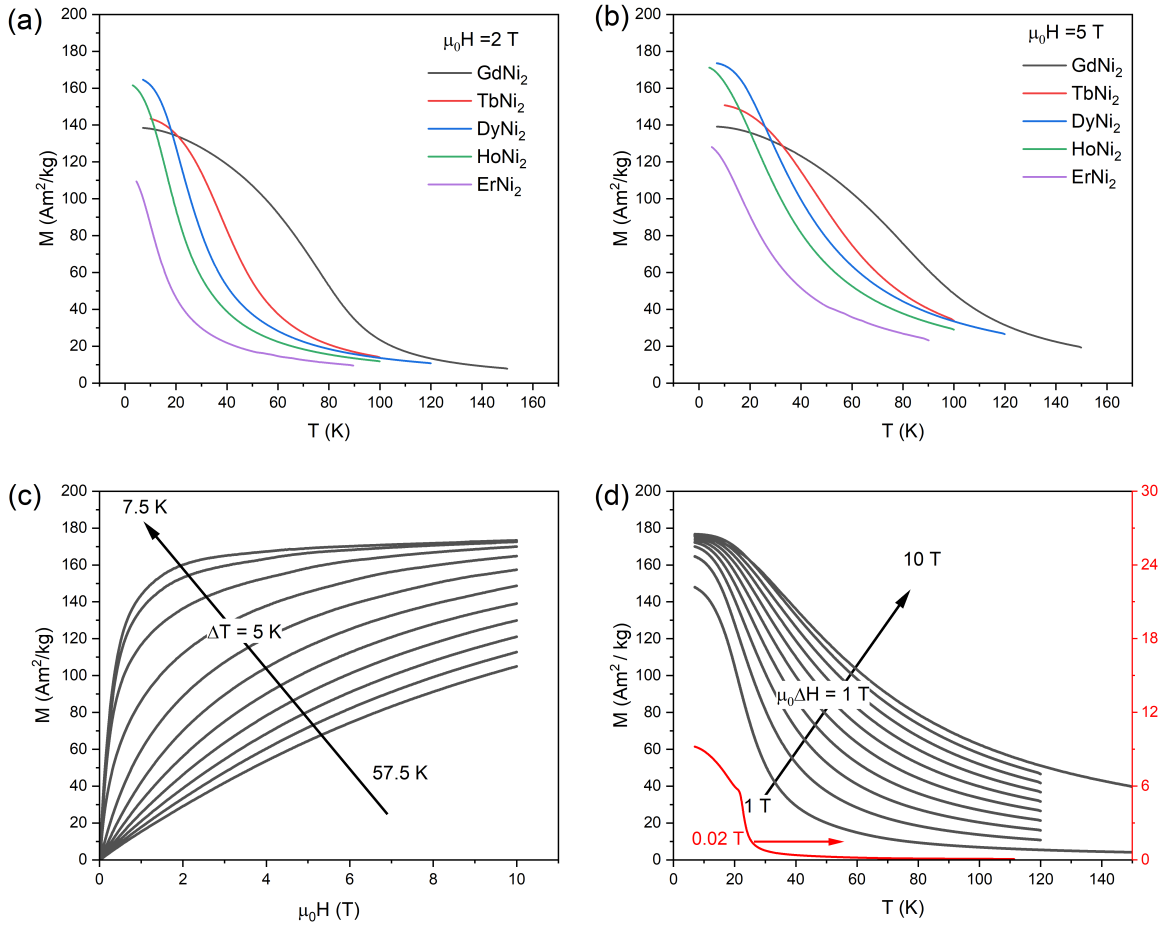

Figure 4.10: (a) (b) Magnetization as a function of temperature for RNi_2 samples in magnetic fields of 2 and 5 T, respectively. (c) (d) Magnetization as a function of magnetic fields and temperature for $DyNi_2$, respectively.

$$\frac{\chi}{\rho\,\mu_0} = \frac{\frac{C}{\rho\,\mu_0}}{T - T_C} = \frac{M}{\mu_0\,H} \tag{4.1}$$

where ρ is the density, C is the Curie-Weiss constant and is given by:

$$C = \frac{\mu_0\,\mu_B}{3k_B} N\,g^2\,J(J+1). \tag{4.2}$$

Let $\alpha = \rho\mu_0/C$ which is the slope of $\mu_0\chi^{-1}\,vs.T$, the effective magnetic moment μ_{eff} can be calculated by:

$$\mu_{eff} = g\sqrt{J(J+1)} = \frac{1}{\mu_B}\sqrt{\frac{3k_B\,M_R}{N_A\,\alpha}}, \tag{4.3}$$

with M_R as the molecular mass.

Figure 4.11 plots $\mu_0\chi^{-1}\ vs.T$ in magnetic fields of 1 T for the RNi_2 and RAl_2 Laves phases. The dashed lines are the Curie-Weiss fits, with their intercepts with the x-axis giving the paramagnetic Curie temperature. The calculated μ_{eff} of all the samples and their T_C are summarized together with the μ_{eff} of the corresponding heavy rare-earth ions in **Table 4.3**.

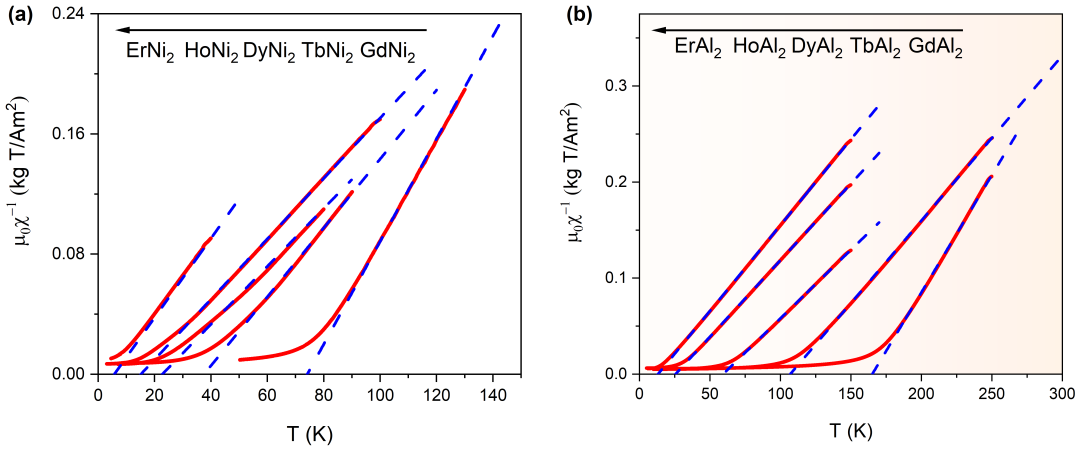

Figure 4.11: $\mu_0\chi^{-1}$ as a function of temperature in fields of 1 T with Curie-Weiss fits shown as blue dashed lines for (a) RNi_2 and (b) RAl_2.

Table 4.3: Effective magnetic moments of the RAl_2 and RNi_2 Laves phases, and the effective magnetic moments of rare-earth ions (taken from reference [39]).

Compounds	$\mu_{eff}(\mu_B/f.u.)$	μ_{eff} of free ions (μ_B)	$T_C(K)$
$GdAl_2$	8.32	8.9	165
$GdNi_2$	8.01		74
$TbAl_2$	9.98	9.8	107
$TbNi_2$	9.82		38
$DyAl_2$	11.12	10.6	60
$DyNi_2$	10.74		23
$HoAl_2$	10.46	10.4	26
$HoNi_2$	10.60		15
$ErAl_2$	9.97	9.5	13

$DyAl_2$ has the largest magnetic moment among all the samples, while $DyNi_2$ has the largest magnetic moment within the RNi_2 series. $GdNi_2$ shows the smallest magnetic moment among all the samples, while $GdAl_2$ shows the smallest magnetic moment within the RAl_2 series. All the samples show a magnetic moment similar to that of their corresponding rare-earth ions. The average magnetic moments of the RAl_2 and RNi_2 is 9.85 $\mu_B/f.u.$. The calculation of the magnetic moments conforms the large and similar magnetic moments of these heavy rare-earth Laves phases.

4.1.5 Magnetocaloric properties

Figure 4.12 shows the ΔS_T in magnetic fields of 2 and 5 T for RNi_2 and RAl_2. In both Laves phase series, significant larger maximum ΔS_T in lower temperature is observed. For example, maximum ΔS_T of $ErAl_2$ with a T_C of about 13 K reaches 40 J K^{-1} kg^{-1}, which is almost 5 times larger than that of $GdAl_2$ with a T_C of about 165 K in magnetic fields of 5 T. In magnetic fields of 2 T, $HoNi_2$ shows a ΔS_T of about 15 J K^{-1} kg^{-1}, while $GdNi_2$ shows a value that is just slightly larger than 5 J K^{-1} kg^{-1}. From the plots, it can be concluded that in both Laves phase series, maximum ΔS_T increases with decreasing T_C , except for $ErNi_2$ in the RNi_2 series showing a smaller ΔS_T and T_C than $HoNi_2$.

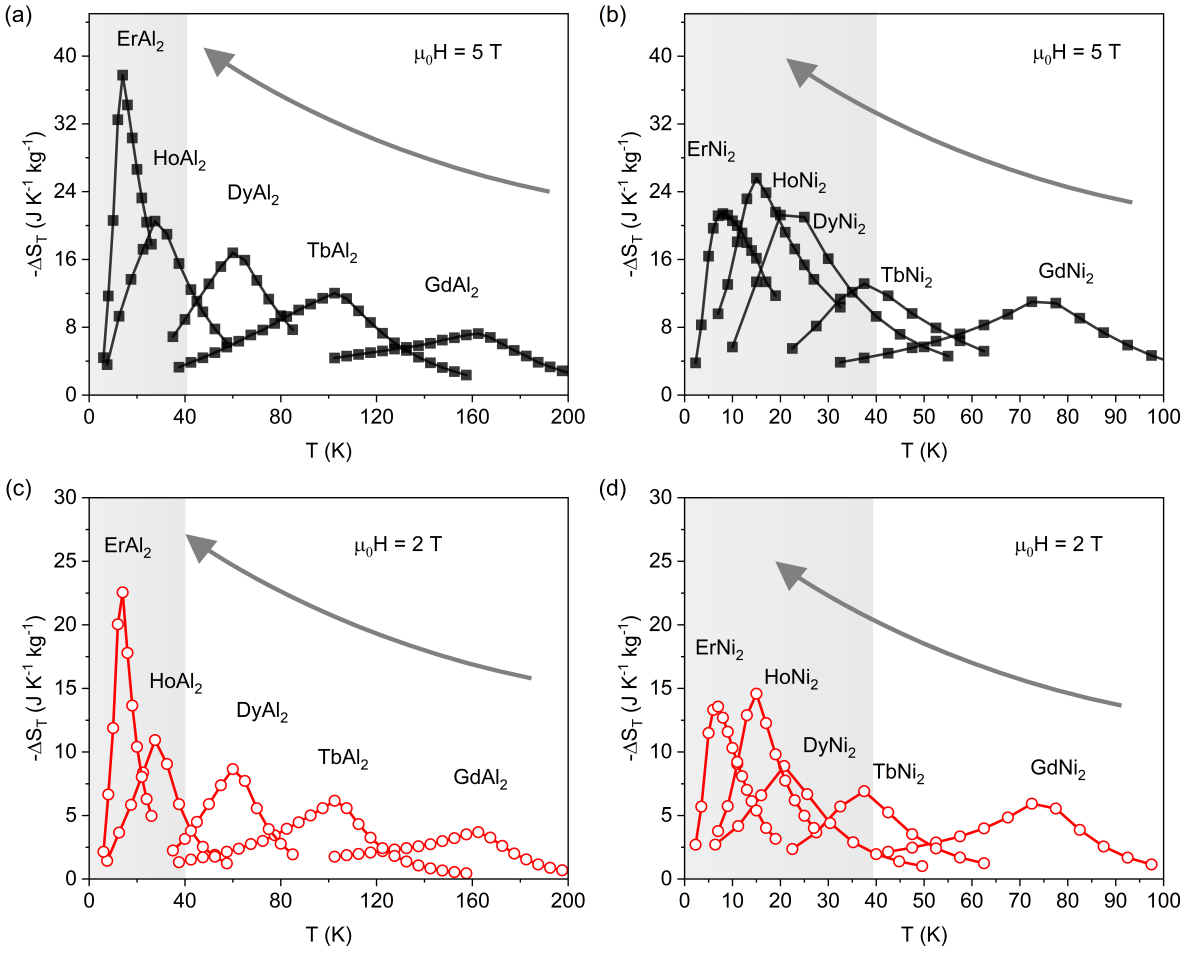

Figure 4.12: ΔS_T in magnetic fields of 5 T for RAl_2 (a) and RNi_2 (b), and 2 T for RAl_2 (c) and RNi_2 (d).

Though belonging to the second-order magnetocaloric materials, $ErAl_2$ exhibits a ΔS_T that is even slightly larger than that of the first-order magnetocaloric materials $ErCo_2$ with a ΔS_T of about 36 J K^{-1} kg^{-1}. This agrees with the conclusion in **Section 4.1** that second-order magnetocaloric materials can show the same ”giant” value of ΔS_T at low temperatures as first-order magnetocaloric materials.

In Dresden High Magnetic Laboratory of Helmholtz-Zentrum Dresden-Rossendorf, the adiabatic temperature changes were directly measured in pulsed fields of up to 2, 5, and 20 T. **Figure 4.13** (a) presents the time profiles of the magnetic fields and ΔT_{ad} for $HoNi_2$ at 15 K. Before and after field application, ΔT_{ad} returns to zero, which is a sign of a full reversibility of ΔT_{ad} . **Figure 4.13** (b) plots ΔT_{ad} as a function of magnetic fields of up to 2 and 5 T at 15 K. Both curves almost overlap each other in the region of $0 \sim 2$ T, indicating a full reversibility of the magnetocaloric effect. In addition, no obvious hysteresis is observed, which is a characteristic of the second-order MCE. These observations agree with the fact that $HoNi_2$ undergoes a second-order phase transition.

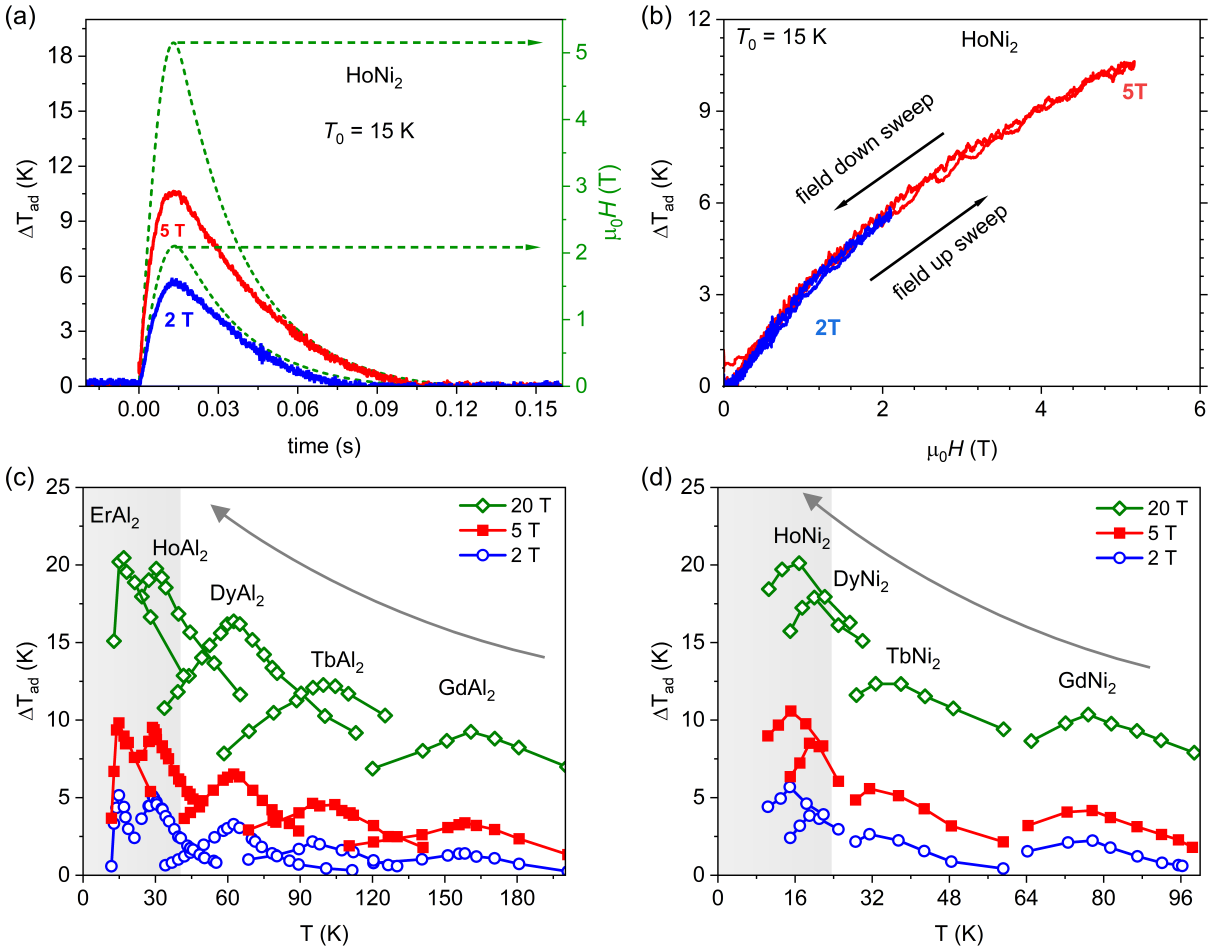

Figure 4.13: (a) Time dependencies of ΔT_{ad} and magnetic fields for the measurements in 2 and 5 T for the $HoNi_2$ sample at 15 K. (b) ΔT_{ad} of $HoNi_2$ as a function of magnetic fields up to 2 and 5 T. (c) (d) ΔT_{ad} as a function of temperature for RAl_2 and RNi_2 in magnetic fields of 2, 5, 20 T.

Figure 4.13 (c) and (d) plot the ΔT_{ad} of RAl_2 and RNi_2 (No data for $ErNi_2$ with a paramagnetic Curie temperature of 6 K due to the bad accuracy of the thermocouple below 10 K) in magnetic fields of 2, 5, and 20 T. Similar to what has been observed in the $\Delta S_T(T)$, the maximum ΔT_{ad} shows a significantly larger value at lower temperatures. Both $ErAl_2$ and $HoAl_2$ exhibit a ΔT_{ad} of above 5 K in magnetic fields of 2 T, being significantly larger than $GdAl_2$ with a ΔT_{ad} of about 1 K, and $GdNi_2$ with a ΔT_{ad} of about 2.5 K.

In addition to the analyses on ΔS_T and ΔT_{ad} , typical figures of merit, namely the RCP, the Q_{REV}^{max}, and the TEC(5 K) are studied as well. The results are plotted in **Figure 4.14**. No apparent trend of the RCP can be observed in both RAl_2 and RNi_2 series, whereas a clear increasing trend of Q_{REV}^{max} is observable in RAl_2 and RNi_2 in both magnetic fields of 2 and 5 T. Furthermore, contrary to the increasing trend of Q_{REV}^{max}, TEC(5 K) shows a decreasing trend.

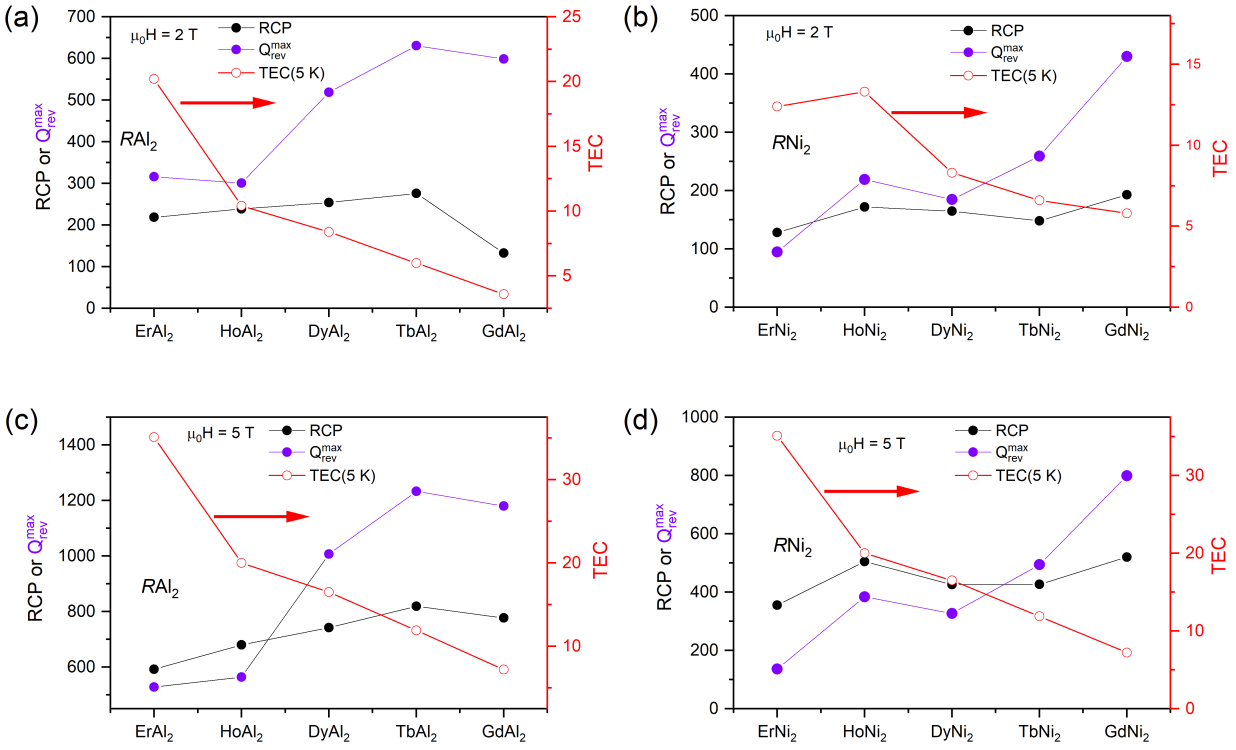

Figure 4.14: (a) (b) (c) (d) RCP, Q_{rev}^{max}, and TEC(5 K) as figures of merit for RAl_2 and RNi_2 in 2 and 5 T.

The above analyses demonstrate that, despite that all the heavy rare-earth Laves phases exhibit similar magnetic moments, their maximum ΔS_T and ΔT_{ad} can be significantly different. For the heavy rare-earth Laves phase RAl_2 and RNi_2 series, these two parameters are much larger at lower temperatures. Is this just coincidence, or a genuine behavior of the rare-earth-based magnetocaloric materials?

In search of answers, a literature review was conducted on the maximum ΔS_T and ΔT_{ad} of the rare-earth-based intermetallic compounds. The results on maximum ΔS_T and ΔT_{ad} in magnetic fields of 2 and 5 T are plotted in **Figure 4.15** (a) and (b), respectively. Data are taken from references [12, 23, 36, 89, 92, 97, 98, 108–151]. Large ΔS_T that exceed the reference polycrystalline Gd with a value of about 10 J K^{-1} kg^{-1} are observed below around 140 K. As the gray shadow indicates, "giant" values in second-order magnetocaloric materials such as HoB_2, $ErAl_2$, and TmGa are found. Like what is observed in the RAl_2 and RNi_2 series, the maximum ΔS_T shows an increasing trend with the decreasing Curie temperatures.

As against the numerous data on ΔS_T , only limited data on ΔT_{ad} of materials with a T_C below 100 K exist in the literature, mostly indirectly given by heat capacity measurements. Similar to what is observed in **Figure 4.15** (a), the maximum ΔT_{ad} in the cryogenic temperature range increases with the decreasing T_C .

Magnetocaloric materials with a T_C in the vicinity of 20 K show much larger ΔT_{ad} than materials with a T_C near 160 K. Moreover, from room temperature to around 160 K, an increasing trend of ΔT_{ad} with respect to decreasing T_C is not observed. In contrast, a decreasing trend is observed.

Based on the literature review, a genuine feature is observable: magnetocaloric materials can show a large magnetocaloric effect in cryogenic temperature, especially in the vicinity of the hydrogen condensation point (20 K), and two trends are summarized: (1) the maximum ΔS_T increases with decreasing T_C ; (2) the maximum ΔT_{ad} decreases near room temperature with decreasing T_C , but increases in the cryogenic temperature range.

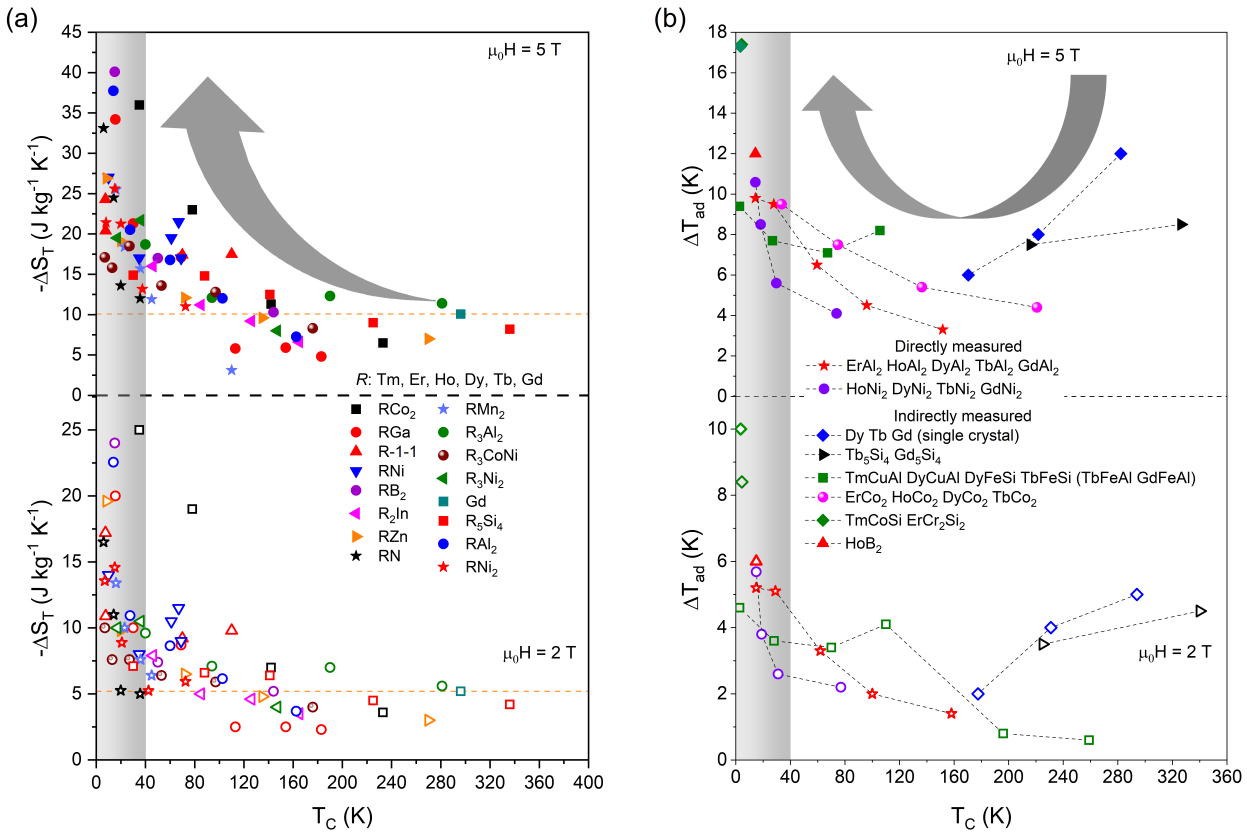

Figure 4.15: Maximum ΔS_T (a) and ΔT_{ad} (b) as a function of Curie temperature for heavy rare-earth-based magnetocaloric materials in magnetic fields of 2 and 5 T.

4.2 A theoretical approach on how cryogenic temperature influences magnetocaloric effect

4.2.1 Magnetic entropy and adiabatic temperature changes by mean-field approach

Recall eq. (2.14) in **Section 2.3.1**:

$$S_M(T,H) = N_M\, k_B \left[\ln\left(\frac{\sinh \frac{2J+1}{2J} y}{\sinh \frac{1}{2J} y} \right) - y B_J(y) \right] ,$$

where for ferromagnetic materials

$$y = \frac{g_J\, J \mu_B\, \mu_0 H + \frac{3J}{J+1} k_B\, T_C\, B_J(y)}{k_B\, T} ,$$

for paramagnetic materials

$$y = \frac{g_J\, J \mu_B\, \mu_0 H}{k_B\, T} .$$

In reference [146], this equation based on mean-field model demonstrates its application in calculating ΔS_T of a single crystalline Gd with good matching between theory and experiment. As a matter of fact, mean-field model is widely used in literature to interpret the magnetocaloric properties of rare-earth-based intermetallic compounds [2, 146, 152–156].

Equation (2.14) takes J, T, T_C, and g_J as variables. Focusing on studying the correlations between ΔS_T and T_C , the variables J and $g_J\, J$ are fixed. In the present work, parameters J and g_J are assumed to be 7.5 and 4/3, respectively. The theoretical magnetic moment μ is 10 μ_B given by

$$\mu = g_J\, J .$$

These parameters, namely J, T_C, and g_J correspond to $DyAl_2$, which is taken as an example in this section.

It should be mentioned that magnetocaloric effect is influenced by many factors, such as microstructure, stoichiometry, nature of phase transition, magnetic moment, and the sweeping rate of the magnetic fields [12, 28, 157]. Despite that mean-field model is a useful tool, it describes an idealized material without considering any extrinsic factors that influence the magnetocaloric effect. Intrinsic factors such as crystal field and spin fluctuation are also not considered.

Nevertheless, since the goal is to study the correlations between Curie temperature and maximum magnetocaloric effect to interpret the findings discovered in **Section 4.1.5** in the present work, factors other than T_C is out of consideration.

Figure 4.16 demonstrates the magnetization M, magnetic entropy S_M, magnetic heat capacity C_H, and magnetic entropy change ΔS_T as a function of temperature for T_C =60 K from mean-field theory. In 5 T,

the saturated magnetization is about $258\,\mathrm{A\,m^2\,kg^{-1}}$, showing a reasonable difference from the experimental data of about $211\,\mathrm{A\,m^2\,kg^{-1}}$ given by **Figure 4.9** (a). In **Figure 4.16** (b), S_M in zero field exhibits a kink, corresponding to the Curie point.

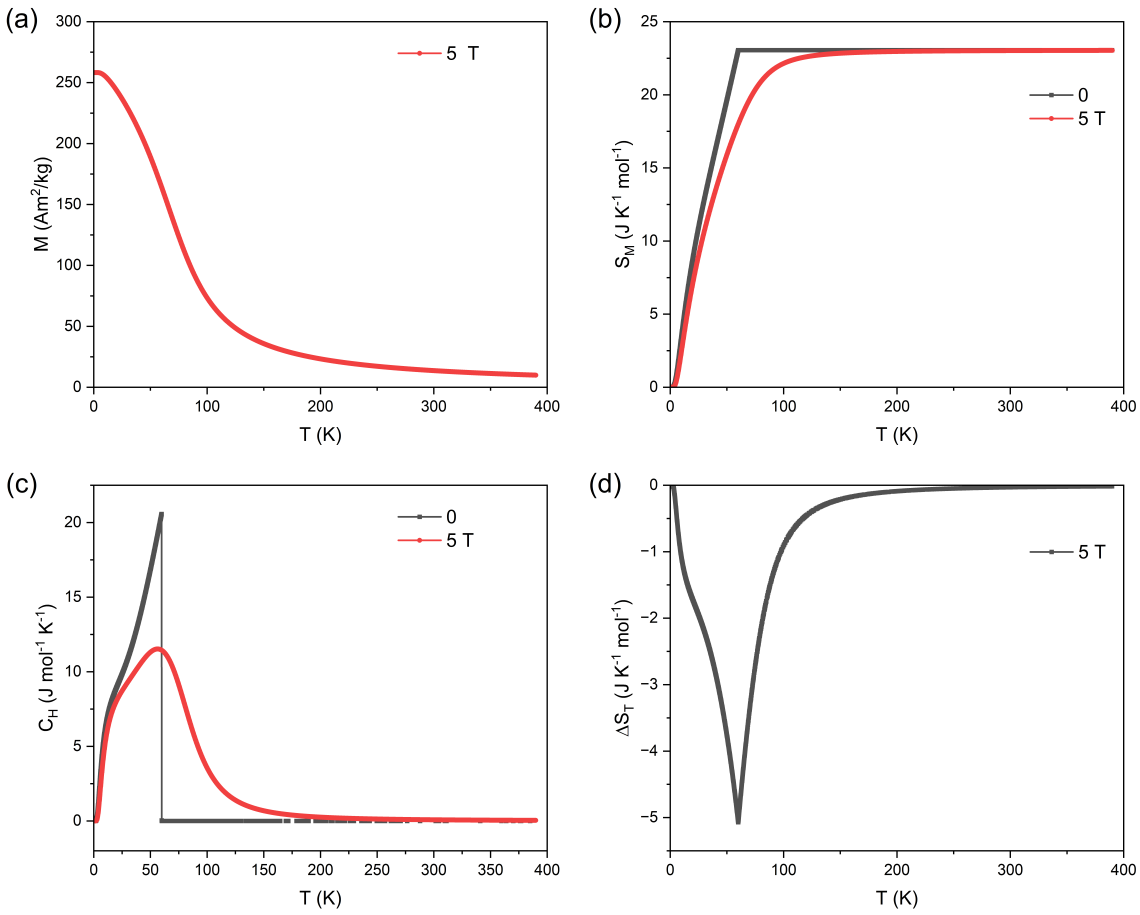

Figure 4.16: Magnetic and magnetocaloric properties from mean-field theory: (a) Magnetization as a function of temperature in magnetic fields of 5 T. (b) Magnetic entropy in magnetic fields of 0 and 5 T. (c) Magnetic heat capacity in magnetic fields of 0 and 5 T. (d) Magnetic entropy change in magnetic field of 5 T.

In zero field, the magnetic heat capacity C_H reaches about $20.5\,\mathrm{J\,K^{-1}\,mol^{-1}}$. C_H can be also approximated by [158]:

$$\frac{\Delta C_{p,H=0}}{N} = k_B \frac{5J(J+1)}{J^2+(J+1)^2}\,. \tag{4.4}$$

Let $J = 7.5$, $\Delta C_{p,H=0}$ is $20.6\,\mathrm{J\,K^{-1}\,mol^{-1}}$. This value is highly close to the value calculated in the present work, confirming the reasonableness of the mean-field calculation. The maximum ΔS_T given by the mean-field theory in magnetic fields of 5 T is about $5.1\,\mathrm{J\,K^{-1}\,mol^{-1}}$, which is reasonably larger than the experimental data of about $4.5\,\mathrm{J\,K^{-1}\,mol^{-1}}$ shown in **Figure 4.12**.

For the calculation of ΔT_{ad} , the total entropy $S_{tot}(T, H)$ curves need to be constructed. Since

$$S_{tot}(T, H) = S_M(T, H) + S_L(T) + S_e(T)\,,$$

lattice heat capacity is involved in the calculation of lattice entropy S_L. To calculate the volumetric lattice heat capacity C_V, Debye temperature (T_D) needs to be known. In the present work, T_D is estimated by the equation [159, 160]:

$$T_D^{RAl_2}(T, n) = \frac{[14 - n]T_D^{LaAl_2}(T) + n\,T_D^{LuAl_2}(T)}{14}\,, \tag{4.5}$$

where n is defined as the relative position of the rare-earth element in the rare-earth series. This equation gives an estimate of 373 K for the Debye temperature of $DyAl_2$.

Figure 4.17 shows the estimate of the volumetric heat capacity C_V for the RAl_2 Laves phase series at the Curie temperature. The estimated C_V at T_C lies in between C_V of $LaAl_2$, with a T_D of about 352 K, and $LuAl_2$, with a T_D of about 384 K.

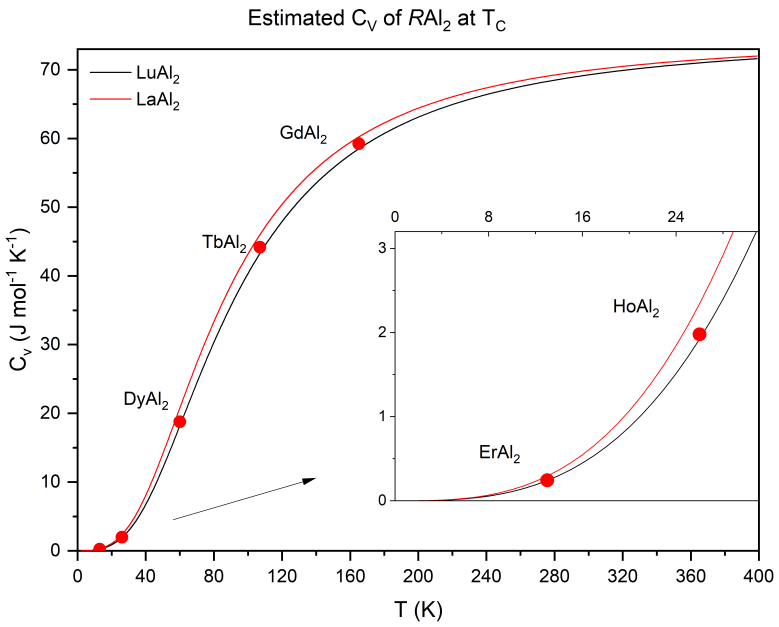

Figure 4.17: Estimated volumetric heat capacities of the RAl_2 Laves phases.

Figure 4.18 (a) plots the results of the total heat capacity in 0 and 5 T calculated from mean-field theory. Electronic heat capacity is neglected since they only contributes to the total heat capacity significantly at sufficiently low temperatures [161]. In magnetic fields of 5 T, the peak on the heat heat capacity curve is not clear anymore. This result agrees with the heat capacity measurements discussed in reference [35]. Moreover, in zero fields, above T_C , the heat capacity curve overlaps with the lattice heat capacity. This is due to that the material above T_C is in paramagnetic state where $\partial S_M/\partial T$ ($C_M = T\partial S_M/\partial T$) is small in small fields. While in magnetic fields of 5 T, even in the vicinity above T_C , the total heat capacity is significantly larger than the lattice heat capacity.

Figure 4.18 (b) exhibits the total entropy curve $S_{tot}(T, H)$ near transition temperature. Based on **Equation (2.18)**, both ΔS_T and ΔT_{ad} can be obtained from the $S_{tot}(T, H)$ curves, as indicated by the arrows

in **Figure 4.18** (b). **Figure 4.18** (c) shows the adiabatic temperature change ΔT_{ad} in magnetic fields of 5 T. The maximum value is about 10 K, significantly larger than the experimental data of about 6 K seen in **Figure 4.13** (c). This difference is expected because the intrinsic factors such as heat capacities from electrons and crystal fields, and extrinsic factors such as microstructure, and secondary phases are out of consideration.

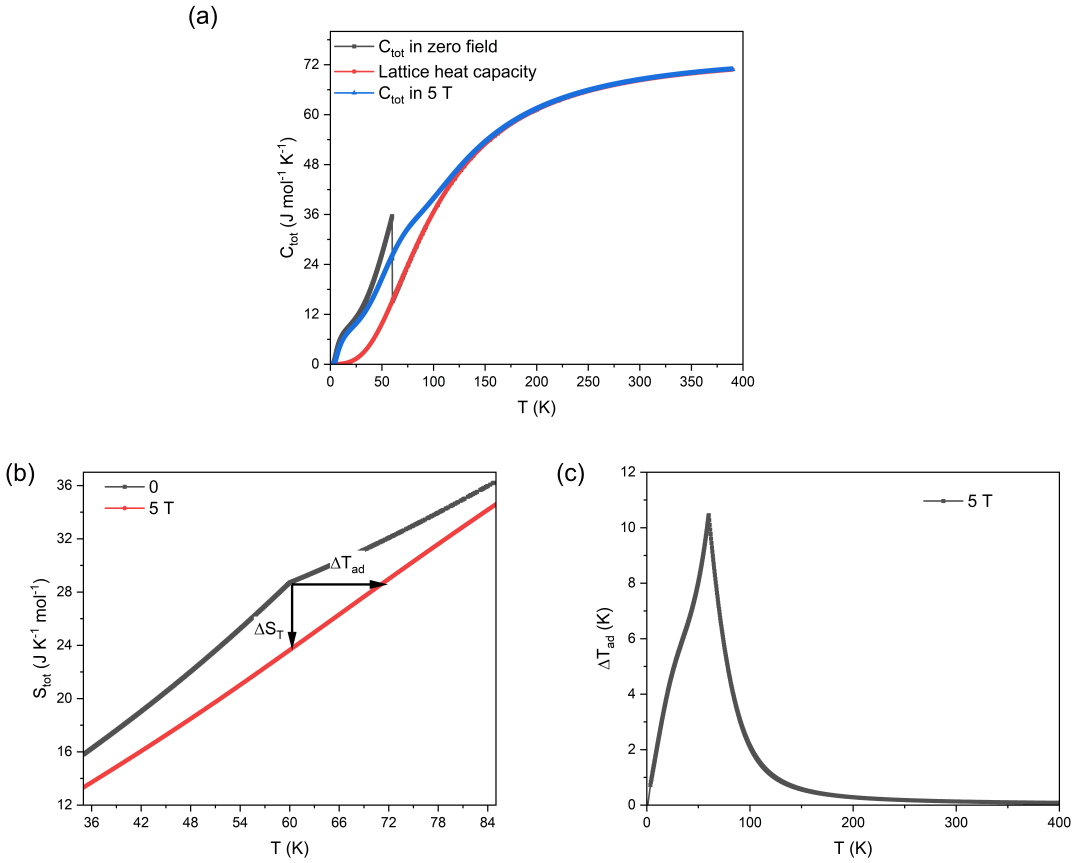

Figure 4.18: (a) Total heat capacity in 0 and 5 T and lattice heat capacity calculated from mean-field theory and Debye model. (b) Total entropy around transition temperature from mean-field theory. (c) Calculated adiabatic temperature change from mean-field theory.

In the above, by comparing the experimental and theoretical results of the ΔS_T and ΔT_{ad} of $DyAl_2$, reasonableness of the mean-field approach used in the present work is confirmed. Now, let us focus on the physical question: how does the maximum ΔS_T and ΔT_{ad} correlate with T_C ?

To answer this question, an idealized "$DyAl_2$"-like material system is hypothesized. In the hypothetical "$DyAl_2$"-like material system, only T_C varies, with the other parameters staying constant. ΔS_T and ΔT_{ad} for the samples in the hypothetical "$DyAl_2$"-like material system are shown in **Figure 4.19**.

Agreeing with the conclusion drawn from **Figure 4.15** (a), the maximum ΔS_T increases with the decreasing T_C . Near room temperature, the increasing trend is rather gentle. However, the increasing trend becomes sharper and sharper towards a lower and lower temperature. Especially in the vicinity of 20 K, we see a large jump of ΔS_T with respect to the decreasing T_C .

Compared to ΔS_T , an increasing trend is not observed near room temperature in **Figure 4.19** (b). On the contrary, the calculation confirms the decreasing trend discovered from **Figure 4.15** (b). As displayed in the inset of **Figure 4.19** (b), the deceasing trend is rather small. However, around 160 K, the decreasing trend turns into an increasing trend. A sharp increasing trend around 20 K is observable as well, agreeing with the conclusion made from **Figure 4.15** (b).

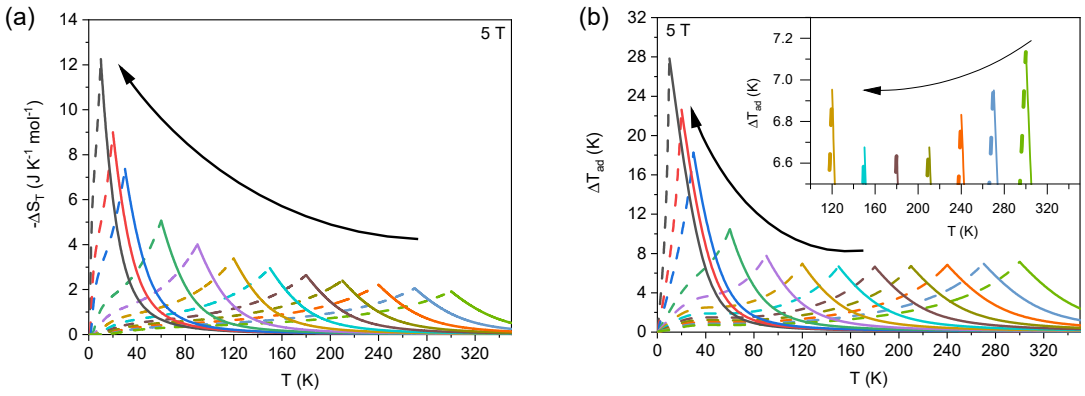

Figure 4.19: (a) (b) Magnetic entropy and adiabatic temperature changes for a hypothetical "$DyAl_2$"-like material system. The inset in (b) shows the enlarged area from near room temperature down to 100 K.

To sum up, based on a mean-field approach, the discoveries that ΔS_T and ΔT_{ad} can be "giant" near the condensation point of hydrogen and that both of them undergo an increase trend in cryogenic temperature range are theoretically interpreted. To understand these discoveries in intuitive ways, one can think like these:(1) As illustrated in **Figure 4.20** (a), the lower the temperature, the weaker the thermal motion of the magnetic moments. Therefore, the magnetic moments are more easily aligned by the external magnetic field. (2) As illustrated **Figure 4.20** (b), the lower the temperature, the smaller the heat capacity, the larger the temperature change, as

$$dQ = C_{tot}\frac{dT}{T}\,. \tag{4.6}$$

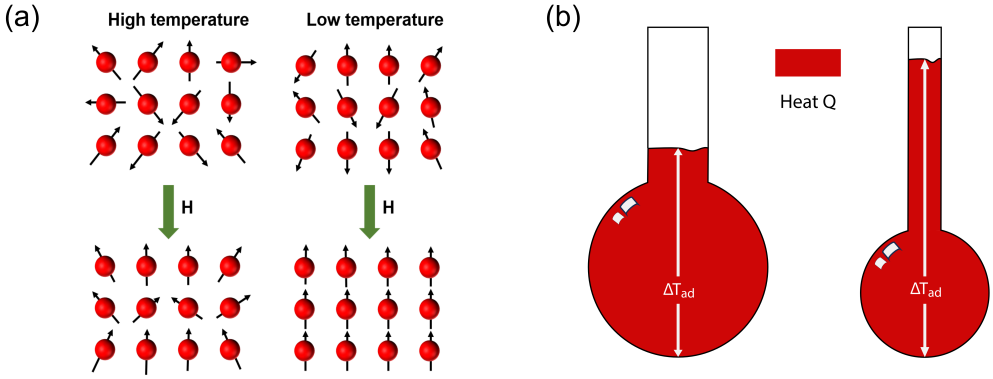

Figure 4.20: Schematic plot showing how thermal motion (a) and heat capacity (b) act on magnetocaloric effect.

4.2.2 Power laws with respect to external field and Curie temperature

introduction power laws

In the section above, the correlations in between the maximum ΔS_T and ΔT_{ad} , and the Curie temperatures, are studied. This section focuses on the pow laws of the maximum ΔS_T and ΔT_{ad} with respect to T_C and H. The approximated power laws offer a straightforward way of understanding the physical question of how ΔS_T and ΔT_{ad} correlate with magnetic field H and Curie temperature T_C.

$H^{2/3}$ power law

As a matter of fact, the correlation between ΔS_T and H has already been well studied in references [2, 155, 162–167]. Based on the mean-field theory, the relation between ΔS_T and H is given as:

$$\Delta S_T = \alpha H^{\frac{2}{3}} , \tag{4.7}$$

where α is a constant.

According to Kuz'min *et al.*[163], a correction is needed for spatial inhomogeneity of real materials [163]. The equation to calculate entropy S

$$S = -\frac{\partial F}{\partial T} , \tag{4.8}$$

Based on eq. (2.43) and using the equilibrium condition $\partial F/\partial T = 0$, S is then given by:

$$S = -\frac{\partial F_0}{\partial T} - \alpha_0 M^2 . \tag{4.9}$$

The magnetic entropy change ΔS_T is then

$$\Delta S_M(H) = \alpha_0 (M_i^2 - M_f^2) , \tag{4.10}$$

where M_i and M_f is the magnetization at $H = 0$ and H, respectively.

Above T_C, M_i is zero. Below T_C , there is a spontaneous magnetization, which is

$$M_i = \sqrt{\frac{\alpha_0}{2\beta}} \qquad T \leq T_C. \tag{4.11}$$

For calculating M_f^2, let's rewrite eq. (2.47) to

$$M^3 + \frac{\alpha_0}{2\beta}(T - T_C)M - \frac{H}{4\beta} = 0 \tag{4.12}$$

The discriminant Δ to this cubic equation is

$$\begin{aligned} \Delta &= \sqrt{\frac{H^2}{64\beta^2} + \frac{\alpha_0^3 (T - T_C)^3}{216\beta^3}} , \\ \sqrt{\Delta} &= \frac{H}{8\beta} \sqrt{1 + \frac{32\beta}{H^2} \frac{\alpha_0^3 (T - T_C)^3}{27\beta^3}} . \end{aligned} \tag{4.13}$$

Since $\frac{\alpha_0(T-T_C)}{\beta}$ is small, applying the approximation $(1+x)^n \approx 1+nx$, $\sqrt{\Delta}$ can be approximated as:

$$\sqrt{\Delta} \approx \frac{H}{8\beta} + \frac{4b}{H}\frac{\alpha_0^3(T-T_C)^3}{27\beta^3}. \tag{4.14}$$

Neglecting the small term

$$\frac{4b}{H}\frac{\alpha_0^3(T-T_C)^3}{27\beta^3}$$

when necessary, the solution is:

$$M = \left(\frac{H}{4\beta}\right)^{\frac{1}{3}} - \frac{\alpha_0(T-T_C)}{3\beta}(\frac{4\beta}{H})^{\frac{1}{3}}. \tag{4.15}$$

M^2 is then

$$M^2 = \left(\frac{H}{4\beta}\right)^{\frac{2}{3}} + \frac{\alpha_0}{3\beta}(T-T_C) + \left[\frac{\alpha_0(T-T_C)}{3\beta}(\frac{4\beta}{H})^{\frac{1}{3}}\right]^2 \tag{4.16}$$

Neglecting the last term, M^2 is given as

$$M^2 = \left(\frac{H}{4\beta}\right)^{\frac{2}{3}} + \frac{\alpha_0}{3\beta}(T-T_C). \tag{4.17}$$

Put M^2 back to eq. (4.10), ΔS_T is given by:

$$\Delta S_T = -\alpha_0\left(\frac{H}{4\beta}\right)^{\frac{2}{3}} + \begin{cases} \frac{\alpha_0^2}{6\beta}(T_C - T) & T < T_C \\ \frac{\alpha_0^2}{3\beta}(T-T_C) & T > T_C. \end{cases} \tag{4.18}$$

For spatial homogeneous sample, this equation becomes $\Delta S_T = -\alpha_0(\frac{H}{4\beta})^{\frac{2}{3}}$.

The correlation between ΔT_{ad} and H was also well-studied in references [2, 146, 155, 168, 169]. Since $\Delta T_{ad} \approx \frac{T\Delta S_T}{C_H}$, ΔT_{ad} should also follow the $H^{2/3}$ relation, which is

$$\Delta T_{ad} \propto H^{\frac{2}{3}}. \tag{4.19}$$

$T_C^{-2/3}$ and $T_C^{1/3}$ relations

Compared to the well studied $H^{2/3}$ relations, the correlations between ΔS_T , ΔT_{ad} , and T_C , however, are much less studied. One of the reasons is that, it is difficult to obtain a material series which only varies in T_C , with the other properties staying constant to focus on the relation between ΔS_T , ΔT_{ad} , and T_C only.

Oesterreicher and Parker are the first ones who interpreted the correlation between ΔS_T and T_C in 1984 [155] as:

$$\Delta S_T \propto T_C^{-\frac{2}{3}}. \tag{4.20}$$

This linear relation was also mentioned in reference [2]. In 2010, Belo *et al.* re-discovered this linear relation combining Landau theory and mean-field theory [154], with solid experimental data covering a large temperature range. **Figure 4.21** shows the experimental data that supports this linear relationship. Among the material systems of which their maximum ΔS_T showing a strong linear correlation with $T_C^{-2/3}$, the Laves phases $Gd_{1-x}Tb_xCo_2$, RCo_2, and $Dy(Co_{1-x}Fe_x)_2$ demonstrate that this linear relation can cover a large temperature range, i.e. from near room temperature to cryogenic temperatures.

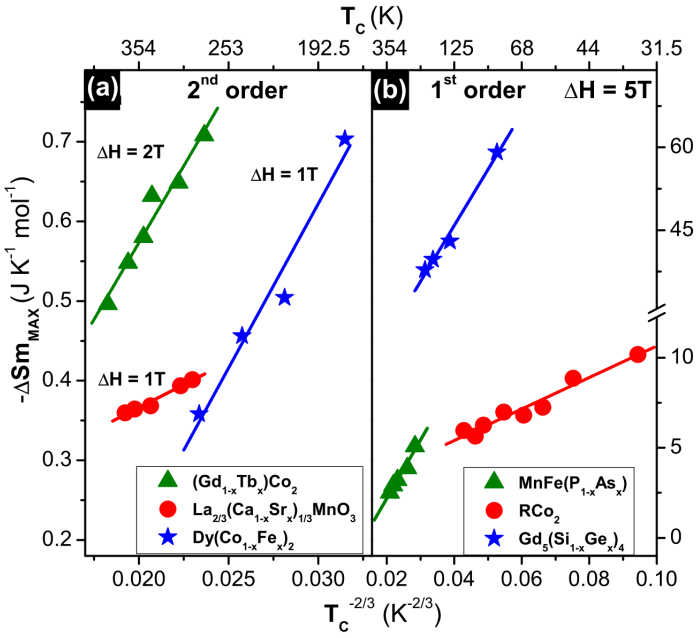

Figure 4.21: Experimental validation of the linear dependence of the maximum ΔS_T on $T_C^{-2/3}$. Picture is taken from [154]

Compared to the power laws mentioned above, the power law between the maximum ΔT_{ad} and T_C were barely mentioned till the work reported in reference [146]. The relation between ΔT_{ad} and T_C can be written as: $\Delta T_{ad}^{max} \propto \alpha T_C^{\frac{1}{3}} + \beta T_C^{-\frac{1}{3}}$, where α and β are constants. At high temperatures, $T_C^{\frac{1}{3}}$ is much larger than $T_C^{-\frac{1}{3}}$. Neglecting the $T_C^{-\frac{1}{3}}$ term, a power law can be obtained:

$$\Delta T_{ad}^{max} \propto \alpha T_C^{\frac{1}{3}}. \tag{4.21}$$

This power law implies that the maximum ΔT_{ad} decreases with decreasing Curie temperature. So far, it has not been validated with experimental data.

Validation of power laws

An approximation of the correlation between ΔS_T^{max} and T_C was proposed by Oesterreicher and Parker, re-discovered by Belo *et al.* [154] as:

$$\Delta S_T^{max} = -\frac{3}{2} R\, J(J+1) \left(\frac{10}{9} \frac{g_J \mu_B H}{[(J+1)^2 + J^2] k_B T_C} \right)^{\frac{2}{3}} \tag{4.22}$$

Figure 4.22 (a) compares the ΔS_T^{max} with respect to T_C calculated from this approximation equation and directly from mean-field approach. Near room temperature, both approaches match well with each other.

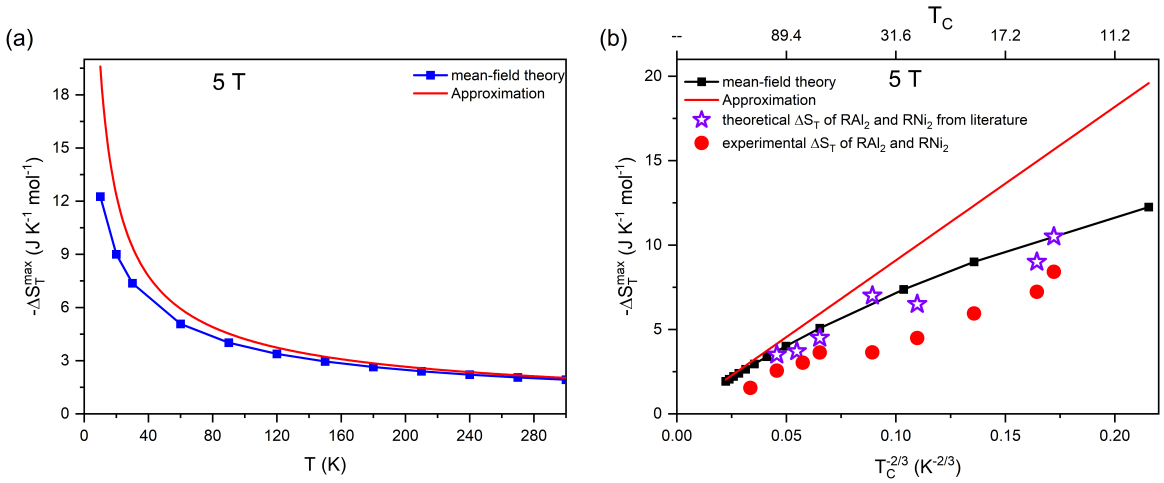

Figure 4.22: (a) Comparing ΔS_T^{max} with respect to T_C from the mean-field approach and the approximation equation from [154]. (b) Comparing ΔS_T^{max} with respect to $T_C^{-2/3}$ from the mean-field approach, the approximation equation from [154], the experimental data in the present work, and the theoretical data taken from references [159, 170].

However, below 120 K, the approximated data start to deviate from the directly calculated data, which poses a question about the validity of the linear relation $\Delta S_T^{max} \propto T_C^{-2/3}$ at low temperatures. **Figure 4.22** (b) plots the directly calculated and approximated data of ΔS_T *vs.* $T_C^{-2/3}$. In agreement with **Figure 4.22** (a), near room temperature, the directly calculated data exhibit excellent linearity, while in cryogenic temperature range, the directly calculated data start to shift away from the linear relation, and below 20 K, the linear relation is completely destroyed.

From **Figure 4.22** (b), the directly calculated data from the mean-field approach in the present work is compared with the experimental data from the present work and the theoretical data from references [159, 170] with the crystal field taken into consideration. ΔS_T calculated from present work are in good agreement with the theoretical data taken from literature. The values from literature shows a linear relation above 12 K as well, agreeing with the $T_C^{-2/3}$ linear approximation proposed by [155] and the directly calculated data from the present work. The experimental data show smaller values than the theoretical data. It is reasonable to consider that the samples in the present work are polycrystal. In line with the calculations, the experimental data show a rough linear relation with $T_C^{-2/3}$.

Figure 4.23 plots ΔT_{ad}^{max} directly calculated from mean-field theory in the present work with respect

to $T_C^{1/3}$. The result confirms that the power law of $\Delta T_{ad}^{max} \propto T_C^{1/3}$ is only valid near room temperature, as we can see from the inset that the linear decreasing trend turns to be an increasing trend at around 120 K. Instead of decreasing linearly with $T_C^{1/3}$, it is observed that ΔT_{ad}^{max} show an increasing trend with respect to $T_C^{1/3}$. This is due to the fact that at low temperatures, the Dulong-Petit law does not hold true anymore. Instead of being constant, lattice heat capacity will have undergone a sharp decrease towards low temperatures. Indicated by the approximation equation $\Delta T_{ad} = T\Delta S_T / C_{tot}(H)$, an increasing trend in sufficiently low temperature range is expected.

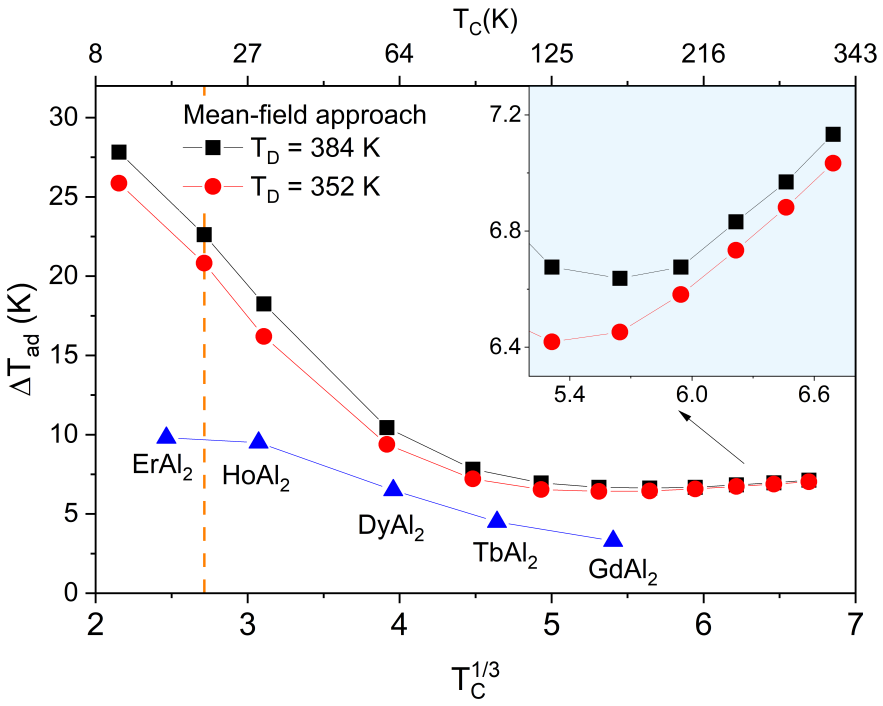

Figure 4.23: ΔT_{ad}^{max} directly calculated from mean-field theory and experimental ΔT_{ad}^{max} of the RAl_2 and RNi_2 Laves phases with respect to $T_C^{1/3}$.

The above work examines the power law of $\Delta S_T^{max} \propto T_C^{-2/3}$ with theoretical calculations and experimental data, and the power law of $\Delta T_{ad}^{max} \propto T_C^{1/3}$ with theoretical calculations. According to the theoretical calculations, the linearity of $\Delta S_T^{max} \propto T_C^{-2/3}$ can remain down to 20 K, agreeing with the experimental data of RAl_2 and RNi_2, which show a clear linear relation from about 160 K down to 13 K. However, from the theoretical calculations, the power law of $\Delta T_{ad}^{max} \propto T_C^{1/3}$ is only valid near room temperature.

4.3 Design magnetocaloric materials for hydrogen liquefaction with light rare-earth Laves phases

4.3.1 Analysis on the criticality of rare-earth elements

If the criticality of the raw materials were ignored, heavy rare-earth-based magnetocaloric materials would be excellent candidates for magnetocaloric hydrogen liquefaction. As shown in **Figure 4.15** (a) and (b), they show larger ΔS_T and ΔT_{ad} within the temperature range of $20 \sim 77$ K. However, when used on a large scale, criticality cannot be ignored [171].

Heavy rare-earth elements are highly critical in resources [171, 172]. **Figure 4.24** shows the relative abundances of the rare-earth elements, categorized into non-heavy rare-earth elements with non-zero magnetic moments (Ce, Pr, Nd, and Sm), and heavy rare-earth elements with non-zero magnetic moments (Gd, Tb, Dy, Ho, Er, Tm, and Yb), and heavy rare-earth elements with zero magnetic moments (Lu), and Eu (whether Eu belongs to light rare-earth elements or not is inconsistent in literature, and sometimes it is called ”medium rare-earth element [38]”). Ni, Co, and Cu are also included in the plot for comparison. Heavy rare-earth elements such as Tm and Lu have poor abundances. The total abundance of all the heavy rare earths combined is not as abundant as the light rare-earth element Nd alone. Nd has an abundance similar to that of Cu, and Ce is even more abundant than Ni.

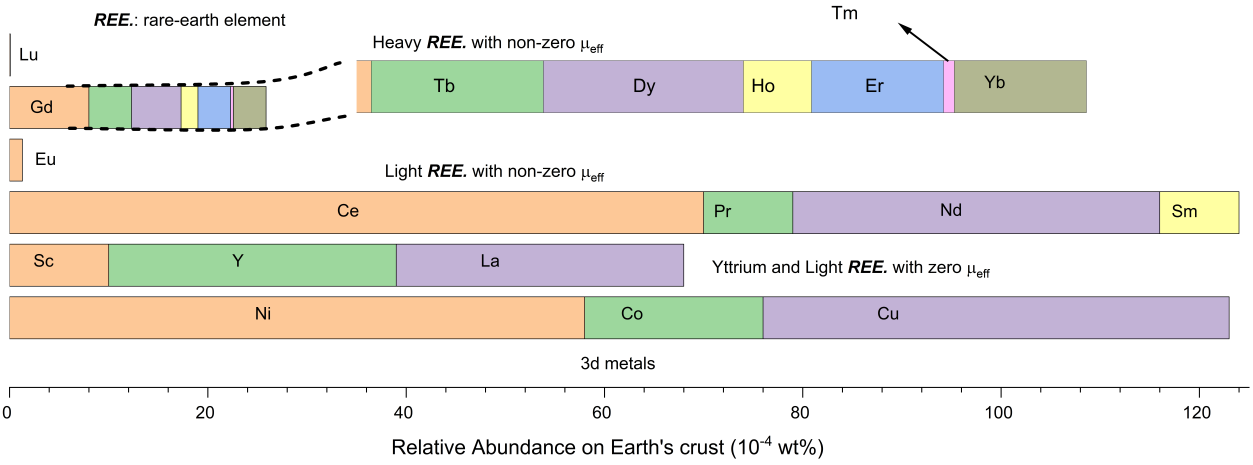

Figure 4.24: Relative abundances of Ni, Co, Cu, and the rare-earth elements categorized into non-heavy rare-earth elements with zero magnetic moments (Sc, Y, La), light rare-earth elements with non-zero magnetic moments (Ce, Pr, Nd, Sm), Eu, and heavy rare-earth elements with non-zero magnetic moments (Gd, Tb, Dy, Ho, Er, Tm, Yb), and zero magnetic moments (Lu). Data are taken from [173].

The criticality of one material can be reflected in part by its price. **Figure 4.25** categorizes the prices of the elements into five groups. Y and Ce are the cheapest rare-earth elements, light rare-earth elements Nd and Sm are affordable, while heavy rare earths Tb, Dy, Ho, Er, Tm, Yb, and Lu are expensive.

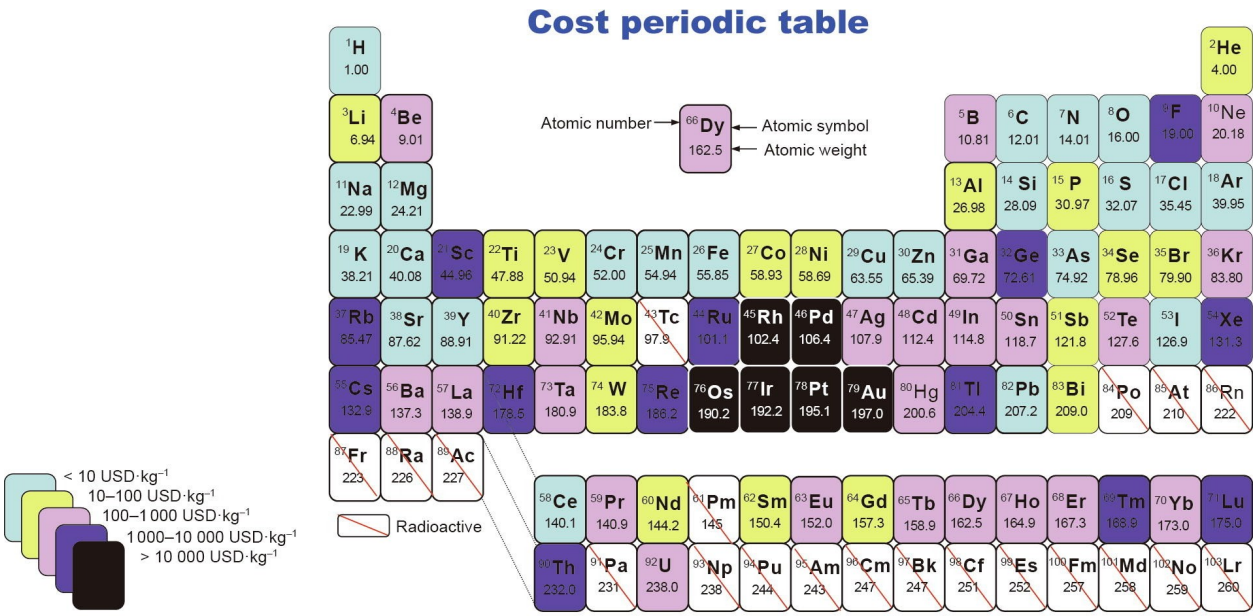

Figure 4.25: The periodic table of the elements assigned to five different cost categories. Picture is taken from [174].

Figure 4.26 shows the price of the rare-earth oxides with a purity higher than 99.5 wt% in the years of 2018 and 2021 in the global market. the oxides of the rare-earth elements Y, La, and Ce are very cheap, with their prices all below 3 $/kg. The oxides of the light rare-earth elements Pr and Nd are less cheap. On the contrary, the oxides of the heavy rare-earth elements Tb and Dy are highly expensive, with their prices all surpassing 175 $/kg and varying abruptly.

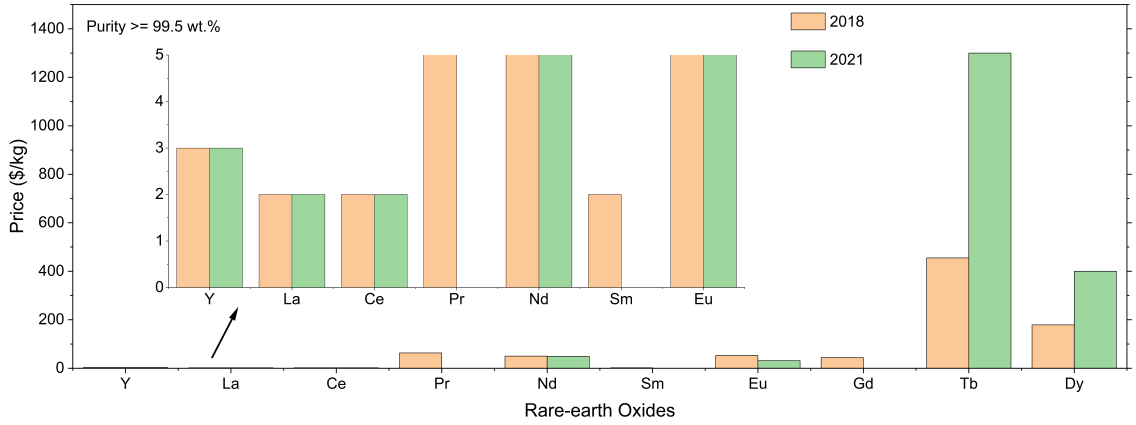

Figure 4.26: Prices of the rare-earth oxides (Y, La, Ce, Pr, Nd, Sm, Eu, Gd, Tb, Dy) in year 2018 and 2021. Data are taken from references [171, 175]

For sure, criticality is much more than just simple geological abundances. Other factors such as mining, hazardous by-products, benefaction, separation (and their social and ecological consequences along this value

chain), trade restrictions, geopolitics, and monopolistic supply in terms of demand vs. supply, need to be studied and quantified in terms of life-cycle-analysis and life-cycle-costing [176]. Nevertheless, the analysis above on the criticality put a question on the feasibility of using heavy rare-earth based magnetocaloric materials for hydrogen liquefaction in a viable industrial scale. The lower criticality of the light rare-earth elements makes their alloys appealing for the application of magnetocaloric hydrogen liquefaction in a large scale.

As already mentioned in **Chapter 1**, light rare-earth-based magnetocaloric materials generally show a weaker magnetocaloric effect than their heavy rare-earth counterparts due to that light rare-earth ions possess smaller magnetic moments. **Figure 4.27** compares the effective magnetic moments of the light rare-earth ions and the heavy rare-earth ions. Pr^{3+} has the largest magnetic moment of 3.54 μ_B among the light rare-earth elements. In contrast, Yb^{3+} shows the smallest magnetic moment among the heavy rare-earth elements in **Figure 4.27** but its magnetic moment still exceeds 4 μ_B. Dy^{3+} and Ho^{3+} even have magnetic moments of more than 10 μ_B, almost three times as large as Pr^{3+}.

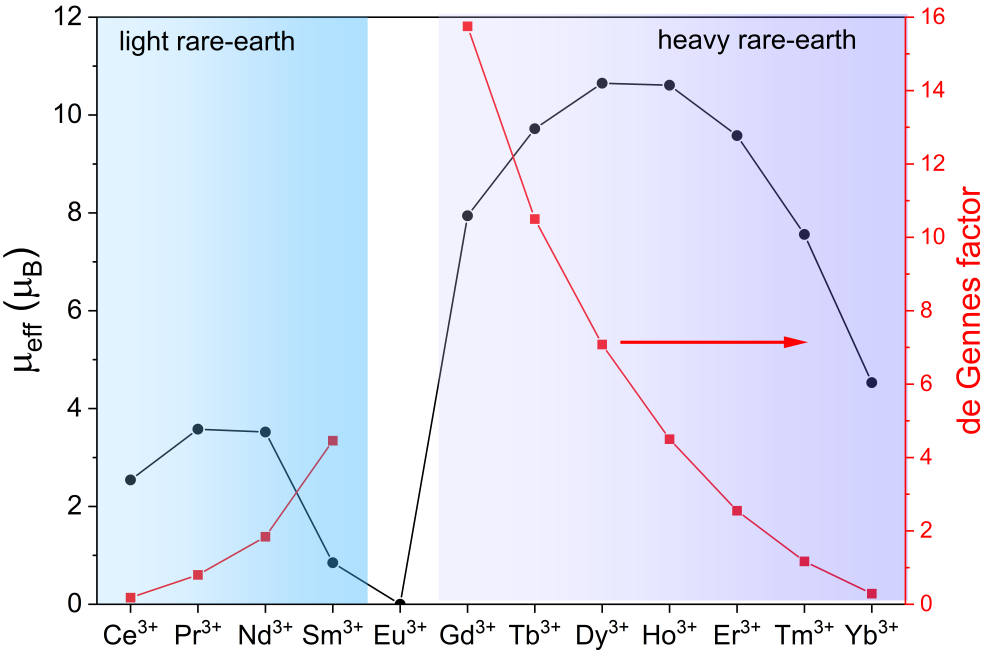

Figure 4.27: Magnetic moments and de Gennes factors of rare-earth ion. Data are taken from [39].

In **Section 4.2.1**, the increasing trend trends of the maximum ΔS_T and ΔT_{ad} with respect to a decreasing T_C are demonstrated. Although light rare-earth-based magnetocaloric materials generally show a weaker magnetocaloric effect in comparison with their heavy rare-earth counterparts, are their magnetocaloric effects strong enough in cryogenic temperature range for hydrogen liquefaction? In the next chapter, the magnetocaloric effect of the light rare-earth Laves phases $PrAl_2$ and $NdAl_2$ will be evaluated.

4.3.2 Magnetocaloric effect of light rare-earth Laves phases

$NdAl_2$ amd $PrAl_2$ samples were prepared as introduced in **Section 3.1**. **Figure 4.28** (a) and (b) present the BSE images of both samples. No significant amount of impurities is observed. There exists tiny amount of rare-earth rich phases, as the bright spots indicates. The black dots on the images are confirmed to be hole, possibly formed during polishing process.

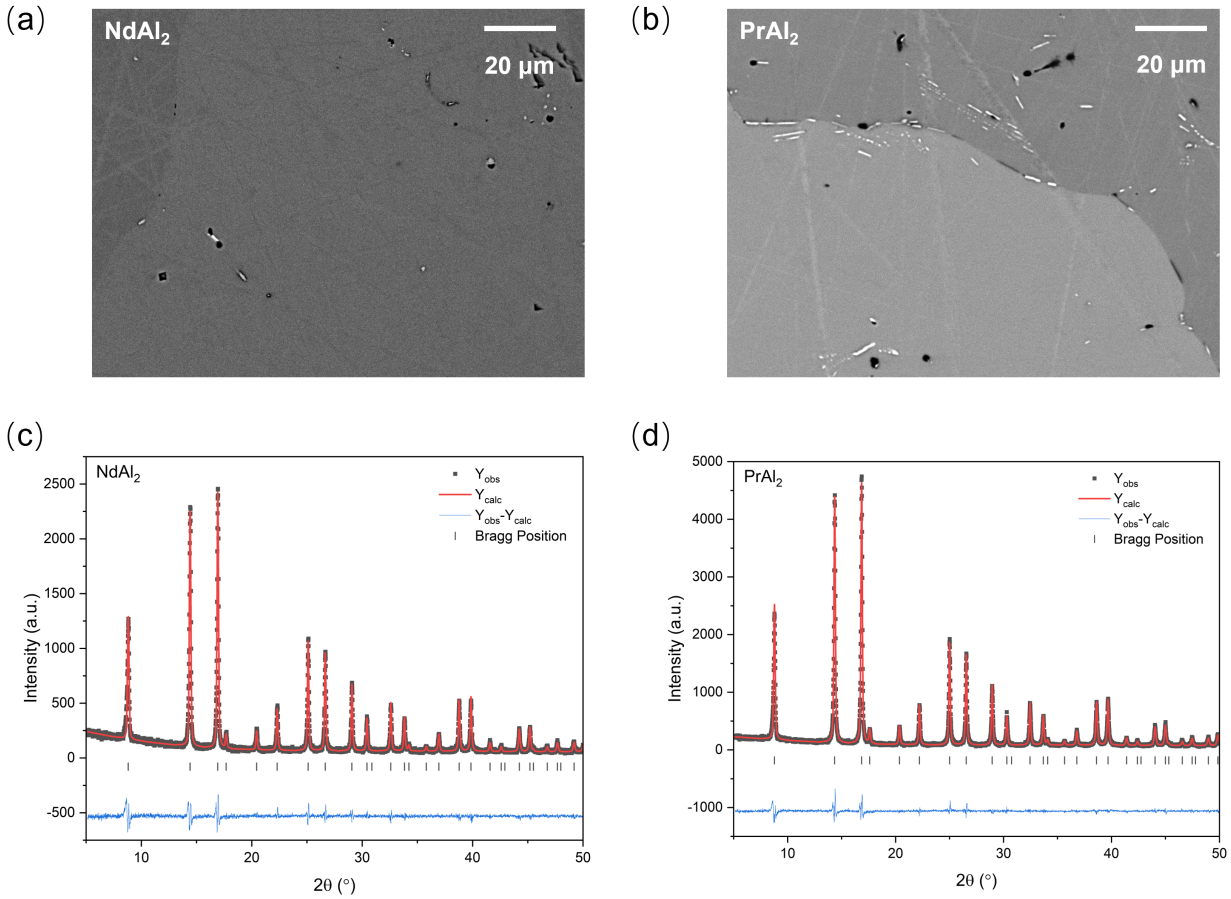

Figure 4.28: (a) (b) BSE images of $NdAl_2$ and $PrAl_2$. (c)(d) XRD patterns and the results of Rietveld refinements.

The quality of the samples was further confirmed by the XRD measurements. **Figure 4.28** (c) and (d) show the XRD patterns of both samples together with the results of the Rietveld refinements. Both of the samples are confirmed by the XRD measurements to crystallize in the cubic $MgCu_2$-type structure. The lattice constant of the $NdAl_2$ sample is given by the Rietveld refinement to be 7.99641 Å, and that of $PrAl_2$ is 8.02931 Å. No obvious peaks from impurities are observed for both samples. Both the BSE and XRD measurements confirm the high quality of the samples $NdAl_2$ and $PrAl_2$.

Figure 4.29 (a) (b) (c) (d) shows the magnetization curves for both of the samples. The $M(T)$ curves in magnetic fields of 0.02 T indicate that the Curie temperature of $NdAl_2$ is around 80 K, and that of $PrAl_2$ is around 30 K. In both $M(T)$ and $M(H)$ curves, it can be seen that the magnetization saturates in magnetic fields of 10 T between 65 A m^2 kg^{-1} to 70 A m^2 kg^{-1}.

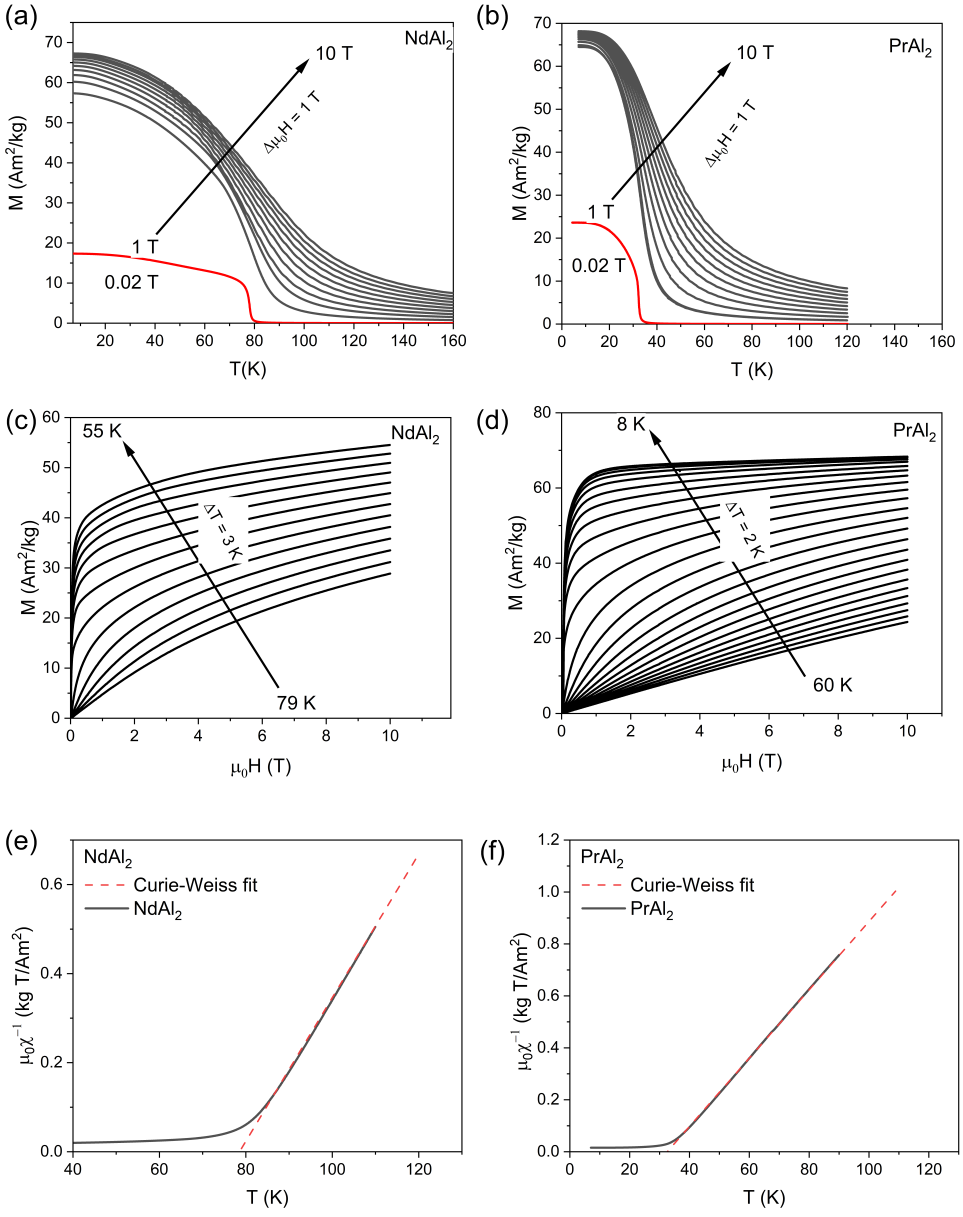

Figure 4.29: (a) (b) Magnetization as a function of temperature for $NdAl_2$ and $PrAl_2$. (c) (d) Magnetization as a function of magnetic fields for $NdAl_2$ and $PrAl_2$. (e) (f) Curie-Weiss fits for $NdAl_2$ and $PrAl_2$.

Figure 4.29 (e) (f) show the Curie-Weiss fits for the samples $NdAl_2$ and $PrAl_2$ in magnetic fields of 1 T. From the Curie-Weiss fits, the paramagnetic Curie temperature of $NdAl_2$ and $PrAl_2$ are given as 78.5 and 32.5 K, respectively, agreeing with the values reported in references [42, 177–179]. The magnetic moments are calculated from the Curie-Weiss fit to be 3.13 and 3.5 μ_B for $NdAl_2$ and $PrAl_2$, respectively. These two values are a bit smaller than the magnetic moments of their corresponding light rare-earth ions shown in **Figure 4.27**.

Figure 4.30 (a) and (b) plot the ΔS_T of $NdAl_2$ and $PrAl_2$ in magnetic fields from 1 to 10 T. The ΔS_T are calculated from the $M(H)$ curves using Maxwell relation via eq. (3.3). In magnetic fields of 2 and 5 T, $NdAl_2$ shows a ΔS_T of about 3.8 and 7.2 J K^{-1} kg^{-1}, respectively. $PrAl_2$ exhibits a large ΔS_T , reaching 9.3 and 16.6 J K^{-1} kg^{-1} in magnetic fields of 2 and 5 T, respectively.

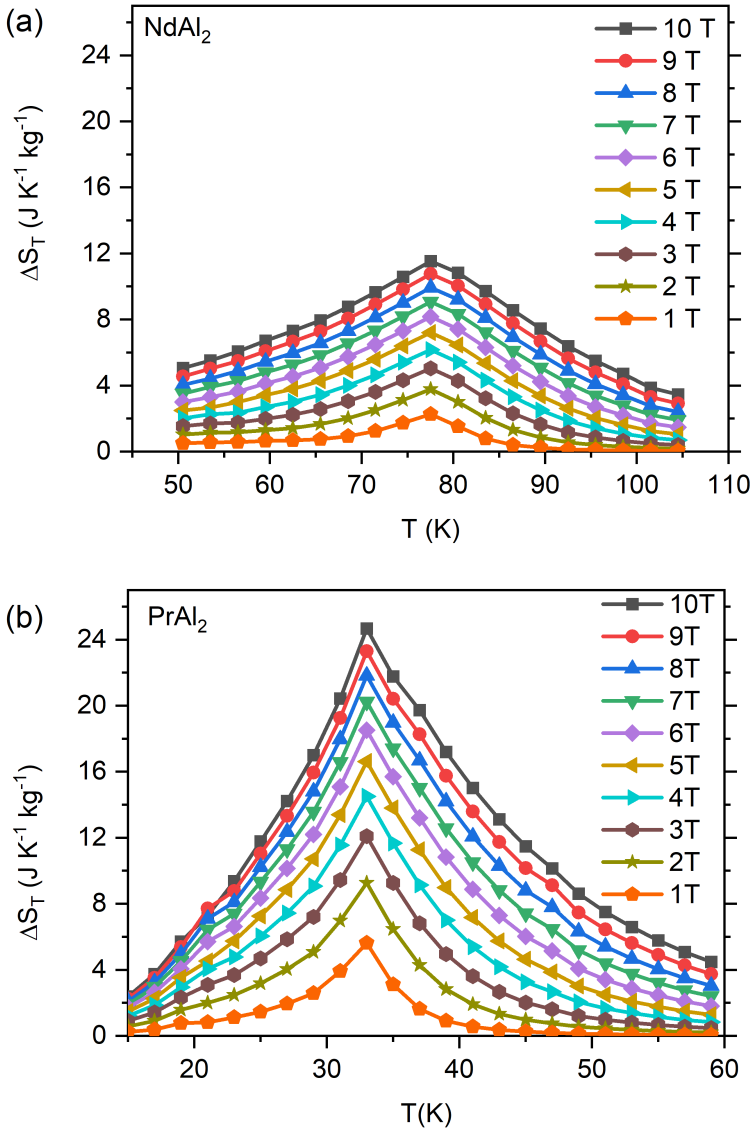

Figure 4.30: ΔS_T in magnetic fields of 1 to 10 T for $NdAl_2$ (a) and $PrAl_2$ (b) from $M(H)$ measurements.

Figure 4.31 (a)(c) present the results of the heat capacity measurements for $NdAl_2$ and $PrAl_2$. λ-shaped peaks are observed for both samples in zero fields, which is a character of second-order phase transition.

Besides, the peak does not shift with magnetic fields. Instead, it only decreases in height with increasing magnetic fields, which is another sign of second-order phase transition [63].

At around room temperature, both samples show a heat capacity of around $72\,\mathrm{J\,mol^{-1}\,K^{-1}}$, which is close to the Dulong-Petit limit ($\approx 74.7\,\mathrm{J\,mol^{-1}\,K^{-1}}$). In addition, the peak on the heat capacity curve in zero fields of $PrAl_2$ is much larger than that of $NdAl_2$. Another point that needs to be emphasized is that the peak on the heat capacity curve for $PrAl_2$ is located at the stage where the heat capacity curves have undergone a fast decrease, while the peak for $NdAl_2$ is located at the stage where the heat capacity curves begin to undergo a fast decrease.

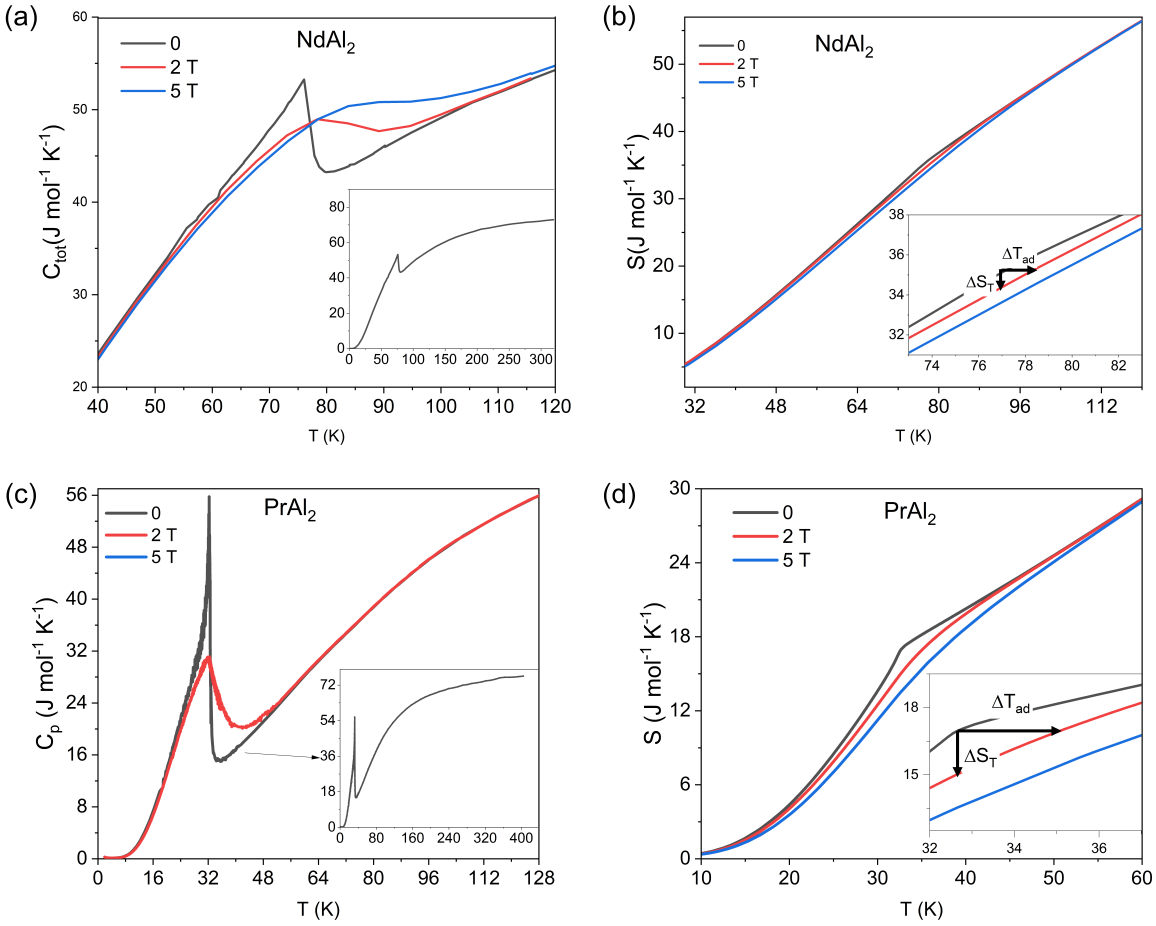

Figure 4.31: Heat capacity measurements and the calculated total entropies of $NdAl_2$ (a)(b) and $PrAl_2$ (c)(d).

Figure 4.31 (b)(d) show the calculated entropies from heat capacity measurements for $NdAl_2$ and $PrAl_2$. The method to obtain ΔS_T and ΔT_{ad} are indicated by the arrows in the insets of the plots. On the total entropy curves of $NdAl_2$, a kink can be observed at around 77 K, which agrees with the paramagnetic Curie temperature from Curie-Weiss fit. For $PrAl_2$, the kink appears at around 30 K, agreeing with the Curie-Weiss fit as well.

Figure 4.32 (a) (b) compares the ΔS_T from $M(H)$ measurements with that from heat capacity mea-

surements. The scattered squares are the ΔS_T calculated from magnetization measurements. The solid lines are the $\Delta S_T(T)$ curves calculated from heat capacity measurements. Both methods match well, as the squares almost fall onto the solid lines. This comparison demonstrates the high quality of the heat capacity measurements.

Figure 4.32 (c) (d) present the results of the adiabatic temperature change ΔT_{ad} calculated by constructing the total entropy curves $S_{tot}(T, H)$. In magnetic fields of 2 T, $NdAl_2$ exhibits a ΔT_{ad} of about 1 K, while $PrAl_2$ shows a value of about 2.5 K. In magnetic fields of 5 T, the ΔT_{ad} of $NdAl_2$ is close to 2.5 K, while for $PrAl_2$, the value is just slightly below 5 K. From the discussion above, it is observed that $PrAl_2$ demonstrates much large ΔS_T and ΔT_{ad} than $NdAl_2$ in magnetic fields of both 2 and 5 T. The fact that $PrAl_2$ shows much larger maximum ΔS_T and ΔT_{ad} than $NdAl_2$ is in agreement with the conclusion made in **Section 4.2.1**: materials with lower T_C tends to show stronger maximum MCE in cryogenic temperature range.

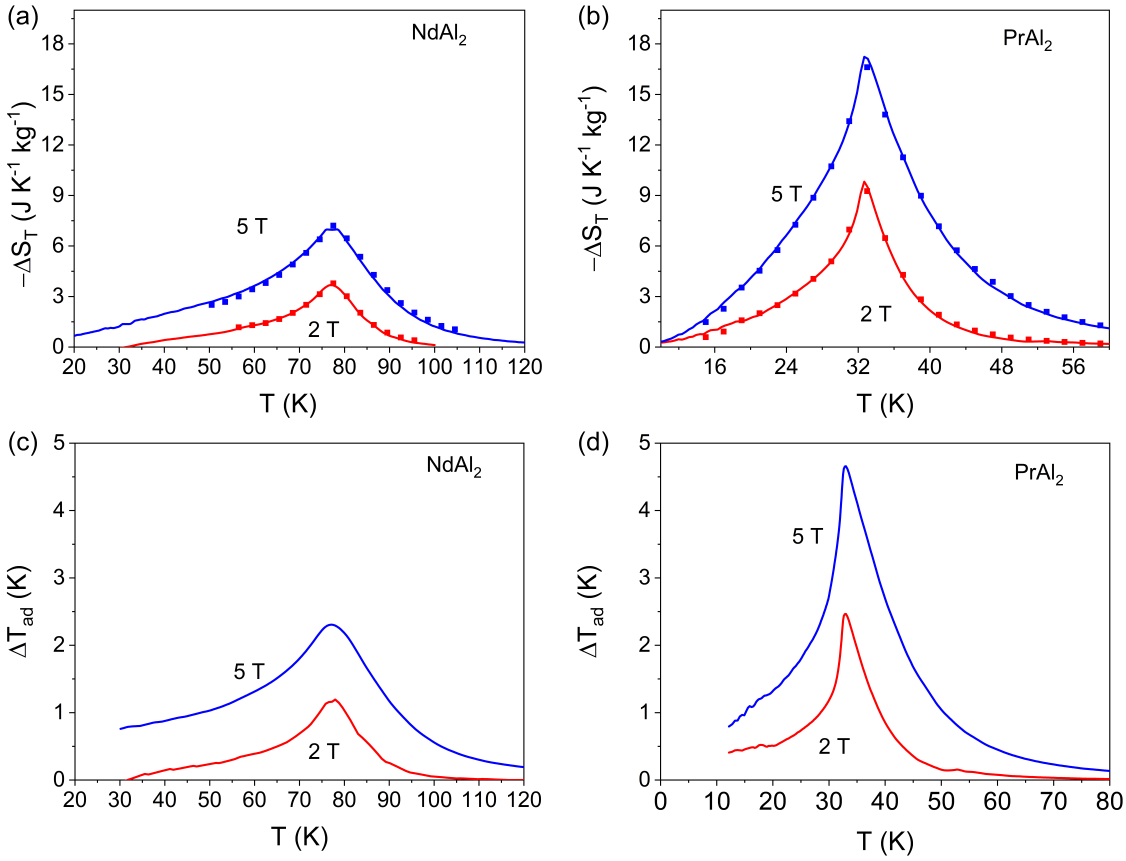

Figure 4.32: (a) (b) Magnetic entropy changes of $NdAl_2$ and $PrAl_2$ from $M(H)$ measurements and heat capacity measurements. (c) (d) Adiabatic temperature changes indirectly calculated from heat capacity measurements.

4.3.3 Tailoring magnetocaloric effect of light rare-earth Laves phases down to 20 K

The above discussion confirmed the moderate MCE in $NdAl_2$ and the large MCE in $PrAl_2$, indicating that these two materials are potential candidates for magnetocaloric hydrogen liquefaction in large-scale utilization. However, magnetocaloric hydrogen liquefaction requires a working temperature range of $77 \sim 20\,\mathrm{K}$ for magnetocaloric materials. From the analysis above, $NdAl_2$ can only cover a narrow temperature range around 77 K, and $PrAl_2$ can only cover a narrow temperature range around 30 K. Their ordering temperatures need to be tailored to cover the full temperature range for hydrogen liquefaction.

Curie temperature of a material is given by:

$$T_C = \frac{2Z\mathcal{J}S(S+1)}{3k_B}, \tag{4.23}$$

where Z is the number of nearest neighbours, $\mathcal{J}$ is the exchange parameter, and S is the spin quantum number.

However, among the rare-earth elements, only Gd possesses S as a good quantum number. Due to the spin-orbital coupling, J is the good quantum number for the rest rare-earth elements. Therefore, spin vector $\vec{S}$ needs to be projected onto the total angular momentum vector $\vec{J}$.

Since

$$\begin{aligned} \vec{L} + 2\vec{S} &= g_J\,\vec{J}\,, \\ \vec{J} &= \vec{L} + \vec{S}, \\ \vec{S} &= (g_J - 1)\vec{J}\,, \end{aligned} \tag{4.24}$$

where $\vec{L}$ is the orbital angular momentum vector. A factor G is introduced as:

$$G = (g_J - 1)\vec{J}^2 = (g_J - 1)J(J+1), \tag{4.25}$$

which is the so-called de Gennes factor. Now, eq. (4.23) becomes

$$T_C = \frac{2Z\mathcal{J}G}{3k_B}. \tag{4.26}$$

It can be deduced that magnetic ordering temperatures for any series of rare-earth metals or compounds with the same conduction-band structure and similar lattice spacing should scale with G. Besides tuning the de Gennes factor G, T_C can also be tuned by tuning $\mathcal{J}$.

Figure 4.33 summarizes three common ways of tuning T_C for rare-earth-based intermetallic compounds: mixing rare-earth elements with different de Gennes factors (**Figure 4.33** (a)), doping the non-rare-earth site (**Figure 4.33** (b)), and hydrogenation ((**Figure 4.33** (c))). While all methods can effectively tune the ordering temperature, the methods of doping the non-rare-earth site and hydrogenation are not as well studied as the method of mixing rare-earth elements [40]. The present work mainly focuses on the method of mixing rare-earth elements.

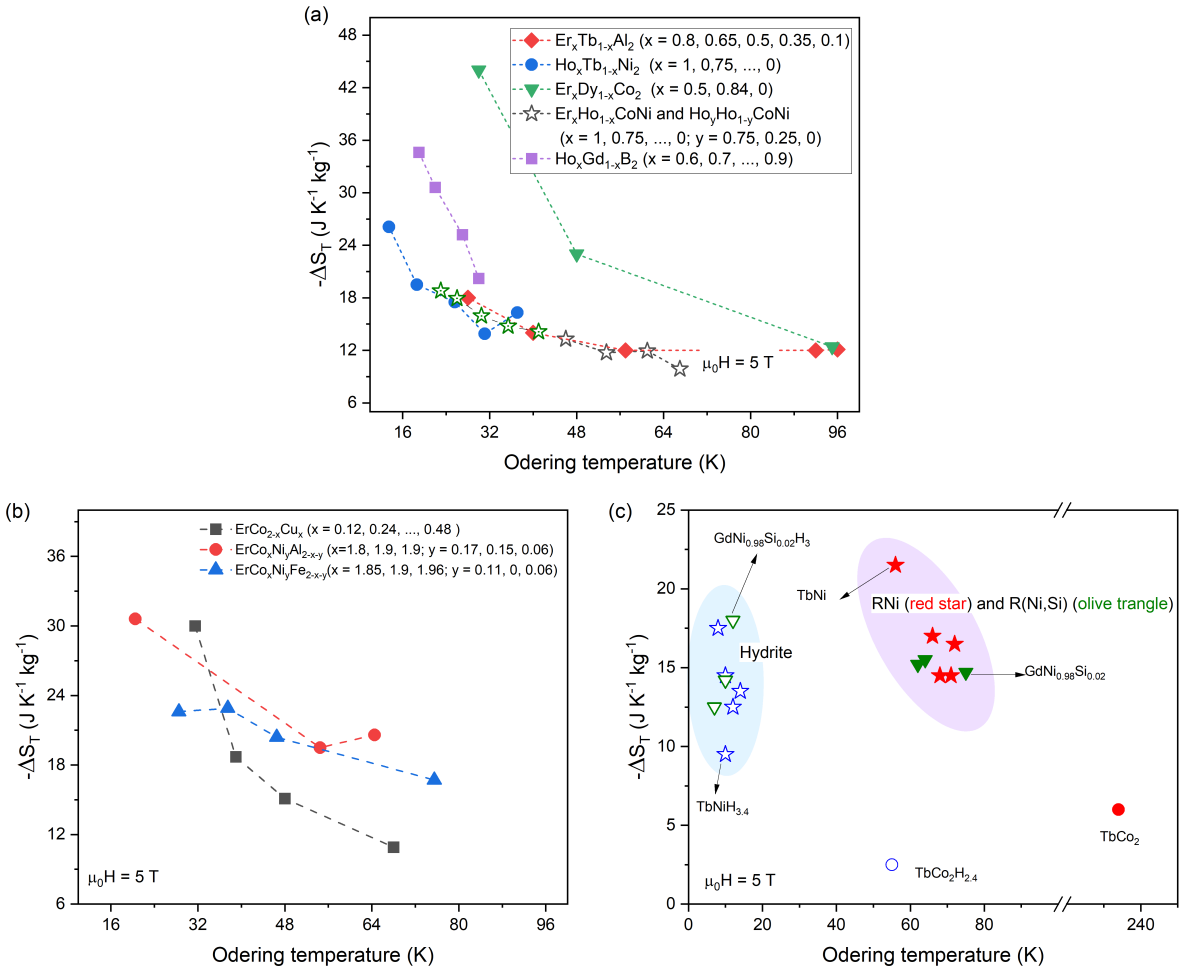

Figure 4.33: (a) (b) (c) ΔS_T with respect to the ordering temperatures in the cases of mixing rare-earth elements, doping the non-rare-earth site, and hydrogenation. Data are taken from [17, 180–191]

In **Section 4.2.1**, it is shown that the maximum ΔS_T and ΔT_{ad} increase with decreasing Curie temperature in cryogenic temperature range. The increasing trend of ΔS_T with decreasing ΔT_{ad} can be observed in **Figure 4.33** (a) and (b). However, upon hydrogenation, ΔS_T tends to decrease, as shown in **Figure 4.33** (c). All the samples shown in **Figure 4.33** belongs to heavy rare-earth-based intermetallic compounds. Here comes a question: how do the magnetocaloric effects of light rare-earth-based intermetallic compounds change with T_C?

To answer this question, a calculation of a mean-field approach based on eq. (2.14) was performed. The parameters of J and g_J are taken to be 4.5 and 11/8 respectively, corresponding to Nd^{3+}. The results are

plotted in **Figure 4.34**, together with the data of heavy rare-earth Laves phases taken from **Figure 4.19**.

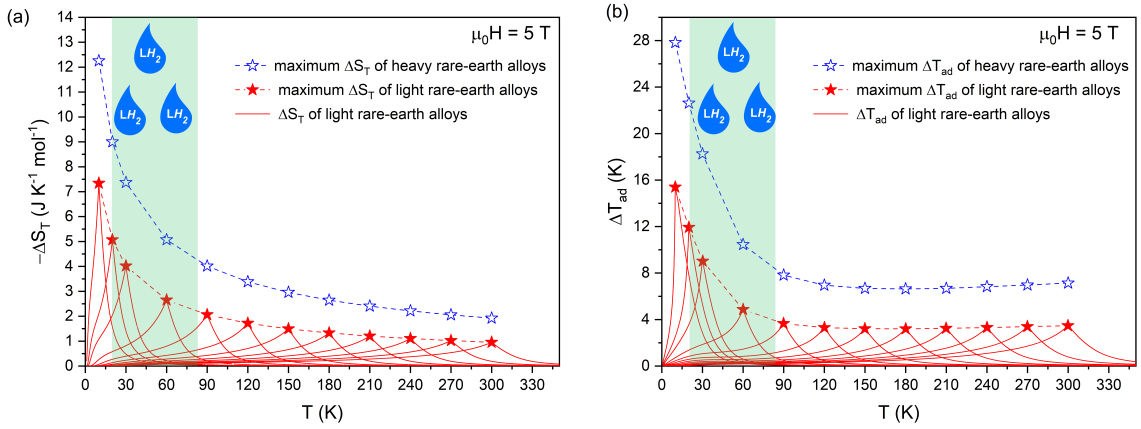

Figure 4.34: (a) Magnetic entropy and (b) adiabatic temperature changes of a light rare-earth alloy series and the maximum magnetic entropy and adiabatic temperature changes of the heavy rare-earth alloy series from mean-field approach.

With decreasing Curie temperature, the maximum ΔS_T and ΔT_{ad} of the light rare-earth series increases as well as the heavy rare-earth series. Although showing a smaller maximum ΔS_T and ΔT_{ad} compared to their heavy rare-earth counterparts with a similar Curie temperature, the light rare-earth series can show large ΔS_T and ΔT_{ad} in cryogenic temperature range, especially in the vicinity of the condensation point of hydrogen. As observed, the alloy in the light rare-earth series with a T_C of 20 K shows values of ΔS_T and ΔT_{ad} that are similar to the alloy in the heavy rare-earth series with a T_C of 60 K. In short, based on the results of the mean-field approach, it can be concluded that light rare-earth magnetocaloric materials can show large magnetocaloric effects in cryogenic temperature range.

As shown in **Figure 4.27**, the de Gennes factor of Nd and Pr are 1.84 and 0.80, respectively. Ce has a low de Gennes factor of 0.18. Here, a method of tuning the Curie temperature for the light rare-earth Laves phases RAl_2 is proposed: mixing Nd and Pr in $(Nd, Pr)Al_2$ to cover the temperature range between T_C of $NdAl_2$ and T_C of $PrAl_2$, i.e. around 77 K to around 30 K, and mixing Pr and Ce in $(Pr, Ce)Al_2$ to tuning T_C down to the condensation point of hydrogen (20 K).

Following this idea, polycrystalline $Nd_xPr_{1-x}Al_2$ (x = 1, 0.75, 0.5, 0.25) and $Pr_xCe_{1-x}Al_2$ (x = 1, 0.75, 0.5) samples were synthesized by arc melting high-purity elements Ce (99.5 at. %), Pr (99.5 at. %), Nd (99.5 at. %), and Al (99.998 at.%) under Ar atmosphere, as introduced in **Section 3.1**. Back-scattered electron (BSE) images were collected with a Tescan Vega 3 scanning electron microscope (SEM). Powder X-ray diffraction (XRD) patterns were collected at room temperature with an x-ray diffractometer (Stadi P, Stoe & Cie GmbH) equipped with a Ge[111]-Monochromator using Mo-K_α-radiation in the Debye-Scherrer geometry. The XRD data were evaluated by Rietveld refinement with the FullProf software packages. A Physical Properties Measurement System (PPMS) from Quantum Design was used to measure the magnetization of the samples in magnetic fields up to 5 T. Heat capacity in magnetic fields of 0, 2, and 5 T was measured in the same PPMS with the 2τ approach.

Figure 4.35 (a) displays the XRD patterns of all the samples. All the samples show a similar patterns, with the peak positions almost overlap with each other, indicating that mixing the rare-earth site with another rare-earth elements does not change the crystal structure. Detailed Rietveld refinements can be found in the published work (reference [40]). The results of the Rietveld refinements show that the samples are of high quality, since the impurities are undetectable under XRD.

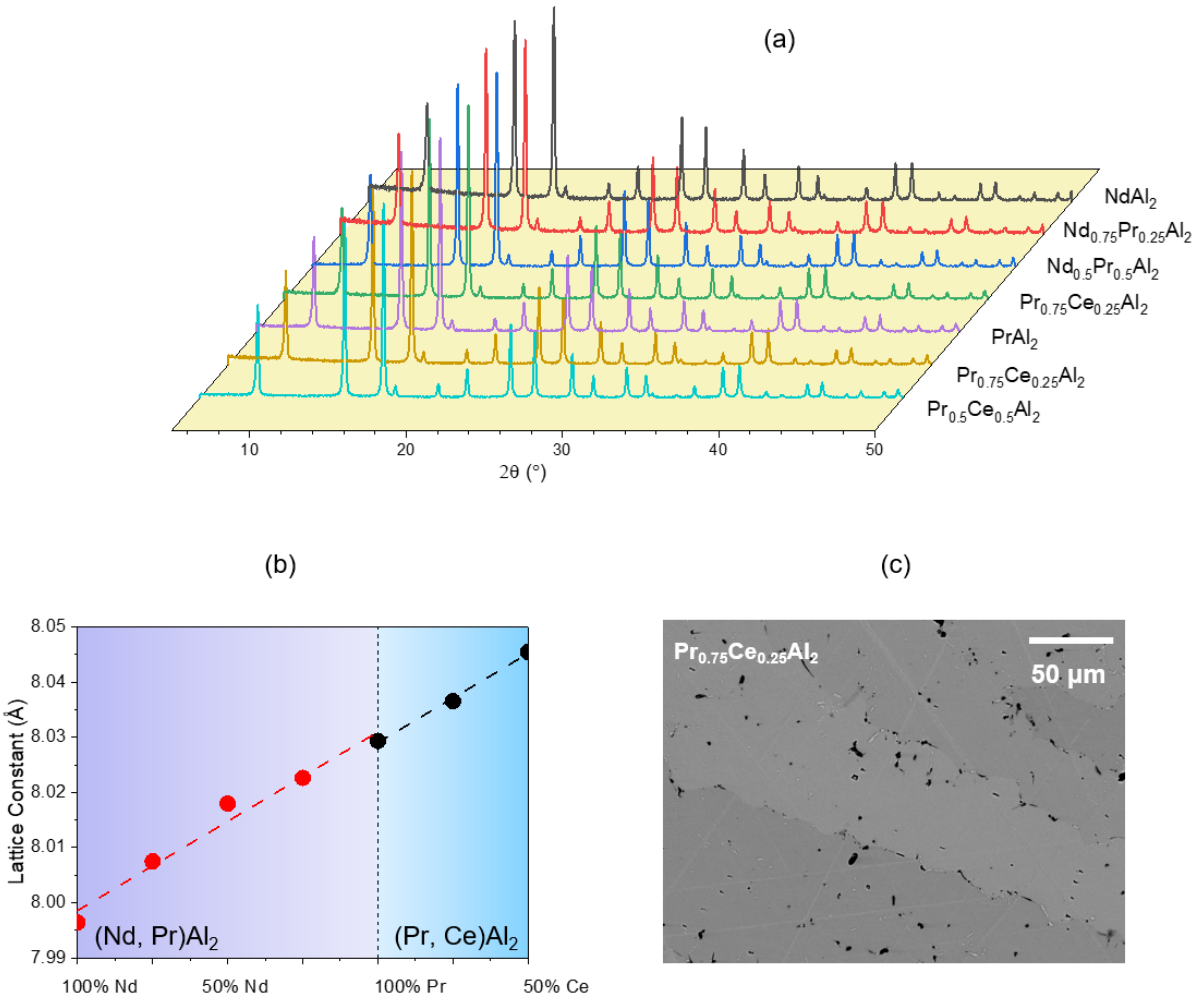

Figure 4.35: (a) XRD patterns of the Laves phases $(R_1, R_2)Al_2$ (R_1: Nd, Pr, R_2: Pr, Ce) measured at room temperature. (b) Lattice constants of all the samples given by Rietveld refinement. The red dashed line is the linear fitting for $(Nd, Pr)Al_2$ samples, and the black dashed line is the linear fitting for $(Pr, Ce)Al_2$ samples. (c) BSE image of $Pr_{0.75}Ce_{0.25}Al_2$. The black dots are holes.

Figure 4.35 (b) plots the lattice constants of $(Nd, Pr)Al_2$ and $(Pr, Ce)Al_2$ samples. A linear correlation can be observed: the lattice constants increase almost linearly from $NdAl_2$ to $PrAl_2$ with increasing Pr content in $(Nd, Pr)Al_2$, and from $PrAl_2$ to $Pr_{0.5}Ce_{0.5}Al_2$ with increasing Ce content in $(Pr, Ce)Al_2$. This linear relation is in consistence with the fact that $NdAl_2$ has the smallest lattice constant and $CeAl_2$ possesses the largest lattice constant within the light rare-earth Laves phase series RAl_2 (R: Ce, Pr, Nd) [192]. **Figure 4.35** (c) shows the BSE image of $Pr_{0.75}Ce_{0.25}Al_2$ as an example. Similar to the BSE images of $NdAl_2$ and $PrAl_2$, no obvious impurities are observed.

Figure 4.36 (a) shows the magnetization as a function of temperature in magnetic fields of 5 T. Except for $Pr_{0.5}Ce_{0.5}Al_2$ which shows a magnetization of 40 A m^2 kg^{-1} at around 10 K, the rest of the samples exhibit a similar magnetization at around 10 K, ranging from 64 A m^2 kg^{-1} to 71 A m^2 kg^{-1}. **Figure 4.36** (b) presents the results of the Curie-Weiss fit using the $M(T)$ measurements in magnetic fields of 1 T. Magnetic moments and Curie temperatures of all the samples are summarized in **Table 4.4**. Both the XRD and BSE measurements confirmed the high quality of all the samples.

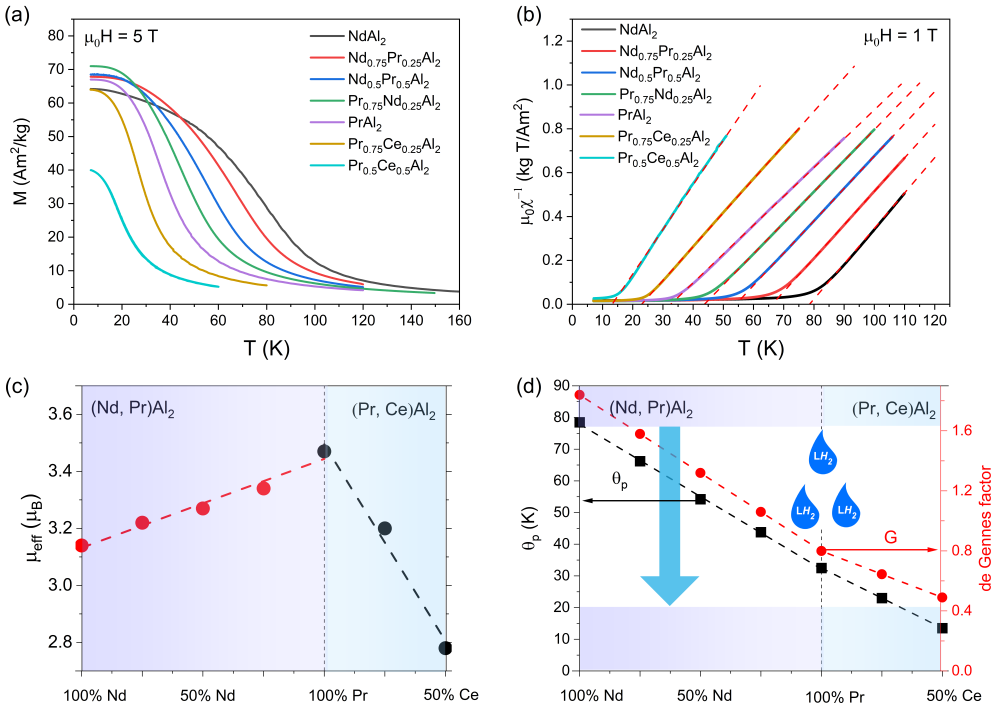

Figure 4.36: (a) Magnetizations of the Laves phases (R1, R2)Al_2 (R1: Nd, Pr, R2: Pr, Ce) as a function of temperature in magnetic fields of 5 T. (b) Curie-Weiss fits of the Laves phases (R1, R2)Al_2 (R1: Nd, Pr, R2: Pr, Ce) in magnetic fields of 1 T. (c) Effective magnetic moments of the samples using the Curie-Weiss law. (d) Paramagnetic T_C of the samples determined by the Curie-Weiss law (black squares) and the average de Gennes factor (red circles).

Figure 4.36 (c) plots the effective magnetic moments obtained from the Curie-Weiss fits for all the samples. In the (Nd, Pr)Al_2 samples, the magnetic moment increases almost linearly from 3.14 μ_B for $NdAl_2$ to 3.47 μ_B for $PrAl_2$, while the magnetic moments of the (Pr, Ce)Al_2 samples decrease with the increasing Ce content down to 2.78 μ_B for $Pr_{0.5}Ce_{0.5}Al_2$. These observations are consistent with the fact that Pr^{3+} possesses the largest magnetic moment of 3.58 μ_B among Ce^{3+}, Pr^{3+}, and Nd^{3+}, while Ce^{3+} exhibits the smallest magnetic moment of 2.54 μ_B.

Figure 4.36 (d) presents the paramagnetic Curie temperature from Curie-Weiss fits and the de Gennes factor of all the samples. Successfully, a light rare-earth Laves phase series is developed, covering the full temperature range of 77 $\sim$ 20 K required by magnetocaloric hydrogen liquefaction. Besides, T_C decreases almost linearly from the $NdAl_2$ sample to the $Pr_{0.5}Nd_{0.5}Al_2$ sample, which is consistent with the linearly decreasing de Gennes factor.

Table 4.4: Effective magnetic moments and paramagnetic Curie temperatures of the RAl_2 and RNi_2 Laves phases calculated using the Curie-Weiss law.

Compounds	$T_C(K)$	$\mu_{eff}(\mu_B/f.u.)$
$NdAl_2$	78.5	3.14
$Nd_{0.75}Pr_{0.25}Al_2$	66.3	3.22
$Nd_{0.5}Pr_{0.5}Al_2$	54.2	3.27
$Pr_{0.75}Nd_{0.25}Al_2$	43.6	3.34
$PrAl_2$	32.6	3.47
$Pr_{0.75}Ce_{0.25}Al_2$	23	3.2
$Pr_{0.5}Ce_{0.5}Al_2$	13.2	2.78

In conclusion, a fully light rare-earth-based magnetocaloric material covering the temperature range required for magnetocaloric hydrogen liquefaction (77 $\sim$ 20 K) is developed by tuning de Gennes factors via mixing different rare-earth elements, and the large effective magnetic moments μ_{eff} are retained from $NdAl_2$ sample to $Pr_{0.75}Ce_{0.25}Al_2$ sample.

Based on the theoretical calculations presented in **Figure 4.34** (a), it can be inferred that in the light rare-earth $(R_1, R_2)Al_2$ (R_1: Nd, Pr; R_2: Pr, Ce) series, the maximum ΔS_T are expected to increase with decreasing T_C , and near the condensation point of hydrogen, the maximum ΔS_T should exhibit large values. **Figure 4.37** (a) $\sim$ (g) shows the ΔS_T of all the samples in magnetic fields of 2 and 5 T obtained from $M(H)$ measurements (scattered points) and heat capacity measurements (solid lines). ΔS_T from magnetization match well with ΔS_T from heat capacity, as the scattered points almost fall onto the lines.

Agreeing with the conclusion made from **Figure 4.34** (a), the maximum ΔS_T increases with decreasing T_C . In 5 T, ΔS_T increases from $7.21\,\mathrm{J\,K^{-1}\,kg^{-1}}$ for $NdAl_2$ up to $18.53\,\mathrm{J\,K^{-1}\,kg^{-1}}$ for $Pr_{0.75}Ce_{0.25}Al_2$. However, $Pr_{0.5}Ce_{0.5}Al_2$ shows a smaller ΔS_T than $Pr_{0.75}Ce_{0.25}Al_2$, though its T_C is lower than $Pr_{0.75}Ce_{0.25}Al_2$. Teh reason for this could be the smaller magnetic moments and the influence of crystal field at low temperatures.

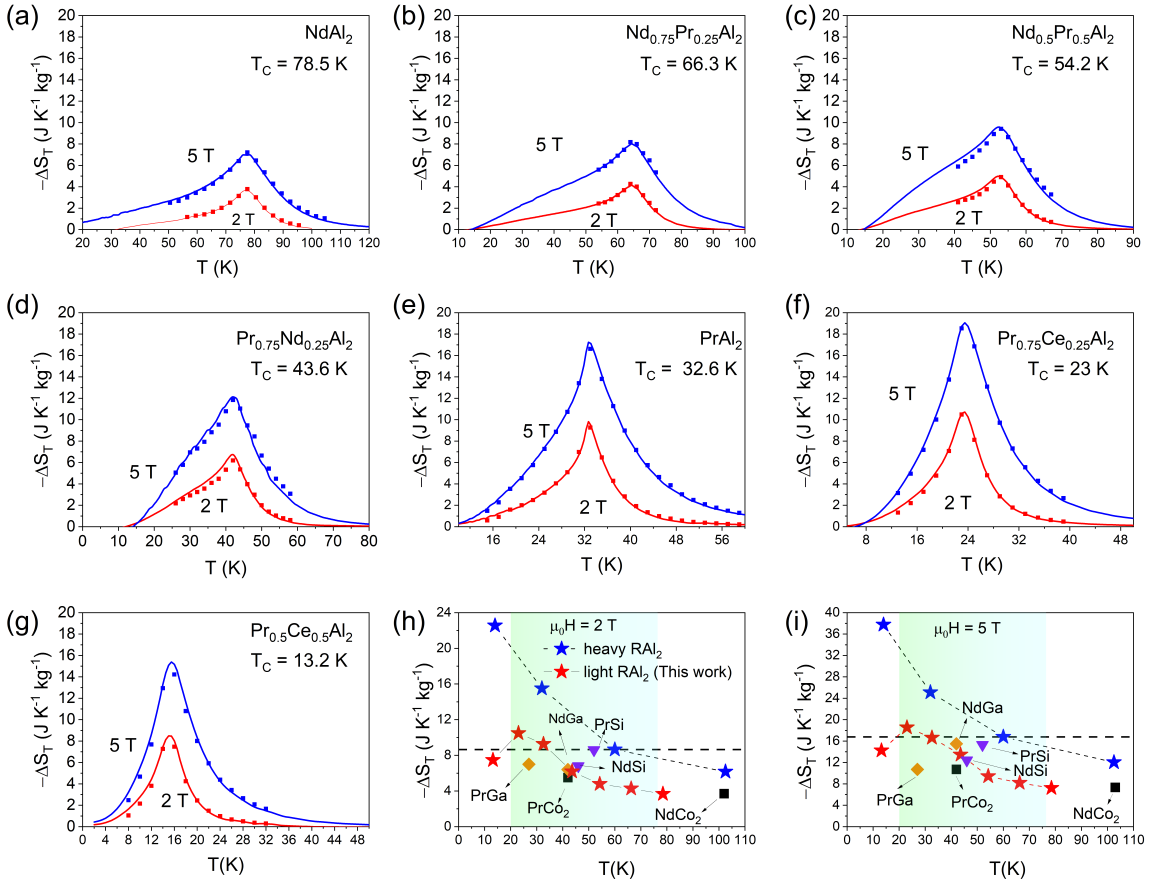

Figure 4.37: 5 (a) $\sim$ (g) ΔS_T of $(Nd, Pr)Al_2$ and $(Pr, Ce)Al_2$ in magnetic fields of 2 and 5 T from $M(H)$ measurements (scattered points) and heat capacity measurements (solid lines). (h) $\sim$ (i) Comparisons of the maximum ΔS_T of the light rare-earth series in this work, RCo_2 ([193, 194]), RSi ([195, 196]), and RGa ([197, 198]), and the heavy rare-earth based RAl_2 ([12, 199]) and $Tb_xHo_{1-x}Ni_2$ (x = 0.75, 0.5, 0.25, 0) [181].

Figure 4.37 (h) and (i) compare the maximum ΔS_T of the samples in the present work with some of the other light and heavy rare-earth magnetocaloric materials. The light rare-earth-based $(R_1, R_2)Al_2$ (R_1:

Nd, Pr; R_2: Pr, Ce) series demonstrate a competitive maximum ΔS_T , which is comparative to or larger than the rest light rare-earth-based magnetocaloric materials with a similar T_C in **Figure 4.37** (h) and (i). PrSi is an exception for showing a larger ΔS_T than $Pr_{0.75}Nd_{0.25}Al_2$ and $Pr_{0.5}Nd_{0.5}Al_2$. Despite that the heavy rare-earth series RAl_2 (R: Tb, Dy, Ho, Er) shows an obvious larger maximum ΔS_T than their light rare-earth counterparts with a similar T_C , the light rare-earth (Pr, Ce)Al_2 exhibits a comparative ΔS_T to $DyAl_2$, which is known for the strong MCE in the temperature range of $77 \sim 20$ K.

Similar to ΔS_T , based on the theoretical calculations presented in **Figure 4.34** (b), it can be inferred that in the light rare-earth $(R_1, R_2)Al_2$ (R_1: Nd, Pr; R_2: Pr, Ce) series, the maximum ΔT_{ad} are expected to increase with decreasing T_C , and near the condensation point of hydrogen, the maximum ΔT_{ad} should exhibit large values. **Figure 4.38** (a) $\sim$ (g) shows the ΔT_{ad} of all the samples in magnetic fields of 2 and 5 T indirectly obtained from heat capacity measurements. Agreeing with the inference, in either 2 or 5 T, the maximum ΔT_{ad} increases with decreasing T_C . ΔT_{ad} increases from about 2 K for $NdAl_2$ up to about 5 K for $Pr_{0.75}Ce_{0.25}Al_2$ in 5 T. Again, $Pr_{0.5}Ce_{0.5}Al_2$ shows a smaller ΔT_{ad} than $Pr_{0.75}Ce_{0.25}Al_2$.

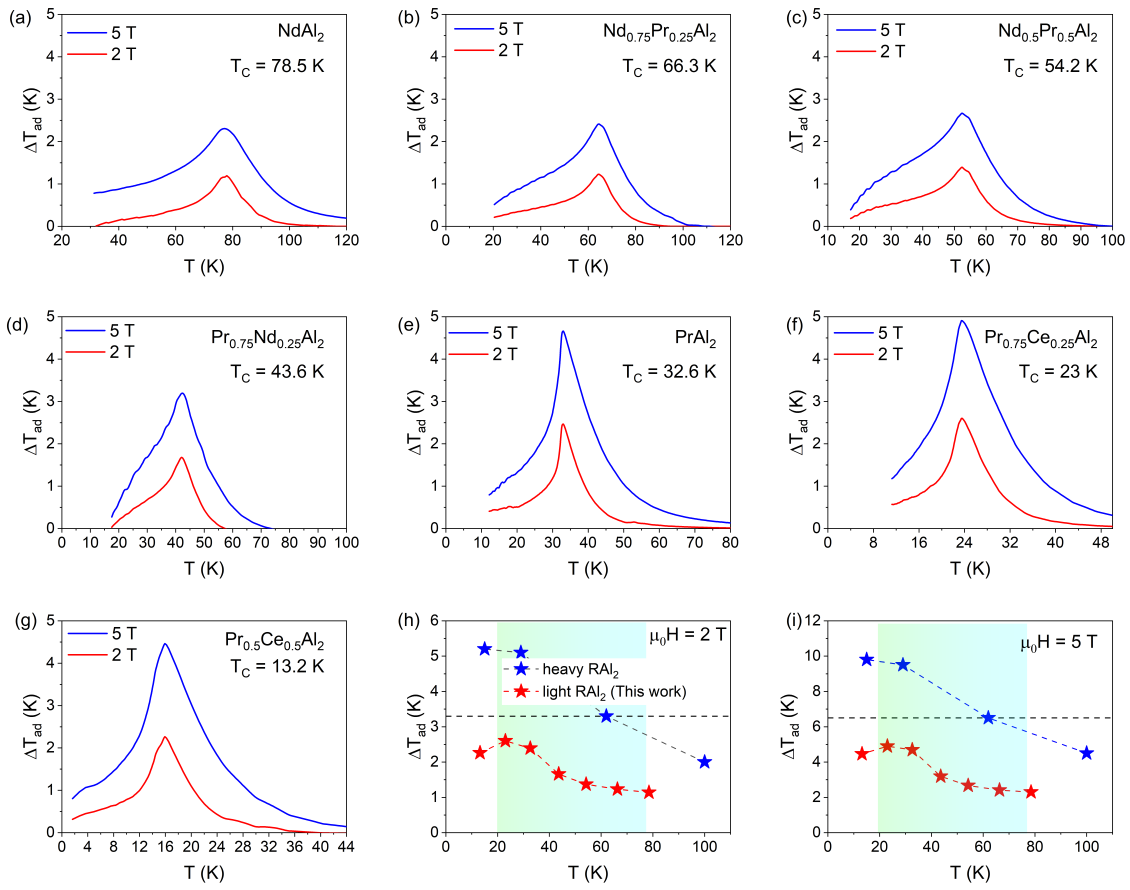

Figure 4.38: (a) $\sim$ (g) ΔT_{ad} of $(R_1, R_2)Al_2$ (R_1: Nd, Pr, R_2: Pr, Ce) obtained from heat capacity measurements in magnetic fields of 2 and 5 T. (h)$\sim$(i) Comparisons of the ΔT_{ad} of the light- and heavy rare-earth RAl_2 series (data of heavy rare-earth RAl_2 (R = Tb, Dy, Ho, and Er) are taken from reference [12]).

Figure 4.38 (h) and (i) compares the maximum ΔT_{ad} of the samples in the present work with the heavy rare-earth RAl_2 (R: Gd, Tb, Dy, Ho, and Er) series. The light rare-earth-based $(R_1, R_2)Al_2$ (R_1: Nd, Pr; R_2: Pr, Ce) series demonstrate a competitive maximum ΔT_{ad} near 20 K (the condensation point of hydrogen), reaching values close to 5 K in magnetic fields of 5 T. Despite that the heavy rare-earth series RAl_2 (R: Tb, Dy, Ho, Er) shows an obvious larger maximum ΔT_{ad} than their light rare-earth counterparts with a similar T_C , the light rare-earth $(Pr, Ce)Al_2$ exhibits a ΔT_{ad} that is only slightly lower than $DyAl_2$.

In this part, the light rare-earth-based magnetocaloric materials are studied. The relatively high abundance of light rare-earth elements in the earth's crust makes their alloys appealing for magnetocaloric hydrogen liquefaction on a large scale. In this part, based on the theoretical calculations on the light rare-earth Laves phases RAl_2, a design strategy for developing a light rare-earth Laves phase series covering the temperature range of $77 \sim 20$ K is used: tune the T_C by mixing the light rare-earth elements with different de Gennes factors.

Successfully, a light rare-earth Laves phase series $(R_1, R_2)Al_2$ (R1: Nd, Pr, R2: Pr, Ce) with T_C in the range from 77 to 20 K is made, which demonstrates large maximum ΔS_T and ΔT_{ad} especially near 20 K, the condensation point of hydrogen. It is observed that the (Pr, Ce) $)Al_2$ samples show comparable ΔS_T to $DyAl_2$, a heavy rare-earth-based magnetocaloric material often proposed as an candidate for hydrogen liquefaction. The $(Pr, Ce)Al_2$ samples also show a large ΔT_{ad} that is only slightly smaller than $DyAl_2$.

This method for tailoring the MCEs of the light rare-earth Laves phases may be applied to other magnetocaloric material systems to adjust their MCEs for the liquefaction of industrial gases, inclusive but not limited to hydrogen gas.

4.4 First-order MCE in light rare-earth-based R_2In for hydrogen liquefaction

4.4.1 Unusually large magnetic entropy changes of Pr_2In

From the discussion in **Section 4.3**, it is observed that light rare-earth-based second-order magnetocaloric materials can show large maximum ΔS_T near the condensation point of hydrogen (20 K). However, near the nitrogen condensation point (77 K), the maximum ΔS_T are not as excellent as near 20 K. As shown in **Figure 4.39**, the mean-field approach gives a ΔS_T of about $5\,\mathrm{J\,K^{-1}\,kg^{-1}}$ at 20 K for light rare-earth alloy series. However, the value drops to below $3\,\mathrm{J\,K^{-1}\,kg^{-1}}$ at 60 K. The inset in **Figure 4.39** shows the experimental data of certain light rare-earth-based magnetocaloric materials, including the light rare-earth-based $(R_1, R_2)Al_2$ (R_1: Nd, Pr, R_2: Pr, Ce) presented in **Section 4.3**. It can be observed that light rare-earth magnetocaloric materials can achieve a ΔS_T above $8\,\mathrm{J\,K^{-1}\,kg^{-1}}$ near 20 K, whereas near 77 K or above, ΔS_T of the light rare-earth-based magnetocaloric materials decrease to below $5\,\mathrm{J\,K^{-1}\,kg^{-1}}$.

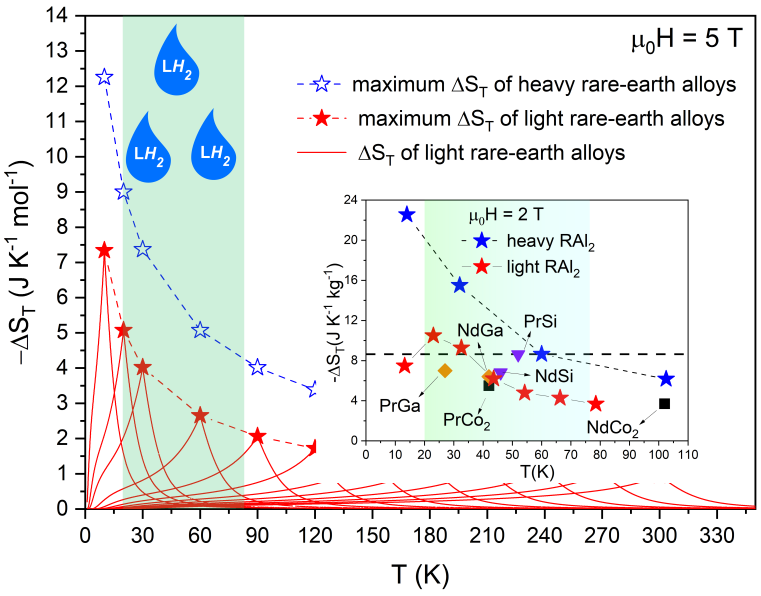

Figure 4.39: ΔS_T for light and heavy rare-earth series obtained from the mean-field approach and experimental data of certain light and heavy rare-earth based magnetocaloric materials. This picture is a combination of **Figure 4.34** (a) and **Figure 4.37** (i).

In addition to the performance gap between MCEs near 77 K and near 20 K, there is another performance gap: light rare-earth-based magnetocaloric materials generally show smaller ΔS_T than their heavy rare-earth counterparts with a similar T_C . From **Figure 4.39**, it is observable that the line of the ΔS_T of the heavy rare-earth series is above the line of the ΔS_T of the light rare-earth series, in both of the data from the mean-field approach and from the experiments. Here, two "stereotypes" are summarized: (1) rare-earth-based magnetocaloric intermetallic compounds show larger maximum ΔS_T near 20 K than near 77 K; (2) light rare-earth-based magnetocaloric intermetallic compounds show smaller maximum ΔS_T than their heavy rare-earth counterparts with a similar T_C .

However, the giant ΔS_T in Pr_2In at about 56 K breaks these two "stereotypes". **Figure 4.40** compares the ΔS_T of light and heavy rare-earth-based R_2In, RAl_2, and RCo_2 (R: Pr, Nd, Eu, Tb, Dy, Ho, and Er) in magnetic fields of 5 T. Although belonging to the light rare-earth-based alloys, the ΔS_T of Pr_2In is much larger than $DyAl_2$. Unlike the RAl_2 system in which the ΔS_T of the heavy rare-earth-based compound is larger than that of the light rare-earth compound when the two have similar ordering temperatures, Pr_2In shows a ΔS_T that even surpasses Er_2In, the compound that exhibits the largest ΔS_T among the heavy rare-earth R_2In system.

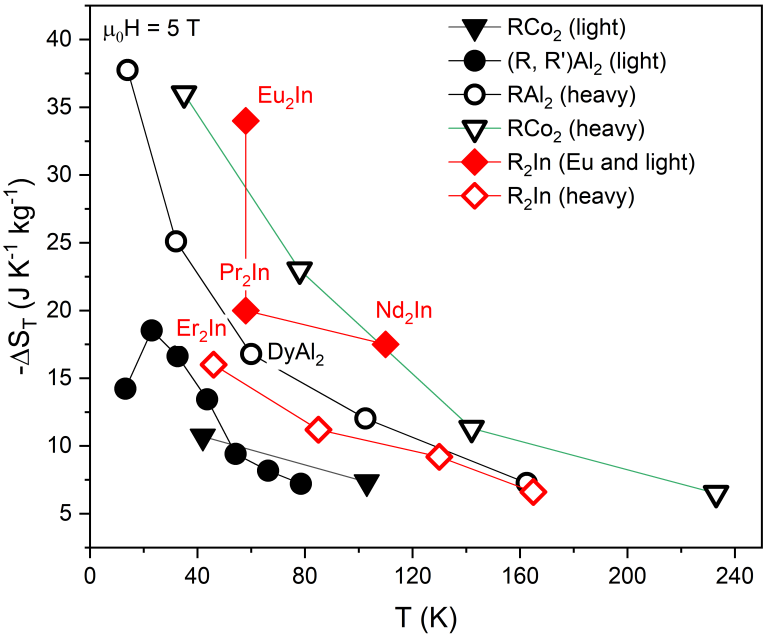

Figure 4.40: ΔS_T of light and heavy rare-earth-based R_2In, RAl_2 (Pr, Nd, Eu, Tb, Dy, Ho, Er), and RCo_2 in magnetic fields of 5 T. Data are taken from [12, 40, 199–201].

The eye-catching giant ΔS_T in Pr_2In is ascribed to its peculiar first-order magnetic phase transition. In 2005, Forker *et al.* reported that Pr_2In demonstrates a first-order phase transition, supported by the measurements of the magnetic and electric hyperfine interactions [202]. As a matter of fact, the heavy rare-earth-based R_2In (R:Gd, Tb, Dy, Ho, and Er) alloys have been intensively investigated for their MCEs. These compounds show a second-order phase transition at T_C . Eu_2In is the first compound in the R_2In series that was reported to show a giant MCE at about 56 K due to its first-order phase transition by Guillou *et al.* [200]. As shown in **Figure 4.40**, Eu_2In exhibits a ΔS_T of about 35 J K^{-1} kg^{-1} in magnetic fields of 5 T. This value is much larger than that of the ΔS_T of $HoCo_2$, and close to the value of the ΔS_T of $ErCo_2$, which is known to show a giant first-order magnetocaloric effect [12].

Triggered by the discovery of the giant MCE in Eu_2In, many experimental and theoretical investigations have been conducted. Among them, it should be mentioned that Tapia-Mendive *et al.* demonstrated that the first-order phase transition in Eu_2In is because of a purely electronic mechanism - the positive feedback between the magnetism of itinerant valence electrons and the ferromagnetic ordering of local f-electron moments drives the first-order phase transition of Eu_2In [203]. Soon after the discovery of the giant MCE in Eu_2In, the giant ΔS_T in Pr_2In was reported by Biswas *et al.* [43, 204].

Another eye-catching point on the Pr_2In and Eu_2In alloys is that, in spite of belonging to the first-order magnetocaloric materials, these two materials shows a negligible thermal hysteresis, indicating a nearly full reversibility of their MCE [43, 200]. Unlike some typical first-order magnetocaloric materials such as Heusler alloys Ni-Mn-In and La-Fe-Si which show a large volume change during their first-order phase transitions [44], these two materials show small volume changes. Nevertheless, the different nature of phase transitions in Eu_2In and Pr_2In compared with the heavy rare-earth-based R_2In materials has yet to be further studied.

4.4.2 Discovering large magnetocaloric effect in Nd_2In

Due to the chemical and physical similarities of Pr and Nd, magnetocaloric materials based on these two elements often appear as a couple. For instance, as shown in **Figure 4.39**, $NdCo_2$ is coupled with $PrCo_2$, while $NdAl_2$ is coupled with $PrAl_2$. Based on this observation, it can be inferred that Nd_2In might also exhibit a large MCE like its couple Pr_2In.

The Nd_2In sample was prepared by arc melting as introduced in **Section 3.1**. The magnetization measurements were carried out in magnetic fields up to 12 T in the Physical Properties Measurement System (PPMS). After synthesizing Nd_2In, it was discovered that the surface decomposes quickly in air or moisture. Therefore, the ground powders of the Nd_2In sample were sealed hermetically in a capillary in an Ar-filled glovebox ($P(O_2 < 0.1$ ppm, MBraun)). The XRD data were evaluated by Rietveld refinement with the software FullProof. BSE imaging was obtained with a Tescan Vega 3 scanning electron microscope (SEM). To avoid decomposition of the sample surface, after the final polishing, the specimen for BSE imaging was transfer to the device quickly. The XRD analysis and the BSE image are shown in **Figure 4.41**.

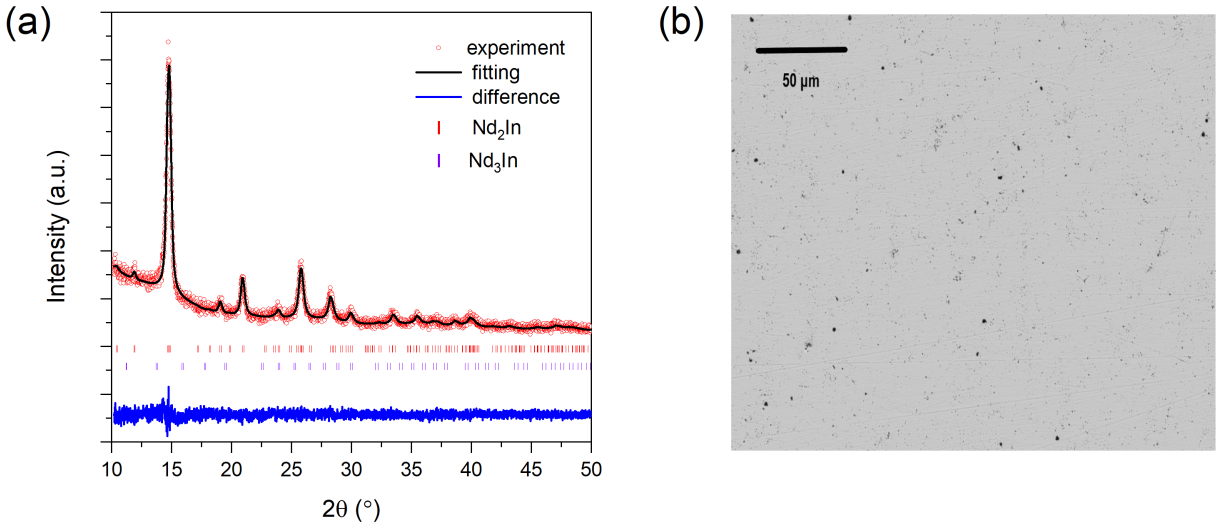

Figure 4.41: XRD and BSE image of Nd_2In.

The XRD analysis shows that the Nd_2In sample crystallizing in the Ni_2In-type hexagonal structure (space group: $P6_3/mmc$). A small amount of impurity of Nd_3In crystallizing in the Cu_3In-type cubic structure with a phase fraction of about 5% is confirmed by the XRD analysis. In the BSE image of Nd_2In, no obvious secondary phase is observable. Both the XRD and the BSE measurements demonstrate the high quality of the Nd_2In sample.

Figure 4.42 (a) presents the $M(T)$ curves in fields of 0.05, 1, and 2 T. From the $M(T)$ curve in magnetic fields of 0.05 T indicates that the ordering temperature of Nd_2In is around 108 K. The heating and cooling $M(T)$ curves in both magnetic fields of 1 and 2 T almost overlap with each other, demonstrating that the thermal hysteresis is negligible. **Figure 4.42** (b) plots the ΔS_T in magnetic fields from 0.25 up to 2 T with a magnetic field step of 0.25 T. The ΔS_T is obtained using the Maxwell relation from the $M(T)$ measurement with a magnetic field step of 0.25 T via **Equation (2.29)**. The ΔS_T reaches 7.42 J K^{-1} kg^{-1} at about 109 K in magnetic fields of 2 T. **Figure 4.42** (c) compares the ΔS_T of Nd_2In with certain intensively studied rare-earth-based magnetocaloric materials. At around the condensation point of natural gas, Nd_2In shower a lower ΔS_T than the first-order magnetocaloric material $Dy_{0.7}Er_{0.3}Co_2$, which has a ΔS_T of about 11.9 J K^{-1} kg^{-1}. Despite that Nd_2In belongs to light rare-earth-based compounds, its ΔS_T compares with $TbAl_2$ showing a ΔS_T of about 7.4 J K^{-1} kg^{-1}.

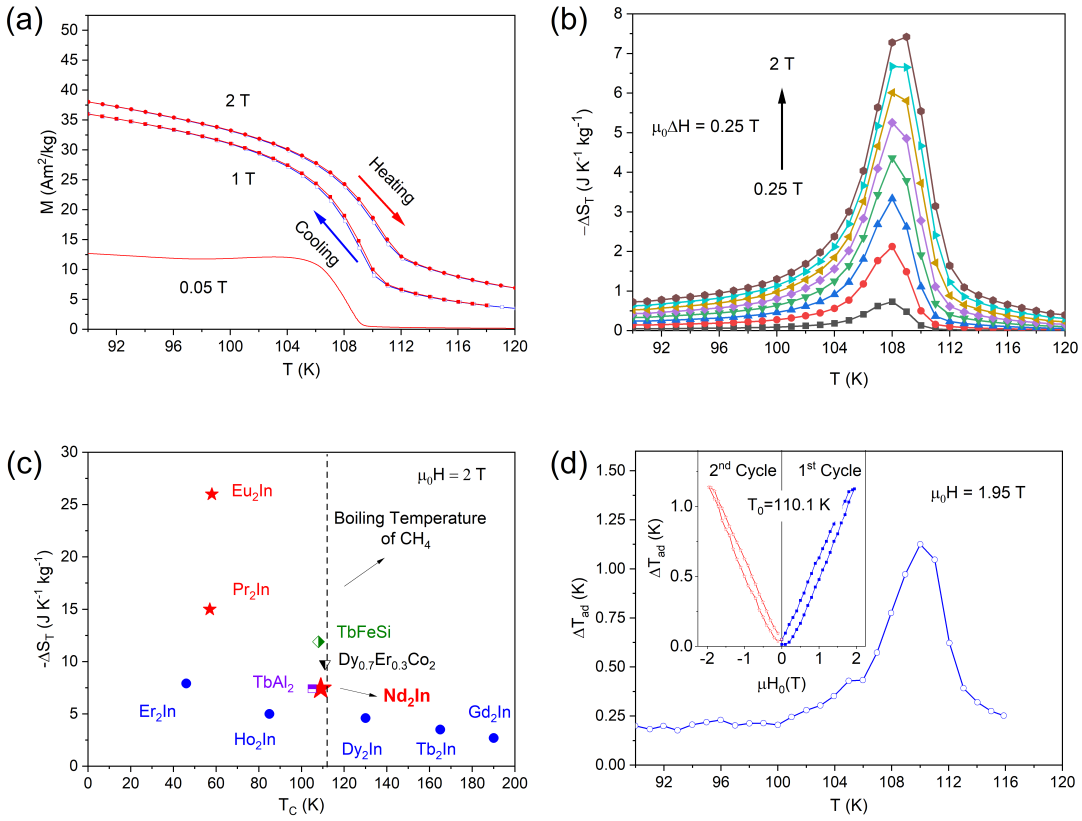

Figure 4.42: (a) Magnetization as a function of temperature in 1 and 2 T. (b) ΔS_T as a function of temperature in 0.25, 0.5, …, 2 T. (c) comparing ΔS_T of Nd_2In with certain rare-earth-based magnetocaloric materials. Data are taken from references [43, 115, 123, 126, 200, 205–207]. (d) ΔT_{ad} as a function of temperature under a magnetic field change of 1.95 T using continuous measurement protocol; the inset shows the one as a function of magnetic field up to 1.95 T at 110.1 K during cycling.

Similar to Pr_2In, the ΔS_T of Nd_2In is larger than $ErAl_2$ as well, breaking the "stereotype" that heavy rare-earth-based magnetocaloric materials generally show a larger ΔS_T than their light rare-earth-based counterparts with a similar or higher T_C . **Figure 4.42** (d) shows the adiabatic temperature change obtained in magnetic fields of 1.95 T using continuous protocol. ΔT_{ad} peaks at about 110 K, reaching a value of 1.13 K.

In the inset of **Figure 4.44** (d), ΔT_{ad} at 110.1 K as a function of magnetic fields of up to 1.95 T during the first and second cycles are plotted. In line with the observation of negligible thermal hysteresis, ΔT_{ad} in both cycles reach a nearly identical value of about 1.13 K, confirming the nearly full reversibility of the MCE.

The unusually large ΔS_T of Nd_2In suggests that this compound undergoes a first-order phase transition at about 108 K, in agreement with the measurements of the magnetic and electric hyperfine interactions conducted by Forker *et al.*. In order to confirm that the phase transition order is indeed first for the Nd_2In sample in the present work, a quantitative criterion featuring the exponent n from the field dependence of ΔS_T was performed to determine the order of the phase transition at about 108 K [69]. Details on this criterion can be found in **Section 2.4.4**. The results are plotted in **Figure 4.43** (a). The exponent n overshoots 2 in magnetic fields of 0.5, 1, ..., 2 T, proving that the phase transition of Nd_2In at about 108 K is indeed of first-order.

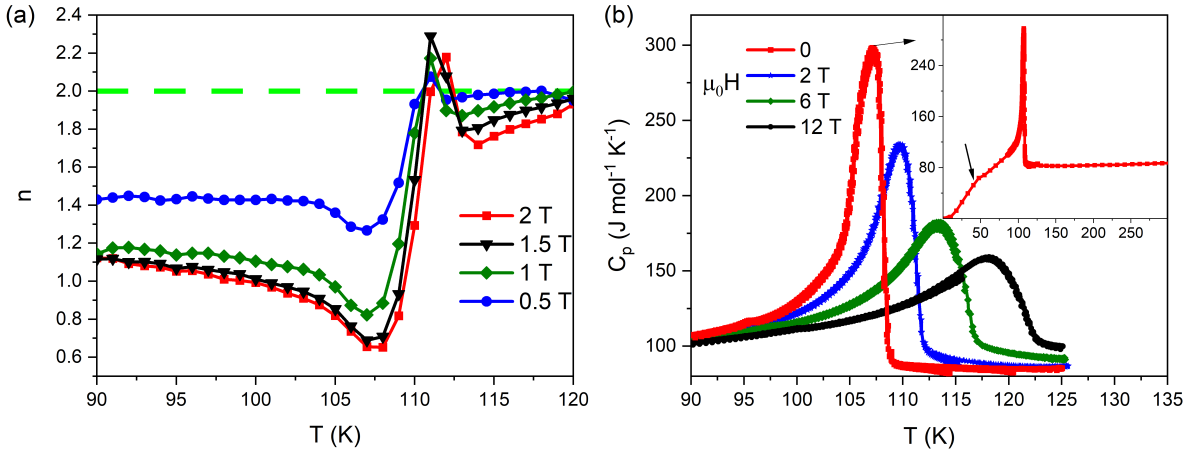

Figure 4.43: (a) n value as a function of temperature in fields of 0.5, 1, 1.5, and 2 T. (b) Heat capacity of Nd_2In sample in fields of 0, 2, 6, and 12 T; the inset shows the heat capacity in zero magnetic field down to 2 K.

In addition, the capacity of Nd_2In was also measured in magnetic fields of 0, 2, 6, and 12 T, as plotted in **Figure 4.43** (b). Apparently, the peak on the heat capacity curve shifts with the changing magnetic field. The speed of the shifting is about 1 K T^{-1}. This behavior is a character of first-order phase transition [63]. Both the quantitative criterion and the heat capacity measurements confirm the first-order phase transition in Nd_2In at about 108 K. It can be concluded that the unusually large ΔS_T of Nd_2In is attributed to its first-order phase transition at about 108 K.

Since first-order phase transition is usually coupled with structure transition, a simultaneous measurement on magnetization, resistivity, and strain was conducted using a home-built device, as introduced in **Chapter 3**. **Figure 4.44** (a) shows the magnetization as a function of temperature down to 2 K and in magnetic fields of up to 12 T. Besides the magnetic transition at about 108 K, another magnetic transition at around 50 K is observed. Similar transitions were reported in Pr_2In and Ho_2In to be a possible spin-reorientation transition. **Figure 4.44** (b) shows the resistivity of the Nd_2In sample [204, 208]. The kinks are observed at around 108 K, corresponding to the magnetic phase transition at about 108 K.

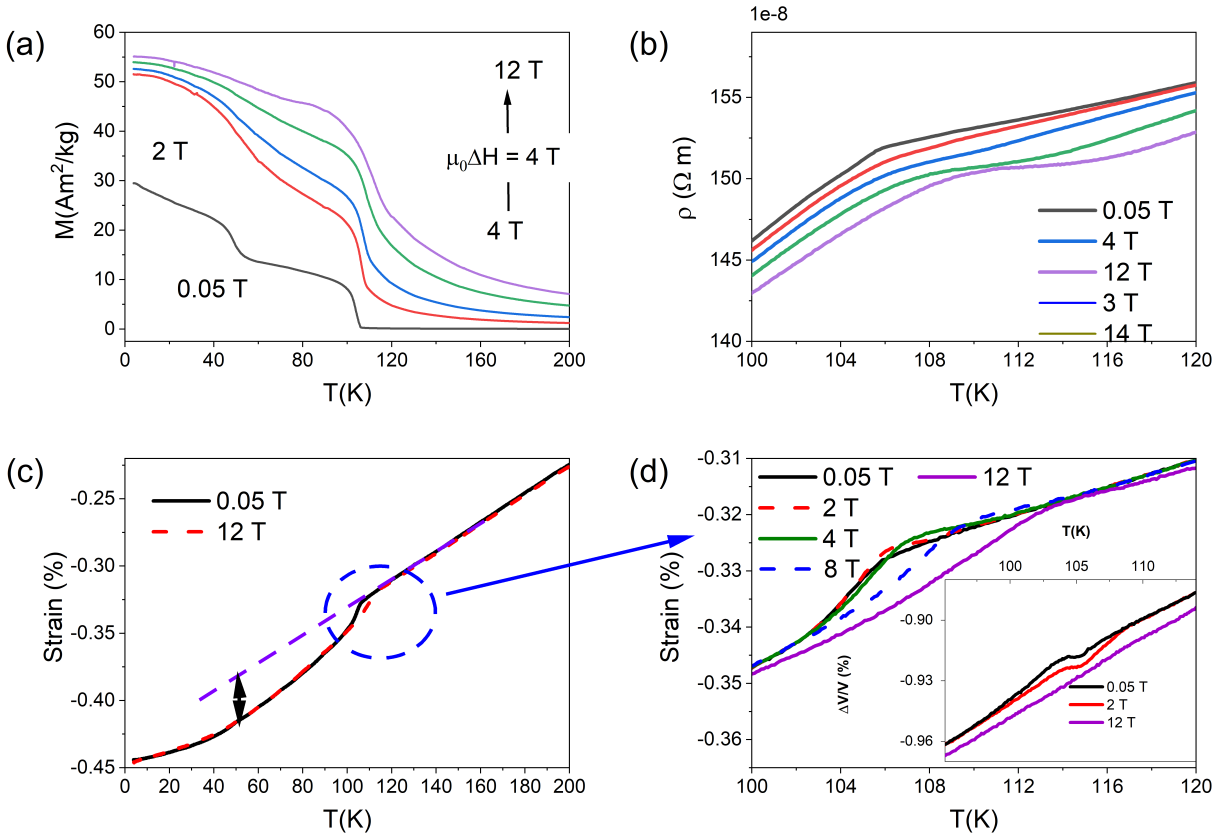

Figure 4.44: (a) Magnetization *vs.* temperature in fields of up to 12 T. (b) Electrical resistivity *vs.* temperature in magnetic fields of up to 12 T. (c) Longitudinal strain *vs.* temperature in magnetic fields of 0.05 and 12 T, the violet dashed line is the linear extrapolation of the paramagnetic regime. (d) Longitudinal strain as a function of temperature from 100 K to 120 K in magnetic fields of 0.05, 2, 8, and 12 T; the inset shows the volume change in magnetic fields of 0.05, 2, and 12 T.

Figure 4.44 (c) and (d) display the results of the longitudinal strain measurements in 0.05, 2, 4, 8, and 12 T. Although the phase transition in Nd_2In at about 108 K is confirmed to be of first-order, its strain across the phase transition is small, only 0.03%. The inset of **Figure 4.44** (d) demonstrates a nearly zero volume change across the phase transition.

In reference [203], the first-order phase transition of Eu_2In is theoretically demonstrated to be due to a full electronic mechanism. Though it is not clear whether the abnormal behavior of the longitudinal strain with magnetic field relates to the first-order phase transition of Nd_2In, a correlation in between is highly suspected.

4.4.3 A study on Pr_2In reveals the role of Debye temperature in achieving large adiabatic temperature change

The giant ΔS_T in Pr_2In at about 56 K makes it appealing for magnetocaloric hydrogen liquefaction [43]. However, as an equally important parameter as ΔS_T , ΔT_{ad} of Pr_2In showing a first-order phase transition is not reported. Knowing ΔT_{ad} is essential for evaluating the potential of a material for a magnetic cooling application.

Pr_2In sample was synthesized in the same way as Nd_2In. The XRD measurement and analysis were also conducted in the same way as Nd_2In. The results are shown in **Figure 4.45**. No obvious peaks from secondary phase are observed, confirming the high quality of the Pr_2In sample.

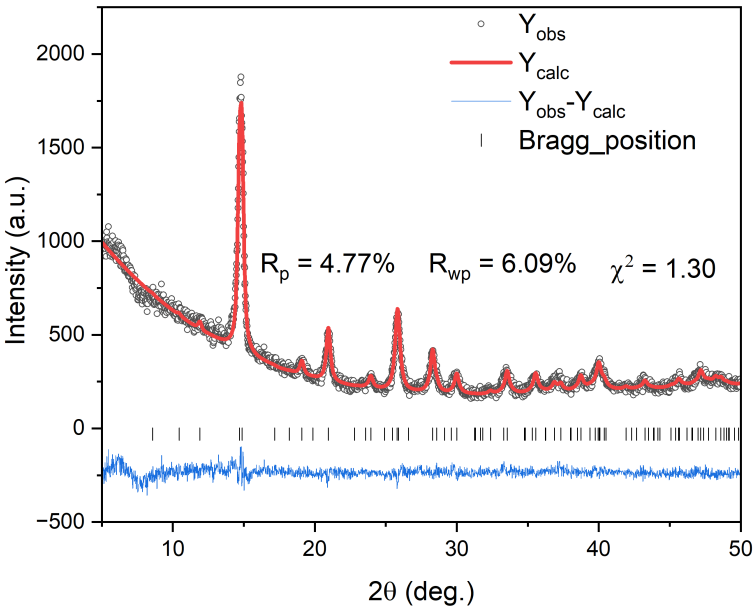

Figure 4.45: XRD measurement of Pr_2In and the results of the Rietveld refinement.

Figure 4.46 (a) plots the $M(T)$ curves of Pr_2In in magnetic fields of 0.02, 1, 2, 5, 10 T. Two magnetic phase transitions are observable: one at about 56 K, the other at about 30 K, agreeing with what were reported by Biswas *et al.*. ΔS_T from 0.25 up to 2 T is obtained from the $M(T)$ measurements based on the Maxwell relation via eq. (2.24). The $M(T)$ measurements used for calculating ΔS_T are plotted in the inset of **Figure 4.46** (a). The obtained ΔS_T are plotted in **Figure 4.46** (b). In magnetic fields of 1 T, ΔS_T reaches a value of about 12 J K^{-1} kg^{-1}. In magnetic fields of 2 T, this value becomes 17 J K^{-1} kg^{-1}. The ΔS_T of the Pr_2In in the present work is slightly larger than that reported in references [43]. To confirm that the phase transition order of the Pr_2In sample is of first, the quantitative criterion featuring the exponent n was performed, as already introduced in **Section 2.4.4** and performed for Nd_2In in **Section 4.4.2**. The n values overshoot 2, proving that the phase transition at about 56 K is of first-order.

Besides obtaining the ΔS_T from magnetization measurements, the ΔS_T were also calculated from heat capacity measurements by constructing the total entropy $S_{tot}(T, H)$ curves using eq. (2.2). **Figure 4.46** (c) compares the ΔS_T from heat capacity measurements and the ΔS_T from magnetization measurements. In magnetic fields of 2 and 5 T, ΔS_T from both methods matches well, as two plots almost overlap each other. The excellent match of these two methods proves the high quality of the heat capacity measurements, indicating that a reliable ΔT_{ad} can be obtained from these heat capacity data. **Figure 4.46** (d) shows the ΔT_{ad} obtained using eq. (2.18) from the constructed $S_{tot}(T, H)$ curves. In magnetic fields of 2 T, ΔT_{ad} reaches about 2 K. In magnetic fields of 5 T, ΔT_{ad} reaches about 4.3 K.

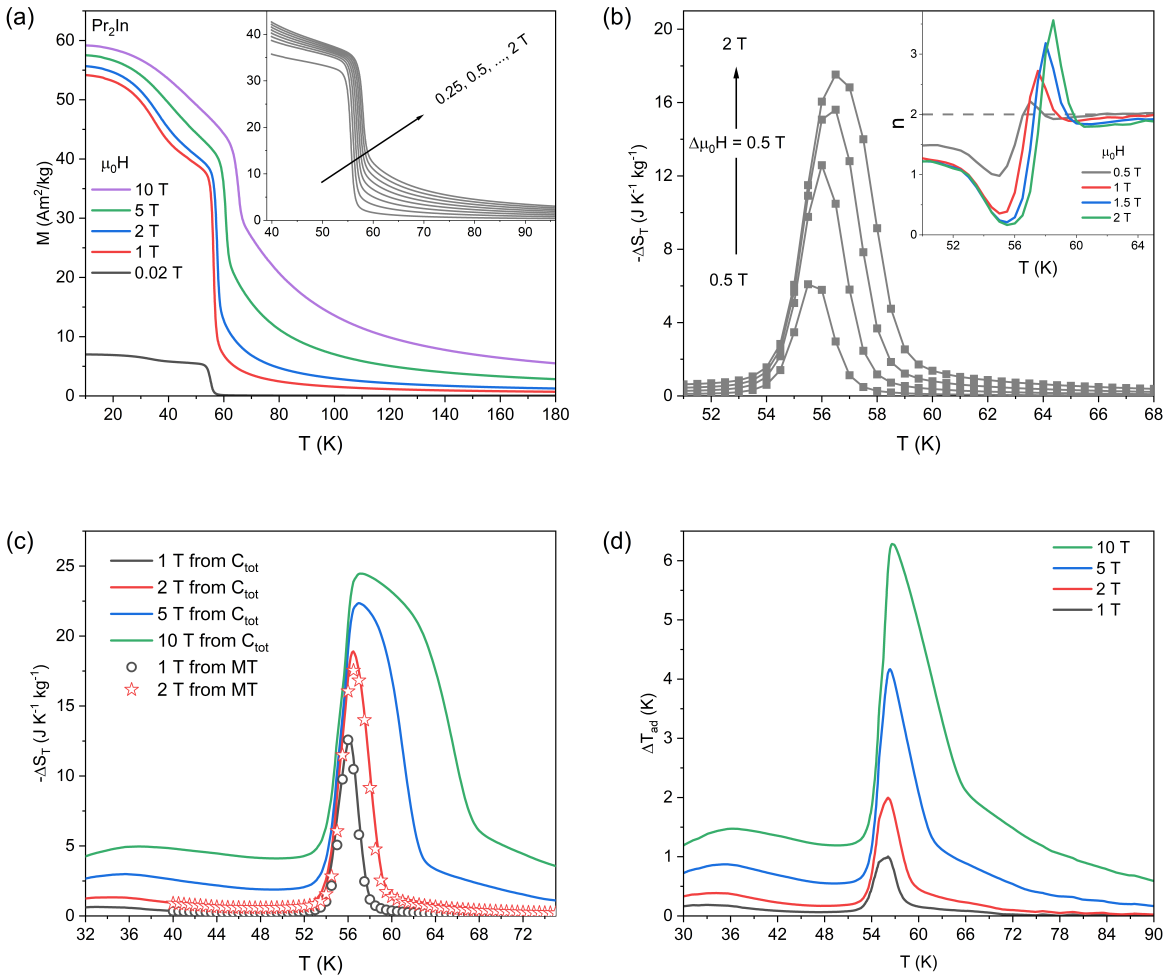

Figure 4.46: (a) $M(T)$ curves of Pr_2In in magnetic fields of 0.02, 1, 2, 5, 10 T. The inset shows the $M(T)$ curves for obtaining ΔS_T . (b) ΔS_T of Pr_2In from magnetization measurements. The inset shows n vs. T. (c) ΔS_T of Pr_2In from magnetization measurements and heat capacity measurements. (d) ΔT_{ad} from heat capacity measurements. Data are taken from references [12, 40, 123, 126, 200].

Unlike its impressive giant ΔS_T , Pr_2In does not show an impressive ΔT_{ad} . **Figure 4.47** (a) and (b) compare the ΔS_T and ΔT_{ad} of Pr_2In with the light rare-earth Laves phases, the heavy rare-earth Laves phases, and the heavy rare-earth-based R_2In (R: Tb, Dy, Ho, and Er) materials in magnetic fields of 5 T. Pr_2In does show a larger ΔT_{ad} than the light rare-earth Laves with a similar T_C . Considering the much larger ΔS_T , this observation is of no surprise. However, despite the fact that Pr_2In shows a larger ΔS_T , its ΔT_{ad} is much smaller than $DyAl_2$, reaching a value that is just half of that of $DyAl_2$ [12].

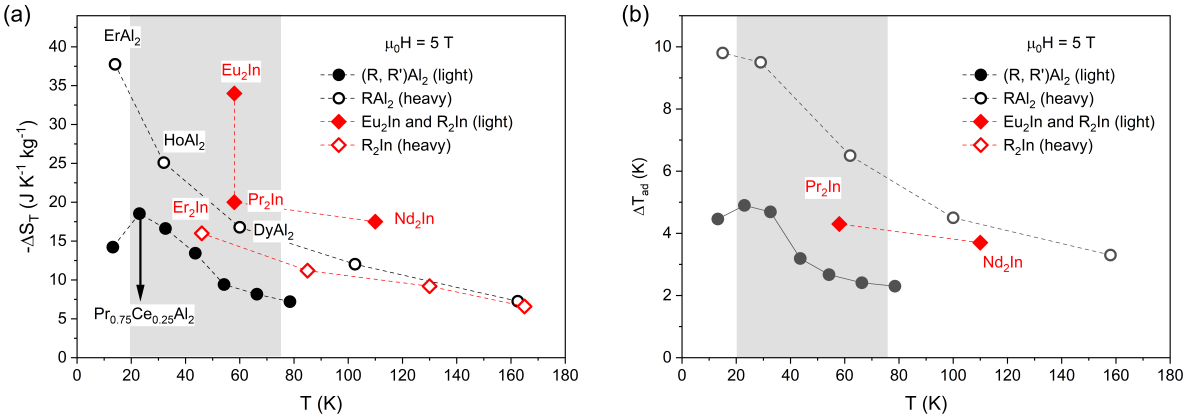

Figure 4.47: (a) ΔS_T for light and heavy rare-earth-based R_2In, RAl_2 , and RCo_2 (Pr, Nd, Eu, Tb, Dy, Ho, Er) in magnetic fields of 5 T. (b) The corresponding ΔT_{ad} .

In order to find out why the large ΔT_{ad} is absent in the Pr_2In sample, a close look is given to the heat capacity data, which are shown in **Figure 4.48** (a). Similar to Nd_2In, the heat capacity peak shifts with changing magnetic field. This is another sign of the first-order phase transition at about 56 K in the Pr_2In sample.

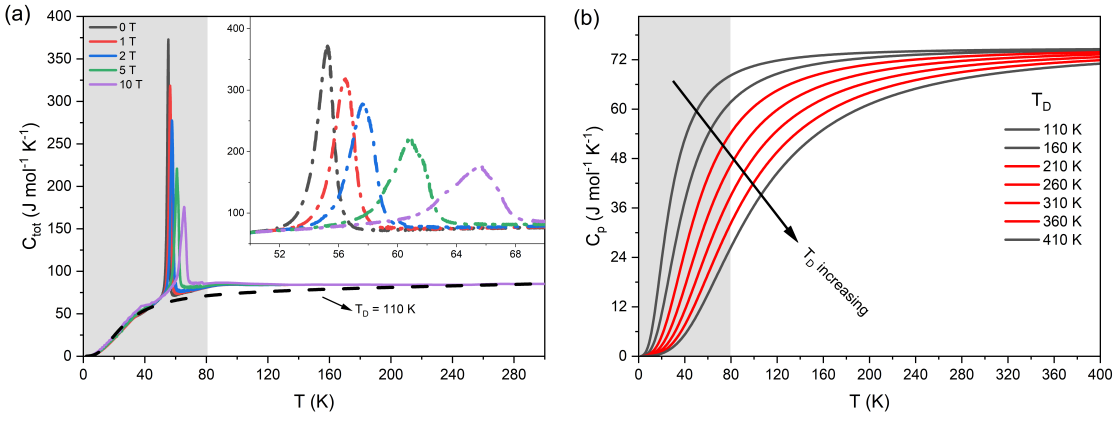

Figure 4.48: Heat capacity of Pr_2In as a function of temperature in magnetic fields of 0, 1, 2, 5, 10 T. (b) Volumetric lattice heat capacity from Debye model with different T_D.

Unlike the RAl_2 Laves phases of which the heat capacities are no longer constant with temperature in cryogenic temperature range, the heat capacity of Pr_2In is nearly constant even down to 80 K, showing a value of about $75\,\mathrm{J\,K^{-1}\,mol^{-1}}$ which is still close to the Dulong-Petit limit. This is a sign of a low Debye temperature.

To obtain the Debye temperature, fitting the heat capacity curve using the Debye model was conducted. The non-magnetic heat capacity can be fitted by

$$C_V + C_e = 9Nk_B \left(\frac{T}{T_D}\right)^3 \int_0^{\frac{T_D}{T}} \frac{x^4 e^x}{(e^x - 1)^2} + \gamma T. \tag{4.27}$$

It should be emphasized that the total heat capacity is often measured under isobaric conditions. A difference exists between the isobaric heat capacity C_p and the lattice heat capacity C_V:

$$C_p - C_V = \frac{9\alpha_T^2}{\kappa} VT, \tag{4.28}$$

where κ is the compressibility and α_T is the thermal expansion. A difference of 5% can exist, according to Tishin *et al.* [2]. In addition, only the harmonic vibration of the lattice is considered in the Debye model, with any anharmonic contributions neglected. Materials such as Gd showing a heat capacity of $30\,\mathrm{J\,K^{-1}\,mol^{-1}}$ well above room temperature, exceeding the Dulong-Petit limit of $24.3\,\mathrm{J\,K^{-1}\,mol^{-1}}$. Because of these limitations, **Section 4.4.3** can only give a rough estimate of T_D.

The fitting result suggests a T_D of around 110 K. **Figure 4.48** (b) displays the C_V of materials with a T_D from 110 to 410 K with a step of 50 K. Most alloys have a T_D in the range of $200 \sim 400$ K. As **Figure 4.48** (b) demonstrates, heat capacities of materials with a T_D from 210 to 410 K do not keep constant from room temperature down to 80 K anymore, while for $T_D = 110K$, only a slight decrease in heat capacity is observed. The T_D of $DyAl_2$ is reported to be around 374 K, much larger than that of Pr_2In.

The large difference in T_D between $DyAl_2$ and Pr_2In and the fact that $DyAl_2$ shows a smaller ΔS_T but a much larger ΔT_{ad} than Pr_2In led to the thinking that T_D might play an important role in achieving a large ΔT_{ad} . To work out the correlation between T_D and ΔT_{ad} , a series of hypothetical "Pr_2In" material systems that only vary in T_D is assumed. In each hypothetical "Pr_2In" material system, the material only varies in T_C , with the other properties staying the same. The hypothetical "Pr_2In" is assumed to undergo a second-order phase transition to reduce the complexity. These assumptions make it possible to conduct the mean-field appraoch on these materials systems. The J and g_J are taken to be 4 and 4/5 respectively, corresponding to the Pr ions.

Figure 4.49 (a) and (b) present the results of ΔS_T and ΔT_{ad} from the mean-field approach, respectively. Since ΔS_T is not correlated with T_D based on eq. (2.14), all the hypothetical "Pr_2In" material systems are in the same line of ΔS_T vs. T_C .

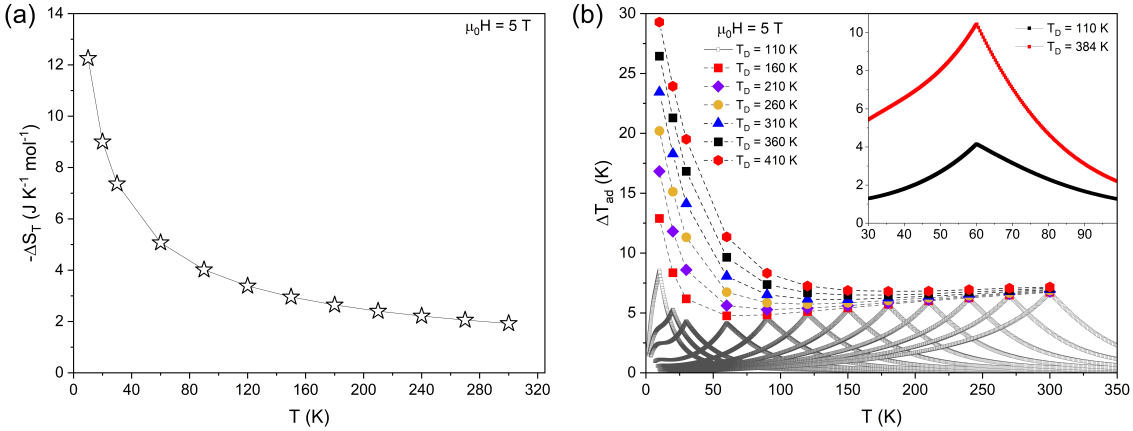

Figure 4.49: (a) ΔS_T of the "Pr_2In" systems from mean-field approach. (b) ΔT_{ad} of the "Pr_2In" systems from mean-field approach, the inset shows the ΔT_{ad} of the "Pr_2In" systems with T_D=110 and 384 K.

However, the T_D influences ΔT_{ad} . As shown in **Figure 4.49**, though near room temperature and above, these Pr_2In systems show a similar ΔT_{ad} . However, in cryogenic temperature range, ΔT_{ad} of different systems start to show a difference: the higher the T_D, the larger the ΔT_{ad} . At around 60 K, it is observed that ΔT_{ad} of a material with a T_D of 384 K is almost twice as large as that of a material with a T_D of 110 K.

From the above analysis, it is concluded that magnetocaloric materials with a higher T_D tend to exhibit a larger ΔT_{ad} . The work in this part explains the absence of large ΔT_{ad} in Pr_2In and highlights that "giant" magnetic entropy change does not necessarily lead to an excellent adiabatic temperature change. The conclusions in this part can serve as a tool to understand the magnetocaloric effect at cryogenic temperatures and may help with discovering or designing materials with both large magnetic and adiabatic temperatures changes.

5 Summary and outlook

In this work, heavy rare-earth Laves phases RAl_2 and RNi_2 (R: Gd, Tb, Dy, Ho, and Er), light rare-earth Laves phases $(R_1, R_2)Al_2$ (R_1: Nd, Pr; R_2: Pr, Ce), and light rare-earth-based R_2In (R: Nd, Pr) intermetallic compounds are investigated. This work focuses on their MCEs in the temperature range of $77 \sim 20$ K required by magnetocaloric hydrogen liquefaction. The goal is to develop magnetocaloric materials with strong MCEs and reduced criticality. This work can be summarized in three aspects:

1. Experimental and theoretical interpretations of increasing trends of MCEs with decreasing Curie temperature

Heavy rare-earth Laves phases are competitive candidates for magnetocaloric hydrogen liquefaction in terms of magnetocaloric performance. While studying the MCEs of the heavy rare-earth Laves phases RAl_2 and RNi_2, it is discovered that second-order magnetocaloric materials can achieve ΔS_T and ΔT_{ad} at low temperatures as "giant" as many of the giant first-order magnetocaloric materials. Taking into account the similarities of rare-earth elements, this study suggests that ΔS_T and ΔT_{ad} are highly correlated with T_C .

A comprehensive literature review is conducted to interpret the correlations between these three parameters. Two trends are revealed: (1) ΔS_T increases with decreasing T_C . (2) ΔT_{ad} decreases with decreasing T_C near room temperature but increases in the cryogenic temperature range. Additionally, a feature is summarized: second-order magnetocaloric materials with a T_C in the vicinity of the hydrogen condensation point can show giant MCEs.

Following the discoveries from the experiments, a mean-field approach is adopted to theoretically interpret these discoveries. The theoretical calculation demonstrates that ΔS_T increases with decreasing T_C , and the increasing trend becomes stronger toward lower temperatures, resulting in giant values of ΔS_T in the vicinity of the hydrogen condensation point (20 K). Unlike ΔS_T , the calculations on ΔT_{ad} show that ΔT_{ad} decreases first with decreasing T_C near room temperature, but increases in the cryogenic temperature range. Similar to ΔS_T , near 20 K, ΔT_{ad} increases sharply with decreasing T_C . The mean-field calculations are in line with the experimental study on the heavy rare-earth Laves phases and the literature review.

In addition to the mean-field approach, this work presents another theoretical interpretation based on the linear relation of $\Delta S_T^{max} \propto T_C^{-2/3}$. Mathematically, $f(x) = x^{-2/3}$ (x is any variable) is a function that increases faster toward smaller x. The linear relation of $\Delta S_T^{max} \propto T_C^{-2/3}$ is validated by the mean-field approach and the experimental data of the heavy rare-earth Laves phases.

2. Developing light rare-earth-based second-order magnetocaloric materials

For large-scale applications, the criticality of raw materials need to be considered. An analysis on the resource criticality of rare-earth elements is conducted. The results show that, although heavy rare-earth-based

magnetocaloric materials show an outstanding MCE, the high criticality of the heavy rare-earth elements is a major obstacle for scaling up magnetocaloric hydrogen liquefaction technology. On the contrary, light rare-earth elements such as Ce, Pr, and Nd are less critical than heavy rare-earth elements such as Tb, Dy, Ho, and Er. The lower criticality of light rare-earth elements makes their alloys appealing for large-scale application of magnetocaloric hydrogen liquefaction.

The above studies on the heavy rare-earth Laves phases points out the fact that maximum MCE gets enlarged by lowering T_C . Based on this finding, a method of tailoring the MCEs of the light rare-earth Laves $NdAl_2$ and $PrAl_2$ is applied: tune the T_C of the compounds down to 20 K by mixing different light rare-earth elements with different de Gennes factor at the rare-earth sublattice.

A fully light rare-earth-based Laves phase series $(R_1, R_2)Al_2$ (R1: Nd, Pr; R2: Pr,Ce) is successfully designed. This series covers a full temperature range of 77 ~20 K required by magnetocaloric hydrogen liquefaction with a competitive maximum ΔS_T and ΔT_{ad} . In particular, the (Pr, Ce)Al_2 samples show a ΔS_T that is larger than or comparable to $DyAl_2$, a heavy rare-earth-based magnetocaloric material ($T_C \approx 60K$) that is often proposed to be used in an active magnetic regenerator for hydrogen liquefaction due to its excellent magnetocaloric effect. ΔT_{ad} of the (Pr, Ce)Al_2 samples are slightly lower than that of $DyAl_2$.

3. Developing light rare-earth-based first-order magnetocaloric materials

The above studies demonstrate that light rare-earth-based magnetocaloric materials with a second-order phase transition are able to show excellent ΔS_T near the condensation point of hydrogen (20 K). However, it is discovered that the ΔS_T drops quickly up to the condensation point of nitrogen (77 K). This finding drives this work to focus on the light rare-earth-based magnetocaloric materials with a first-order phase transition.

Unlike its heavy rare-earth counterparts with a second-order phase transition, light rare-earth-based material Pr_2In demonstrates a first-order phase transition with a giant ΔS_T that is much larger than the ΔS_T of Er_2In, which is known to show the largest ΔS_T among the heavy rare-earth-based R_2In (R: Gd, Tb, Dy, Ho, and Er) alloys. Considering the similarities of Nd and Pr elements, a Nd_2In sample was prepared and its MCE was studied. Similar to Pr_2In, Nd_2In also shows a large ΔS_T at about 108 K that is even higher than Er_2In. The nature of its phase transition is confirmed to be first-order by the quantitative criterion featuring the exponent n from $\Delta S_T \propto H^n$ and the heat capacity measurements. The ΔT_{ad} measurements show that the MCE of Nd_2In is almost fully reversible, in agreement with the observation of nearly negligible thermal hysteresis in Nd_2In. Further studies on the magnetostrictive strain reveal a nearly zero volume change during phase transition.

Besides Nd_2In, the Pr_2In showing a first-order phase transition were further investigated, as there was no data in the literature on its ΔT_{ad} . Heat capacity measurements were carried out to obtain the ΔT_{ad} of Pr_2In. The results show that Pr_2In exhibits a ΔT_{ad} of about 4.3 K in magnetic fields of 5 T. This value is not as impressive as its giant ΔS_T . Pr_2In shows a higher ΔS_T than $DyAl_2$ in magnetic fields of 5 T, but its ΔT_{ad} reaches only half of that of $DyAl_2$. A close look at the heat capacity data shows that the Debye temperature of Pr_2In is low, only around 110 K. This discovery drives the work to focus on the correlation of Debye temperature and ΔT_{ad} . Via a mean-field approach, it is demonstrated that materials with a higher Debye temperature tend to show a larger ΔT_{ad} , in particular at cryogenic temperatures. This study reveals the role of Debye temperature in achieving large ΔT_{ad} and can serve as a tool for the search and design of magnetocaloric materials with both a large ΔS_T and a large ΔT_{ad} .

Concluding Remarks and Suggestions to Further Research

In short, from the studies on the heavy rare-earth Laves phases and a combined literature review on the heavy rare-earth-based magnetocaloric materials, the fact that maximum ΔS_T and ΔT_{ad} are enlarged by cryogenic temperature is revealed. Based on this finding and the knowledge that T_C can be tuned by tuning the de Gennes factors, the MCEs of the light rare-earth Laves $PrAl_2$ and $NdAl_2$ are tailored to cover the temperature range of $20 \sim 77$ K. A fully light rare-earth-based magnetocaloric material series is successfully developed, showing competitive maximum ΔS_T and ΔT_{ad} near 20 K. The discovery that this series does not show as excellent ΔS_T near 77 K as that near 20 K drives the work to explore first-order light rare-earth-based magnetocaloric materials. The large ΔS_T in Nd_2In is discovered, and its peculiar first-order phase transition is studied. In addition, via the study on Pr_2In, it is revealed that materials with higher Debye temperature tend to exhibit larger ΔT_{ad} .

This work points out a pathway to develop rare-earth-based magnetocaloric materials with reduced criticality and enhanced magnetocaloric performance: developing light rare-earth-based first-order magnetocaloric materials. However, the R_2In (R: Nd and Pr) explored in this work contain Indium, an element that is highly critical. Further research should focus on reducing the usage of indium. Considering the significant influence of Debye temperature on ΔT_{ad} , potential ways of increasing the Debye temperatures of the R_2In materials while keeping their nature of first-order phase transitions need to be explored to achieve both a large ΔS_T and a large ΔT_{ad} . In addition, all of the samples discussed in this work are polycrystalline. Recent research shows that texture can lead to an enhancement of ΔS_T and ΔT_{ad} of rare-earth-based magnetocaloric materials [107]. It is of great importance to optimize the microstructure of the rare-earth-based magnetocaloric materials for optimized ΔS_T and ΔT_{ad} .

References

[1] A. Smith. “Who discovered the magnetocaloric effect?” In: *Eur. Phys. J. H* 38 (2013), pp. 507–517. DOI: 10.1140/epjh/e2013-40001-9 (cited on pp. 1, 6).

[2] A. M. Tishin and Y. I. Spichkin. *The Magnetocaloric Effect and its Applications*. 1st Edition. Boca Raton, Florida, USA: CRC Press, 2003. ISBN: 9780429141379. DOI: 10.1201/9781420033373 (cited on pp. 1, 45, 50–52, 81).

[3] W. F. Giauque and D. P. MacDougall. “Attainment of Temperatures Below 1° Absolute by Demagnetization of $Gd_2(SO_4)_3 \cdot 8H_2O$”. In: *Physical Review* 43 (1933), p. 768. DOI: 10.1103/PhysRev.43.768 (cited on pp. 1, 6).

[4] M. A. Shampo, Robert K. A., and D. P. Steensma. “William F. Giauque—Nobel Prize for Low-Temperature Research”. In: *Mayo Clin. Proc.* 81 (2006), p. 587. DOI: 10.4065/81.5.587 (cited on pp. 1, 6).

[5] IPCC. *Climate change 2022: Mitigation of climate change*. Ed. by P. R. Shukla, J. Skea, R. Slade, A. AI Khourdajie, R. van Diemen, D. McCollum, M. Pathak, S. Some, P. Vyas, R. Fradera, M. Belkacemi, A. Hasija, G. Lisboa, S. Luz, J. Malley. Cambridge, UK and New York, NY, USA, 2022. URL: https://www.ipcc.ch/report/ar6/wg3/downloads/report/IPCC_AR6_WGIII_FullReport.pdf (cited on p. 1).

[6] W. Cornwall. “Five years in, Paris pact still a work in progress”. In: *Science* 370 (2020), p. 1390. DOI: 10.1126/science.370.6523.1390 (cited on p. 1).

[7] Editorials. “Net-zero carbon pledges must be meaningful to avert climate disaster”. In: *Nature* 592 (2021), p. 8. DOI: 10.1038/d41586-021-00864-9 (cited on p. 1).

[8] Zainul Abdin et al. “Hydrogen as an energy vector”. In: *Renew. Sust. Energ. Rev.* 120 (2020), p. 109620. DOI: 10.1016/j.rser.2019.109620 (cited on p. 1).

[9] Sonja van Renssen. “The hydrogen solution?” In: *Nat. Clim. Change* 10 (2020), pp. 799–801. DOI: 10.1038/s41558-020-0891-0 (cited on p. 1).

[10] Ankica Kovač, Matej Paranos, and Doria Marciuš. “Hydrogen in energy transition: A review”. In: *Int. J. Refrig.* 46 (2021), pp. 10016–10035. DOI: 10.1016/j.ijhydene.2020.11.256 (cited on p. 1).

[11] Joakim Andersson and Stefan Grönkvist. “Large-scale storage of hydrogen”. In: *Int. J. Hydrog. Energy* 44 (2019), pp. 11901–11919. DOI: 10.1016/j.ijhydene.2019.03.063 (cited on p. 2).

[12] Wei Liu et al. “A study on rare-earth Laves phases for magnetocaloric liquefaction of hydrogen”. In: *Appl. Mater. Today* 29 (2022), p. 101624. DOI: 10.1016/j.apmt.2022.101624 (cited on pp. 2, 3, 31–33, 43, 45, 69, 70, 73, 79, 80).

[13] Majid Aasadnia and Mehdi Mehrpooya. “Large-scale liquid hydrogen production methods and approaches: A review”. In: *Appl. Energy* 212 (2018), pp. 57–83. DOI: 10.1016/j.apenergy.2017.12.033 (cited on p. 2).

[14] George W. Crabtree, Mildred S. Dresselhaus, and Michelle V. Buchanan. “The Hydrogen Economy”. In: *Phys. Today* 57 (2004), pp. 39–44. DOI: 10.1063/1.1878333 (cited on p. 2).

[15] Shoji Kamiya, Motohiko Nishimura, and Eichi Harada. “Study on Introduction of CO_2 Free Energy to Japan with Liquid Hydrogen”. In: *Phys. Procedia* 67 (2015), pp. 11–19. DOI: 10.1016/j.phpro.2015.06.004 (cited on p. 2).

[16] Jiawei Lai et al. “Machine learning assisted development of Fe2P-type magnetocaloric compounds for cryogenic applications”. In: *Acta Mater.* 232 (2022), p. 117942. DOI: 10.1016/j.actamat.2022.117942 (cited on p. 2).

[17] Xin Tang et al. “Magnetic refrigeration material operating at a full temperature range required for hydrogen liquefaction”. In: *Nat. Commun.* 13.1 (2022), p. 1817. DOI: 10.1038/s41467-022-29340-2 (cited on pp. 2, 64).

[18] Noriki Terada and Hiroaki Mamiya. “High-efficiency magnetic refrigeration using holmium”. In: *Nature Commun.* 12 (2021), p. 1212. DOI: 10.1038/s41467-021-21234-z (cited on p. 2).

[19] Shuxian Yang et al. “Giant low-field magnetocaloric effect in ferromagnetically ordered $Er_{1-x}Tm_xAl_2$ ($0 \leq x \leq 1$) compounds”. In: *J. Mater. Sci. Technol.* 146 (2023), pp. 168–176. DOI: 10.1016/j.jmst.2022.10.066 (cited on p. 2).

[20] Zhipan Ma et al. “Achievement of promising cryogenic magnetocaloric performances in $La_{1-x}Pr_xFe_{12}B_6$ compounds”. In: *J. Mater. Sci. Technol.* 92 (2021), pp. 138–142. DOI: 10.1016/j.jmst.2021.02.055 (cited on p. 2).

[21] Huilong Hou, Suxin Qian, and Ichiro Takeuchi. “Materials, physics and systems for multicaloric cooling”. In: *Nat. Rev. Mater.* 7 (2022), pp. 633–652. DOI: 10.1038/s41578-022-00428-x (cited on p. 2).

[22] Andrej Kitanovski. “Energy Applications of Magnetocaloric Materials”. In: *Adv. Energy Mater.* 10 (2020), p. 1903741. DOI: 10.1002/aenm.201903741 (cited on p. 2).

[23] Tino Gottschall et al. “Making a Cool Choice: The Materials Library of Magnetic Refrigeration”. In: *Adv. Energy Mater.* 9 (2019), p. 1901322. DOI: 10.1002/aenm.201901322 (cited on pp. 2, 13, 14, 30, 31, 43).

[24] X Moya, Sohini Kar-Narayan, and Neil David Mathur. “Caloric materials near ferroic phase transitions”. In: *Nat. Mater.* 13 (2014), pp. 439–450. DOI: 10.1038/nmat3951 (cited on p. 2).

[25] Xavier Moya and ND Mathur. “Caloric materials for cooling and heating”. In: *Science* 370 (2020), pp. 797–803. DOI: 10.1126/science.abb0973 (cited on p. 2).

[26] Tianshi Feng, Renkun Chen, and Robin V. Ihnfeldt. “Modeling of hydrogen liquefaction using magnetocaloric cycles with permanent magnets”. In: *Int. J. Refrig.* 119 (2020), pp. 238–246. DOI: 10.1016/j.ijrefrig.2020.06.032 (cited on p. 2).

[27] Oliver Gutfleisch et al. “Magnetic materials and devices for the 21st century: stronger, lighter, and more energy efficient”. In: *Adv. Mater.* 23 (2011), pp. 821–842. DOI: 10.1002/adma.201002180 (cited on p. 2).

[28] O. Gutfleisch et al. “Mastering hysteresis in magnetocaloric materials”. In: *Philos. Trans. R. Soc. A-Math. Phys. Eng. Sci.* 374 (2016). DOI: 10.1098/rsta.2015.0308 (cited on pp. 2, 45).

[29] Koji Kamiya et al. “Active magnetic regenerative refrigeration using superconducting solenoid for hydrogen liquefaction”. In: *Appl. Phys. Express* 15 (2022), p. 053001. DOI: 10.35848/1882-0786/ac5723 (cited on pp. 2, 3, 6).

[30] T. Numazawa et al. “Magnetic refrigerator for hydrogen liquefaction”. In: *Cryogenics* 62 (2014), pp. 185–192. DOI: 10.1016/j.cryogenics.2014.03.016 (cited on p. 2).

[31] Hu Zhang et al. “Review on the materials and devices for magnetic refrigeration in the temperature range of nitrogen and hydrogen liquefaction”. In: *Physica B: Condensed Matter* (2019), pp. 65–73. DOI: 10.1016/j.physb.2019.01.035 (cited on p. 2).

[32] K. A. GschneidnerJr, V. K. Pecharsky, and A. O. Tsokol. “Recent developments in magnetocaloric materials”. In: *Rep. Prog. Phys.* 68 (2005), pp. 1479–1539. DOI: 10.1088/0034-4885/68/6/R04 (cited on p. 2).

[33] Hu Zhang and Bao-Gen Shen. “Magnetocaloric effects in RTX intermetallic compounds (R = Gd–Tm, T = Fe–Cu and Pd, X = Al and Si)”. In: *Chin. Phys. B* 24 (2015), p. 127504. DOI: 10.1088/1674-1056/24/12/127504 (cited on pp. 2, 3).

[34] Xin-Qi Zheng and Bao-Gen Shen. “The magnetic properties and magnetocaloric effects in binary R – T (R = Pr, Gd, Tb, Dy, Ho, Er, Tm; T = Ga, Ni, Co, Cu) intermetallic compounds”. In: *Chinese Physics B* 26 (2017), p. 027501. DOI: 10.1088/1674-1056/26/2/027501 (cited on p. 2).

[35] E. Bykov et al. “Magnetocaloric effect in the Laves-phase $Ho_{1-x}Dy_xAl_2$ family in high magnetic fields”. In: *Phys. Rev. Mater.* 5 (2021). DOI: 10.1103/PhysRevMaterials.5.095405 (cited on pp. 2, 3, 47).

[36] M. Balli, D. Fruchart, and D. Gignoux. “A study of magnetism and magnetocaloric effect in $Ho_{1-x}Tb_xCo_2$ compounds”. In: *J. Magn. Magn.* 314 (2007), pp. 16–20. DOI: 10.1016/j.jmmm.2007.02.007 (cited on pp. 2, 43).

[37] V. Franco et al. “Magnetocaloric effect: From materials research to refrigeration devices”. In: *Prog. Mater. Sci.* 93 (2018), pp. 112–232. DOI: 10.1016/j.pmatsci.2017.10.005 (cited on p. 2).

[38] Volker Zepf. *Rare Earth Elements: What and where they are*. Springer, 2013. ISBN: 978-3-642-35457-1. DOI: 10.1007/978-3-642-35458-8_2 (cited on pp. 3, 55).

[39] John MD Coey. *Magnetism and magnetic materials*. Cambridge university press, 2010 (cited on pp. 3, 32, 40, 57).

[40] Wei Liu et al. "Designing magnetocaloric materials for hydrogen liquefaction with light rare-earth Laves phases". In: *J. Phys. Energy* 5 (2023), p. 034001. DOI: 10.1088/2515-7655/accb0b (cited on pp. 3, 64, 66, 73, 79).

[41] Li-Chen Wang and Bao-Gen Shen. "Magnetic properties and magnetocaloric effects of PrSi". In: *Rare Metals* 33 (2014), pp. 239–243. DOI: 10.1007/s12598-014-0310-7 (cited on p. 3).

[42] A Magnus G Carvalho et al. "Experimental and theoretical analyses of $PrAl_2$ and $NdAl_2$ composite for use as an active magnetic regenerator". In: *J. Appl. Phys.* 97 (2005). DOI: 10.1063/1.1876575 (cited on pp. 3, 60).

[43] Anis Biswas et al. "First-order magnetic phase transition in Pr_2In with negligible thermomagnetic hysteresis". In: *Phys. Rev. B* 101 (2020), p. 224402. DOI: 10.1103/PhysRevB.101.224402 (cited on pp. 3, 73–75, 78).

[44] Wei Liu et al. "Large magnetic entropy change in Nd_2In near the boiling temperature of natural gas". In: *Appl. Phys. Lett.* 119 (2021). DOI: 10.1063/5.0054959 (cited on pp. 3, 74).

[45] Zaira Navas-Anguita, Diego García-Gusano, and Diego Iribarren. "A review of techno-economic data for road transportation fuels". In: *Renew. Sustain. Energy Rev.* 112 (2019), pp. 11–26. DOI: 10.1016/j.rser.2019.05.041 (cited on p. 4).

[46] Kasper T Møller et al. "Hydrogen-A sustainable energy carrier". In: *Prog. Nat. Sci.: Mater. Int.* 27 (2017), pp. 34–40. DOI: 10.1016/j.pnsc.2016.12.0146 (cited on p. 4).

[47] P.P. Edwards et al. "Hydrogen and fuel cells: Towards a sustainable energy future". In: *Energy Policy* 36 (2008), pp. 4356–4362. ISSN: 0301-4215. DOI: 10.1016/j.enpol.2008.09.036 (cited on p. 4).

[48] Evangelos Tzimas et al. "Hydrogen storage: state-of-the-art and future perspective". In: *EU Commission, JRC Petten, EUR 20995EN* (2003). URL: https://publications.jrc.ec.europa.eu/repository/handle/JRC26493 (cited on p. 4).

[49] *The Liquefaction of Gases – Part I*. http://web.archive.org/web/20080207010024/http://www.808multimedia.com/winnt/kernel.htm. Accessed: 2013-07-13 (cited on p. 4).

[50] Pierre Weiss and Auguste Piccard. "Le phénomène magnétocalorique". In: *J. Phys. Theor. Appl.* 7 (1917), pp. 103–109 (cited on p. 6).

[51] Peter Debye. "Einige bemerkungen zur magnetisierung bei tiefer temperatur". In: *Annalen der Physik* 386 (1926), pp. 1154–1160 (cited on p. 6).

[52] WF Giauque. “A thermodynamic treatment of certain magnetic effects. A proposed method of producing temperatures considerably below 1° absolute”. In: *Journal of the American Chemical Society* 49 (1927), pp. 1864–1870 (cited on p. 6).

[53] G. V. Brown. “Magnetic heat pumping near room temperature”. In: *Journal of Applied Physics* 47 (1976), pp. 3673–3680. DOI: 10.1063/1.323176 (cited on p. 6).

[54] JA Barclay. “Use of a ferrofluid as the heat-exchange fluid in a magnetic refrigerator”. In: *Journal of Applied Physics* 53 (1982), pp. 2887–2894. DOI: 10.1063/1.331069 (cited on p. 6).

[55] John Barclay et al. “Propane liquefaction with an active magnetic regenerative liquefier”. In: *Cryogenics* 100 (2019), pp. 69–76. DOI: 10.1016/j.cryogenics.2019.01.009 (cited on p. 6).

[56] Corey Archipley et al. “Methane liquefaction with an active magnetic regenerative refrigerator”. In: *Cryogenics* 128 (2022), p. 103588. DOI: 10.1016/j.cryogenics.2022.103588 (cited on p. 6).

[57] Inmyong Park et al. “Design method of the layered active magnetic regenerator (AMR) for hydrogen liquefaction by numerical simulation”. In: *Cryogenics* 70 (2015), pp. 57–64. DOI: 10.1016/j.cryogenics.2015.04.007 (cited on p. 7).

[58] J. S. Amaral and V. S. Amaral. “On estimating the magnetocaloric effect from magnetization measurements”. In: *J. Magn. Magn.* 322 (2010), pp. 1552–1557. DOI: 10.1016/j.jmmm.2009.06.013 (cited on p. 12).

[59] ME Wood and WH Potter. “General analysis of magnetic refrigeration and its optimization using a new concept: maximization of refrigerant capacity”. In: *Cryogenics* 25 (1985), pp. 667–683. DOI: 10.1016/0011-2275(85)90187-0 (cited on p. 13).

[60] Xavier Moya et al. “Too cool to work”. In: *Nat. phys.* 11 (2015), pp. 202–205. DOI: 10.1038/nphys3271 (cited on pp. 13, 14).

[61] KA Gschneidner Jr and Vitalij K Pecharsky. “Magnetocaloric materials”. In: *Annu. Rev. Mater. Sci.* 30 (2000), pp. 387–429. DOI: 10.1146/annurev.matsci.30.1.387 (cited on p. 13).

[62] L. D. Griffith et al. “Material-based figure of merit for caloric materials”. In: *J. Appl. Phys.* 123 (2018), p. 034902. DOI: 10.1063/1.5004173 (cited on pp. 13, 14).

[63] Anders Smith et al. “Materials challenges for high performance magnetocaloric refrigeration devices”. In: *Adv. Energy Mater.* 2 (2012), pp. 1288–1318. DOI: 10.1002/aenm.201200167 (cited on pp. 13, 16, 61, 76).

[64] Julia Herrero-Albillos et al. “Nature and entropy content of the ordering transitions in RCo_2”. In: *Phys. Rev. B* 73 (2006). DOI: 10.1103/PhysRevB.73.134410 (cited on p. 16).

[65] Julia Herrero-Albillos et al. “Reply to “Comment on ‘Nature and entropy content of the ordering transitions in RCo_2 ’ ””. In: *Phys. Rev. B* 75 (2007). DOI: 10.1103/PhysRevB.75.187402. URL: https://journals.aps.org/prb/pdf/10.1103/PhysRevB.75.187402 (cited on p. 16).

[66] M. Forker et al. “Comment on “Nature and entropy content of the ordering transitions in RCo_2 ””. In: *Phys. Rev. B* 75 (2007). DOI: 10.1103/PhysRevB.75.187401. URL: https://journals.aps.org/prb/pdf/10.1103/PhysRevB.75.187401 (cited on p. 16).

[67] M. Forker et al. “Perturbed angular correlation study of the magnetic phase transitions in the rare-earth cobalt Laves phases RCo_2”. In: *Phys. Rev. B* 68 (2003). DOI: 10.1103/PhysRevB.68.014409. URL: https://journals.aps.org/prb/pdf/10.1103/PhysRevB.68.014409 (cited on p. 16).

[68] Tino Gottschall et al. “Large reversible magnetocaloric effect in Ni-Mn-In-Co”. In: *Appl. Phys. Lett.* 106.2 (2015), p. 021901. DOI: 10.1063/1.4905371 (cited on p. 18).

[69] Jia Yan Law et al. “A quantitative criterion for determining the order of magnetic phase transitions using the magnetocaloric effect”. In: *Nat. commun.* 9 (2018), p. 2680. DOI: 10.1038/s41467-018-05111-w (cited on pp. 19, 76).

[70] Jian Liu et al. “Giant magnetocaloric effect driven by structural transitions”. In: *Nat. Mater.* 11 (2012), pp. 620–626. DOI: 10.1038/nmat3334 (cited on pp. 26, 30).

[71] C. Salazar Mejía et al. “On the High-Field Characterization of Magnetocaloric Materials Using Pulsed Magnetic Fields”. In: *J. Phys. Energy* 5 (), p. 034006. DOI: 10.1088/2515-7655/acd47d (cited on p. 27).

[72] K. P. Skokov et al. “A multi-stage, first-order phase transition in $LaFe_{11.8}Si_{1.2}$: Interplay between the structural, magnetic, and electronic degrees of freedom”. In: *Appl. Phys. Rev.* 10 (2023), p. 031408 (cited on p. 29).

[73] V. K. Pecharsky and Gschneidner, Jr., K. A. “Giant Magnetocaloric Effect in $Gd_5(Si_2Ge_2)$”. In: *Phys. Rev. Lett.* 78 (1997), pp. 4494–4497. DOI: 10.1103/PhysRevLett.78.4494 (cited on pp. 30, 31).

[74] Jia Yan Law et al. “Current perspective in magnetocaloric materials research”. In: *J. Appl. Phys.* 133 (2023). DOI: 10.1063/5.0130035 (cited on p. 30).

[75] X. X. Zhang et al. “Magnetic entropy change in Fe-based compound $LaFe_{10.6}Si_{2.4}$”. In: *Appl. Phys. Lett.* 77 (2000), pp. 3072–3074. DOI: 10.1063/1.1323993 (cited on p. 30).

[76] ZD Han et al. “Large magnetic entropy changes in the $Ni_{45.4}Mn_{41.5}In_{13.1}$ ferromagnetic shape memory alloy”. In: *Appl. Phys. Lett.* 89 (2006). DOI: 10.1063/1.2385147 (cited on p. 30).

[77] Thorsten Krenke et al. “Inverse magnetocaloric effect in ferromagnetic Ni-Mn-Sn alloys”. In: *Nat. Mater.* 4 (2005), pp. 450–454. DOI: 10.1038/nmat1395 (cited on p. 30).

[78] Z. Y. Wei et al. “Magnetostructural martensitic transformations with large volume changes and magneto-strains in all- d -metal Heusler alloys”. In: *Appl. Phys. Lett.* 109 (2016), p. 071904. DOI: 10.1063/1.4961382 (cited on p. 30).

[79] Z. Y. Wei et al. “Realization of multifunctional shape-memory ferromagnets in all- d -metal Heusler phases”. In: *Appl. Phys. Lett.* 107 (2015), p. 022406. DOI: 10.1063/1.4927058 (cited on p. 30).

[80] O. Tegus et al. “Transition-metal-based magnetic refrigerants for room-temperature applications”. In: *Nature* 415 (2002), pp. 150–152. DOI: 10.1038/415150a (cited on p. 30).

[81] H. Wada and Y. Tanabe. “Giant magnetocaloric effect of $MnAs_{1-x}Sb_x$”. In: *Appl. Phys. Lett.* 79 (2001), pp. 3302–3304. DOI: 10.1063/1.1419048 (cited on p. 30).

[82] M. Balli et al. “Advanced materials for magnetic cooling: Fundamentals and practical aspects”. In: *Appl. Phys. Rev.* 4.2 (2017), p. 021305. DOI: 10.1063/1.4983612 (cited on p. 30).

[83] O. Tegus et al. “Magnetic and magneto-caloric properties of $Tb_5Si_2Ge_2$”. In: *Journal of Applied Physics* 91.10 (2002), pp. 8534–8536. DOI: 10.1063/1.1450830 (cited on p. 30).

[84] Andreas Taubel et al. “Tailoring magnetocaloric effect in all-d-metal Ni-Co-Mn-Ti Heusler alloys: a combined experimental and theoretical study”. In: *Acta Mater.* 201 (2020), pp. 425–434. DOI: 10.1016/j.actamat.2020.10.013 (cited on p. 30).

[85] Andreas Taubel et al. “A Comparative Study on the Magnetocaloric Properties of Ni-Mn-X(-Co) Heusler Alloys”. In: *Phys. Status Solidi B* 255 (2018), p. 1700331. DOI: 10.1002/pssb.201700331 (cited on pp. 30, 31).

[86] A. Chirkova et al. “Giant adiabatic temperature change in FeRh alloys evidenced by direct measurements under cyclic conditions”. en. In: *Acta Materialia* 106 (2016), pp. 15–21. DOI: 10.1016/j.actamat.2015.11.054 (cited on p. 30).

[87] N. H. Dung et al. “From first-order magneto-elastic to magneto-structural transition in $(Mn,Fe)_{1.95}P_{0.50}Si_{0.50}$”. en. In: *Appl. Phys. Lett.* 99.9 (2011), p. 092511. DOI: 10.1063/1.3634016. (Visited on 01/20/2024) (cited on p. 30).

[88] A.T. Saito, T. Kobayashi, and H. Tsuji. “Magnetocaloric effect of new spherical magnetic refrigerant particles of $La(Fe_{1-x-y}Co_xSi_y)_{13}$ compounds”. In: *J. Magn. Magn.* 310.2 (2007), pp. 2808–2810. DOI: 10.1016/j.jmmm.2006.10.1058 (cited on p. 30).

[89] M. Balli, D. Fruchart, and D. Gignoux. “Magnetic behaviour and experimental study of the magnetocaloric effect in the pseudobinary Laves phase $Er_{1-x}Dy_xCo_2$”. In: *J. Alloys Compd.* 509.9 (2011), pp. 3907–3912. DOI: 10.1016/j.jallcom.2010.12.161 (cited on pp. 30, 43).

[90] F. X. Hu et al. “Direct measurements of magnetocaloric effect in the first-order system $LaFe_{11.7}Si_{1.3}$”. In: *J. Appl. Phys.* 93.9 (2003), pp. 5503–5506. DOI: 10.1063/1.1563036 (cited on p. 30).

[91] F. Scheibel et al. “Dependence of the inverse magnetocaloric effect on the field-change rate in Mn_3GaC and its relationship to the kinetics of the phase transition”. In: *J. Appl. Phys.* 117 (2015), p. 233902. DOI: 10.1063/1.4922722 (cited on pp. 30, 31).

[92] Pedro Baptista de Castro et al. “Machine-learning-guided discovery of the gigantic magnetocaloric effect in HoB_2 near the hydrogen liquefaction temperature”. In: *NPG Asia Mater.* 12 (2020). DOI: 10.1038/s41427-020-0214-y (cited on pp. 30, 31, 43).

[93] M Balli, D Fruchart, and D Gignoux. "Optimization of La (Fe, Co)$_{13-x}$Si$_x$ based compounds for magnetic refrigeration". In: *J.Phys. Condens. Matter* 19 (2007), p. 236230 (cited on pp. 30, 31).

[94] Yan-Cong Chen et al. "A brilliant cryogenic magnetic coolant: magnetic and magnetocaloric study of ferromagnetically coupled GdF_3". In: *J. Mater. Chem. C* 3 (2015), pp. 12206–12211. DOI: 10.1039/C5TC02352A (cited on pp. 30, 31).

[95] Song-De Han et al. "Large magnetocaloric effect in a dense and stable inorganic-organic hybrid cobridged by in situ generated sulfate and oxalate". In: *Chemistry – An Asian Journal* 9.11 (2014), pp. 3116–3120. DOI: 10.1002/asia.201402777 (cited on p. 30).

[96] S. A. Nikitin et al. "The magnetocaloric effect in $Fe_{49}Rh_{51}$ compound". In: *Phys. Lett. A* 148 (1990), pp. 363–366. DOI: 10.1016/0375-9601(90)90819-A (cited on p. 31).

[97] J. W. Xu et al. "Giant low field magnetocaloric effect in TmCoSi and TmCuSi compounds". In: *Journal of Alloys and Compounds* (2020), p. 155930. DOI: 10.1016/j.jallcom.2020.155930 (cited on pp. 31, 43).

[98] Lingwei Li et al. "Low-field giant reversible magnetocaloric effect in intermetallic compound $ErCr_2Si_2$". In: *Scripta Materialia* 67 (2012), pp. 237–240. DOI: 10.1016/j.scriptamat.2012.04.028 (cited on pp. 31, 43).

[99] K.P. Skokov et al. "Influence of thermal hysteresis and field cycling on the magnetocaloric effect in $LaFe_{11.6}Si_{1.4}$". In: *J. Alloys Compd.* 552 (2013), pp. 310–317. DOI: 10.1016/j.jallcom.2012.10.008 (cited on p. 31).

[100] Maximilian Fries et al. "Microstructural and magnetic properties of Mn-Fe-P-Si (Fe_2P-type) magnetocaloric compounds". In: *Acta Mater.* 132 (2017), pp. 222–229. DOI: 10.1016/j.actamat.2017.04.040 (cited on p. 31).

[101] V. Franco et al. "The magnetocaloric effect in materials with a second order phase transition: Are T_C and T_{peak} necessarily coincident?" In: *J. Appl. Phys.* 105 (Apr. 2009), 07A917. DOI: 10.1063/1.3063666 (cited on p. 32).

[102] Jr. Karl A. Gschneidner and Vitalij K. Pecharsky. "Binary rare earth Laves phases — an overview". In: *Zeitschrift für Kristallographie - Crystalline Materials* 221 (2006). ISSN: 2194-4946 (cited on pp. 33, 34).

[103] AF Deutz et al. "Magnetic properties of the induced moment system $TmNi_2$". In: *J. Magn. Magn.* 78 (1989), pp. 176–182. DOI: 10.1016/0304-8853(89)90264-3 (cited on p. 33).

[104] J. Deportes, D. Gignoux, and P. Givord. "Magnetic Properties of a $TmCo_2$ Single Crystal". In: *physica status solidi (b)* 64 (1974), pp. 29–32. DOI: 10.1002/pssb.2220640103 (cited on p. 33).

[105] M Patra et al. "Magnetocaloric effect in RAl_2 (R= Nd, Sm, and Tm): Promising for cryogenic refrigeration close to liquid helium temperature". In: *J. Alloys Compd.* 531 (2012), pp. 55–58. DOI: 10.1016/j.jallcom.2012.03.076 (cited on p. 33).

[106] Frank Stein and Andreas Leineweber. “Laves phases: a review of their functional and structural applications and an improved fundamental understanding of stability and properties”. In: *Journal of Materials Science* 56 (2021), pp. 5321–5427. DOI: 10.1007/s10853-020-05509-2 (cited on p. 33).

[107] Chao Zhou et al. “Unified understanding of the first-order nature of the transition in $TbCo_2$”. In: *Phys. Rev. B* 106 (2022). DOI: 10.1103/PhysRevB.106.064409 (cited on pp. 34, 85).

[108] Niraj K Singh et al. “Measurement of pressure effects on the magnetic and the magnetocaloric properties of the intermetallic compounds $DyCo_2$ and $Er(Co_{1-x}Si_x)_2$”. In: *J. Condens. Matter Phys.* 19.3 (2007), p. 036213. DOI: 10.1088/0953-8984/19/3/036213 (cited on p. 43).

[109] Niraj K. Singh et al. “Heat capacity and magnetoresistance in $Dy(Co,Si)_2$ compounds”. In: *J. Appl. Phys.* 97.10 (2005), 10A301. DOI: 10.1063/1.1844932 (cited on p. 43).

[110] T. Tohei and H. Wada. “Change in the character of magnetocaloric effect with Ni substitution in $Ho(Co_{1-x}Ni_x)_2$”. In: *J. Magn. Magn. Mater.* 280.1 (2004), pp. 101–107. DOI: 10.1016/j.jmmm.2004.02.026 (cited on p. 43).

[111] X. Q. Zheng et al. “Magnetic properties and magnetocaloric effects of $Gd_xEr_{1-x}Ga$ ($0 \leq x \leq 1$) compounds”. In: *J. Appl. Phys.* 115.17 (2014), 17A905. DOI: 10.1063/1.4854875 (cited on p. 43).

[112] J. Chen et al. “Giant magnetocaloric effect in HoGa compound over a large temperature span”. In: *Solid State Commun.* 150.3-4 (2010), pp. 157–159. DOI: 10.1016/j.ssc.2009.10.023 (cited on p. 43).

[113] J. Chen et al. “Large reversible magnetocaloric effect caused by two successive magnetic transitions in ErGa compound”. In: *Appl. Phys. Lett.* 95.13 (2009), p. 132504. DOI: 10.1063/1.3233925 (cited on p. 43).

[114] Zhao-Jun Mo et al. “Low field induced giant magnetocaloric effect in TmGa compound”. In: *Appl. Phys. Lett.* 103.5 (2013), p. 052409. DOI: 10.1063/1.4816729 (cited on p. 43).

[115] H. Zhang et al. “Large magnetocaloric effects of RFeSi (R = Tb and Dy) compounds for magnetic refrigeration in nitrogen and natural gas liquefaction”. In: *Appl. Phys. Lett.* 103 (2013), p. 202412. DOI: 10.1063/1.4832218 (cited on pp. 43, 75).

[116] Q. Y. Dong et al. “Large reversible magnetocaloric effect in DyCuAl compound”. In: *J. Appl. Phys.* 105.11 (2009), p. 113902. DOI: 10.1063/1.3122598 (cited on p. 43).

[117] Zhao-Jun Mo et al. “Low-field induced giant magnetocaloric effect in TmCuAl compound”. In: *Appl. Phys. Lett.* 102.19 (2013), p. 192407. DOI: 10.1063/1.4804576 (cited on p. 43).

[118] R. Rajivgandhi et al. “Effect of rapid quenching on the magnetism and magnetocaloric effect of equiatomic rare earth intermetallic compounds RNi (R = Gd, Tb and Ho)”. In: *J. Magn. Magn. Mater.* 433 (2017), pp. 169–177. DOI: 10.1016/j.jmmm.2017.03.011 (cited on p. 43).

[119] R. Rajivgandhi et al. “Effect of microstructure and texture on the magnetic and magnetocaloric properties of the melt-spun rare earth intermetallic compound DyNi”. In: *J. Magn. Magn. Mater.* 418 (2016), pp. 9–13. DOI: 10.1016/j.jmmm.2016.02.052 (cited on p. 43).

[120] Jinu Kurian et al. “Enhanced magnetocaloric effect in undercooled rare earth intermetallic compounds RNi (R = Gd, Ho and Er)”. In: *J. Magn. Magn. Mater.* 499 (2020), p. 166302. DOI: 10.1016/j.jmmm.2019.166302 (cited on p. 43).

[121] Z. Han et al. “Magnetocaloric effect in terbium diboride”. In: *J. Alloy. Compd.* 498.2 (2010), pp. 118–120. DOI: 10.1016/j.jallcom.2010.03.154 (cited on p. 43).

[122] Hui Meng et al. “Reversible magnetocaloric effect and refrigeration capacity enhanced by two successive magnetic transitions in DyB_2”. In: *Sci. China Technol. Sci.* 55.2 (2012), pp. 501–504. DOI: 10.1007/s11431-011-4684-6 (cited on p. 43).

[123] Q. Zhang et al. “Large reversible magnetocaloric effect in Tb_2In”. In: *Solid State Commun.* 149 (2009), pp. 396–399. DOI: 10.1016/j.ssc.2008.12.009 (cited on pp. 43, 75, 79).

[124] Q. Zhang et al. “Large reversible magnetocaloric effect in Dy_2In”. In: *J. Phys. D Appl. Phys.* 42.5 (2009), p. 055011. DOI: 10.1088/0022-3727/42/5/055011 (cited on p. 43).

[125] Q. Zhang et al. “Magnetocaloric effect in Ho_2In over a wide temperature range”. In: *Appl. Phys. Lett.* 94.18 (2009), p. 182501. DOI: 10.1063/1.3130090 (cited on p. 43).

[126] H. Zhang et al. “Large reversible magnetocaloric effect in Er_2In compound”. In: *J. Alloys Compd.* 509 (2011), pp. 2602–2605 (cited on pp. 43, 75, 79).

[127] V. K. Pecharsky and K. A. Gschneidner. “Gd-Zn alloys as active magnetic regenerator materials for magnetic refrigeration”. In: *Cryocoolers 10*. Ed. by R. G. Ross. Boston, MA: Springer US, 2002, pp. 629–637. ISBN: 978-0-306-46120-0. DOI: 10.1007/0-306-47090-X_75 (cited on p. 43).

[128] Xiangjie Wang et al. “Magnetic phase transitions and large magnetocaloric effects in equiatomic binary DyZn compound”. In: *J. Alloy. Compd.* 694 (2017), pp. 613–616. DOI: 10.1016/j.jallcom.2016.09.161 (cited on p. 43).

[129] Lingwei Li et al. “Magnetic phase transitions and large magnetic entropy change with a wide temperature span in HoZn”. In: *J. Alloy. Compd.* 643 (2015), pp. 147–151. DOI: 10.1016/j.jallcom.2015.04.146 (cited on p. 43).

[130] K. P. Shinde et al. “Magnetocaloric properties of TbN, DyN and HoN nanopowders prepared by the plasma arc discharge method”. In: *Dalton trans.* 44.47 (2015), pp. 20386–20391. DOI: 10.1039/c5dt03528g (cited on p. 43).

[131] Takashi Nakagawa et al. “Magnetocaloric effects of ferromagnetic erbium mononitride”. In: *J. Alloy. Compd.* 408-412 (2006), pp. 191–195. DOI: 10.1016/j.jallcom.2005.04.061 (cited on p. 43).

[132] J.Sánchez Marcos et al. “Heat capacity and magnetocaloric effect in polycrystalline and amorphous $GdMn_2$”. In: *J. Magn. Magn. Mater.* 272-276 (2004), pp. 579–580. DOI: 10.1016/j.jmmm.2003.11.225 (cited on p. 43).

[133] Wenliang Zuo et al. “Large reversible magnetocaloric effect in RMn_2 (R=Tb, Dy, Ho, Er) compounds”. In: *J. Alloy. Compd.* 575 (2013), pp. 162–167. DOI: 10.1016/j.jallcom.2013.03.185 (cited on p. 43).

[134] V. K. Pecharsky et al. “Magnetocaloric properties of Gd_3Al_2”. In: *Cryocoolers 10*. Ed. by R. G. Ross. Boston, MA: Springer US, 2002, pp. 639–645. ISBN: 978-0-306-46120-0. DOI: 10.1007/0-306-47090-X_76 (cited on p. 43).

[135] Hu Zhang et al. “Magnetic properties and magnetocaloric effect in Tb_3Al_2 compound”. In: *J. Alloy. Compd.* 615 (2014), pp. 406–409. DOI: 10.1016/j.jallcom.2014.06.209 (cited on p. 43).

[136] YaWei Li et al. “Successive magnetic transitions and magnetocaloric effect in Dy_3Al_2 compound”. In: *J. Alloy. Compd.* 651 (2015), pp. 278–282. DOI: 10.1016/j.jallcom.2015.08.087 (cited on p. 43).

[137] H. Zhang et al. “Giant magnetic refrigerant capacity in Ho_3Al_2 compound”. In: *Solid State Commun.* 152.13 (2012), pp. 1127–1130. DOI: 10.1016/j.ssc.2012.04.004 (cited on p. 43).

[138] Alessia Provino et al. “Gd_3Ni_2 and $Gd_3Co_xNi_{2-x}$: magnetism and unexpected Co/Ni crystallographic ordering”. In: *J. Mater. Chem. C* 4.25 (2016), pp. 6078–6089. DOI: 10.1039/C6TC01035K (cited on p. 43).

[139] A. Herrero et al. “Crystallographic, magnetic and magnetocaloric properties in novel intermetallic materials R_3CoNi (R = Tb, Dy, Ho, Er, Tm, Lu)”. In: *J. Alloy. Compd.* 865 (2021), p. 158948. DOI: 10.1016/j.jallcom.2021.158948 (cited on p. 43).

[140] Q. Y. Dong et al. “Magnetic properties and magnetocaloric effects in R_3Ni_2 (R = Ho and Er) compounds”. In: *Appl. Phys. Lett.* 99.13 (2011), p. 132504. DOI: 10.1063/1.3643142 (cited on p. 43).

[141] Y. I. Spichkin, V. K. Pecharsky, and K. A. Gschneidner. “Preparation, crystal structure, magnetic and magnetothermal properties of $(Gd_x,R_{5-x})Si_4$, where R=Pr and Tb, alloys”. In: *J. Appl. Phys.* 89.3 (2001), pp. 1738–1745. DOI: 10.1063/1.1335821 (cited on p. 43).

[142] V. V. Ivtchenko, V. K. Pecharsky, and K. A. Gschneidner. “Magnetothermal Properties of $Dy_5(Si_xGe_{1-x})_4$ Alloys”. In: *Advances in Cryogenic Engineering Materials*. Ed. by U. Balu Balachandran et al. Boston, MA: Springer US, 2000, pp. 405–412. ISBN: 978-1-4613-6926-4. DOI: 10.1007/978-1-4615-4293-3_52 (cited on p. 43).

[143] Niraj K. Singh et al. “Magnetic and magnetothermodynamic properties of Ho_5Si_4”. In: *J. Appl. Phys.* 107.9 (2010), 09A921. DOI: 10.1063/1.3365515 (cited on p. 43).

[144] Z. Arnold et al. “Magnetocaloric effect of Er_5Si_4 under hydrostatic pressure”. In: *Phys. Rev. B* 79.14 (2009). DOI: 10.1103/PhysRevB.79.144430 (cited on p. 43).

[145] K. W. Zhou et al. “Magnetocaloric effects in $(Gd_{1-x}Tb_x)Co_2$”. In: *Solid State Commun.* 137.5 (2006), pp. 275–277. DOI: 10.1016/j.ssc.2005.11.023 (cited on p. 43).

[146] T. Gottschall et al. “Magnetocaloric effect of gadolinium in high magnetic fields”. In: *Phys. Rev. B* 99 (2019), p. 1750. DOI: 10.1103/PhysRevB.99.134429 (cited on pp. 43, 45, 51, 52).

[147] M. D. Kuz’min and A. M. Tishin. “Magnetocaloric effect Part 2: magnetocaloric effect in heavy rare earth metals and their alloys and application to magnetic refrigeration”. In: *Cryogenics* 33.9 (1993), pp. 868–882. DOI: 10.1016/0011-2275(93)90101-S (cited on p. 43).

[148] E. P. Nóbrega et al. “The magnetocaloric effect in R_5Si_4 (R = Gd, Tb): a Monte Carlo calculation”. In: *J. Condens. Matter Phys.* 18.4 (2006), pp. 1275–1283. DOI: 10.1088/0953-8984/18/4/013 (cited on p. 43).

[149] Niraj K. Singh et al. “Effect of Tm substitution on the magnetic and magnetocaloric properties in the intermetallic compounds $(Tb_{1-x}Tm_x)Co_2$”. In: *J. Phys. D Appl. Phys.* 40.6 (2007), pp. 1620–1625. DOI: 10.1088/0022-3727/40/6/005 (cited on p. 43).

[150] H. Wada et al. “Magnetocaloric effects of Laves phase $Er(Co_{1-x}Ni_x)_2$ compounds”. In: *J. Alloy. Compd.* 316.1-2 (2001), pp. 245–249. DOI: 10.1016/S0925-8388(00)01305-0 (cited on p. 43).

[151] J. Kaštil et al. “Magnetic and magnetocaloric properties of partially disordered RFeAl (R = Gd, Tb) intermetallic”. In: *Intermetallics* 54 (2014), pp. 15–19. DOI: 10.1016/j.intermet.2014.05.008 (cited on p. 43).

[152] Tino Gottschall et al. “Contradictory role of the magnetic contribution in inverse magnetocaloric Heusler materials”. In: *Phys. Rev. B* 93 (2016). DOI: 10.1103/PhysRevB.93.184431 (cited on p. 45).

[153] J. S. Amaral, N.J.O. Silva, and V. S. Amaral. “Estimating spontaneous magnetization from a mean field analysis of the magnetic entropy change”. In: *J. Magn. Magn.* 322 (2010), pp. 1569–1571. DOI: 10.1016/j.jmmm.2009.09.024 (cited on p. 45).

[154] J. H. Belo et al. “On the Curie temperature dependency of the magnetocaloric effect”. In: *Appl. Phys. Lett.* 100 (2012), p. 242407. DOI: 10.1063/1.4726110 (cited on pp. 45, 52, 53).

[155] H. Oesterreicher and F. T. Parker. “Magnetic cooling near Curie temperatures above 300 K”. In: *J. Appl. Phys.* 55 (1984), pp. 4334–4338. DOI: 10.1063/1.333046 (cited on pp. 45, 50–53).

[156] A. S. Arrott. “Approximations to Brillouin functions for analytic descriptions of ferromagnetism”. In: *J. Appl. Phys.* 103 (2008), p. 07C715. DOI: 10.1063/1.2836337 (cited on p. 45).

[157] L. Pfeuffer et al. “Influence of the martensitic transformation kinetics on the magnetocaloric effect in Ni-Mn-In”. In: *Physical Review Materials* 4 (2020). DOI: 10.1103/PhysRevMaterials.4.111401 (cited on p. 45).

[158] M Földeàki, R Chahine, and TK Bose. “Magnetic measurements: A powerful tool in magnetic refrigerator design”. In: *J. Appl. Phys.* 77 (1995), pp. 3528–3537. DOI: 10.1063/1.358648 (cited on p. 46).

[159] PJ Von Ranke et al. “Influence of the crystalline electrical field on the magnetocaloric effect in the series RNi_2 (R= Pr, Nd, Gd, Tb, Ho, Er)”. In: *Phys. Rev. B* 63 (2001), p. 184406. DOI: 10.1103/PhysRevB.63.184406 (cited on pp. 47, 53).

[160] PO Ribeiro et al. “Magnetothermal properties of $Ho_{1-x}Dy_xAl_2$ (x= 0, 0.05, 0.10, 0.15, 0.25 and 0.50) compounds”. In: *J. Magn. Magn.* 544 (2022), p. 168705. DOI: 10.1016/j.jmmm.2021.168705 (cited on p. 47).

[161] Charles Kittel. *Introduction to solid state physics*. John Wiley & sons, inc, 2005 (cited on p. 47).

[162] V. Franco et al. “Field dependence of the magnetocaloric effect in Gd and $(Er_{1-x}\ Dy_x)Al_2$: Does a universal curve exist?” In: *Europhys. Lett.* 79 (2007), p. 47009. DOI: 10.1209/0295-5075/79/47009 (cited on p. 50).

[163] Michael D. Kuz’min, Manuel Richter, and Alexander M. Tishin. “Field dependence of magnetic entropy change: Whence comes an intercept?” In: *J. Magn. Magn.* 321 (2009), pp. L1–L3. DOI: 10.1016/j.jmmm.2008.07.004 (cited on p. 50).

[164] Julia Lyubina et al. “Magnetic field dependence of the maximum magnetic entropy change”. In: *Phys. Rev. B* 83 (2011), p. 111. DOI: 10.1103/PhysRevB.83.012403 (cited on p. 50).

[165] Qiao-Yan Dong et al. “Field dependence of the magnetic entropy change in typical materials with a second-order phase transition”. In: *J. Magn. Magn.* 319 (2007), pp. 56–59. DOI: 10.1016/j.jmmm.2007.04.030 (cited on p. 50).

[166] Carlos Romero-Muñiz et al. “Applicability of scaling behavior and power laws in the analysis of the magnetocaloric effect in second-order phase transition materials”. In: *Phys. Rev. B* 94 (2016). DOI: 10.1103/PhysRevB.94.134401 (cited on p. 50).

[167] Alejandro F. Manchón-Gordón et al. “Distribution of Transition Temperatures in Magnetic Transformations: Sources, Effects and Procedures to Extract Information from Experimental Data”. In: *Metals* 10 (2020), p. 226 (cited on p. 50).

[168] M. D. Kuz’min et al. “Magnetic field dependence of the maximum adiabatic temperature change”. In: *Appl. Phys. Lett.* 99 (2011), p. 012501. ISSN: 0003-6951. DOI: 10.1063/1.3607279 (cited on p. 51).

[169] Sergey Taskaev et al. “Magnetocaloric effect in $GdNi_2$ for cryogenic gas liquefaction studied in magnetic fields up to 50 T”. In: *J. Appl. Phys.* 127 (2020), p. 233906. DOI: 10.1063/5.0006281 (cited on p. 51).

[170] P.J von Ranke et al. “The influence of crystalline electric field on the magnetocaloric effect in the series RAl_2 (R=Pr,Nd,Tb,Dy,Ho,Er, and Tm)”. In: *J. Magn. Magn. Mater.* 226 (2001), pp. 970–972. DOI: 10.1016/S0304-8853(00)01162-8 (cited on p. 53).

[171] D Gielen and M Lyons. *Critical materials for the energy transition: Rare earth elements*. 2022. URL: https://www.%20irena.%20org/Technical-Papers (cited on pp. 55, 56).

[172] European Commission et al. *Study on the EU's list of critical raw materials (2020) : final report*. Publications Office, 2020. DOI: doi/10.2873/11619 (cited on p. 55).

[173] AA Yaroshevsky. "Abundances of chemical elements in the Earth's crust". In: *Geochemistry International* 44 (2006), pp. 48–55. DOI: 10.1134/S001670290601006X (cited on p. 55).

[174] J.M.D. Coey. "Perspective and Prospects for Rare Earth Permanent Magnets". In: *Engineering* (2019). DOI: 10.1016/j.eng.2018.11.034 (cited on p. 56).

[175] *Mineral commodity summaries 2022*. 2022. DOI: 10.3133/mcs2022 (cited on p. 56).

[176] Roland Gauß et al. *Rare Earth Magnets and Motors: A European Call for Action. A report by the Rare Earth Magnets and Motors Cluster of the European Raw Materials Alliance*. 2021. URL: https://fdocuments.net/document/rare-earth-magnets-and-motors-a-european-call-for-action.html?page=9 (cited on p. 57).

[177] M. V. de Souza, J. A. da Silva, and L. S. Silva. "Effect of spin reorientation on magnetocaloric and transport properties of $NdAl_2$". In: *J. Magn. Magn.* 421 (2017), pp. 184–188. DOI: 10.1016/J.JMMM.2016.06.079 (cited on p. 60).

[178] "Anomalous Schottky specific heat and structural distortion in ferromagnetic $PrAl_2$". In: *Phys. rev. lett.* 110 (2013), p. 186405. DOI: 10.1103/PhysRevLett.110.186405 (cited on p. 60).

[179] Arjun K. Pathak et al. "Low temperature crystal structure and magnetic properties of RAl_2". In: *J. Appl. Phys.* 115 (2014), 17E109. DOI: 10.1063/1.4859096 (cited on p. 60).

[180] Mahmud Khan, K. A. Gschneidner, and V. K. Pecharsky. "Magnetocaloric effects in $Er_{1-x}Tb_xAl_2$ alloys". In: *J. Appl. Phys.* 107.9 (2010), 09A904. ISSN: 0163-1829. DOI: 10.1063/1.3335590 (cited on p. 64).

[181] J. Ćwik et al. "Magnetocaloric prospects of mutual substitutions of rare-earth elements in pseudobinary $Tb_{1-x}Ho_xNi_2$ compositions (x = 0.25–0.75)". In: *J. Alloys. Compd.* 886 (2021), p. 161295. DOI: 10.1016/j.jallcom.2021.161295 (cited on pp. 64, 69).

[182] Yikun Zhang et al. "Exploration of the rare-earth cobalt nickel-based magnetocaloric materials for hydrogen liquefaction". In: *J. Mater. Sci. Technol.* 159 (2023), pp. 163–169. ISSN: 10050302. DOI: 10.1016/j.jmst.2023.04.001 (cited on p. 64).

[183] Yiyin Zhu et al. "Magnetocaloric effect of $(Er_xR_{1-x})Co_2$ (R=Ho, Dy) for magnetic refrigeration between 20 and 80K". In: *Cryogenics* 51 (2011), pp. 494–498. DOI: 10.1016/j.cryogenics.2011.06.004 (cited on p. 64).

[184] Pedro Baptista de Castro et al. “Enhancement of giant refrigerant capacity in $Ho_{1-x}Gd_xB_2$ alloys ($0.1 \leq x \leq 0.4$)”. In: *J. Alloys Compd.* (2021), p. 158881. ISSN: 09258388. DOI: 10.1016/j.jallcom.2021.158881 (cited on p. 64).

[185] G. Y. Lu et al. “Effect of Cu substitution on the type of magnetic phase transition and magnetocaloric effect in the $ErCo_{2-x}Cu_x$ compounds”. In: *J. Alloys Compd.* 906 (2022), p. 164343. ISSN: 09258388. DOI: 10.1016/j.jallcom.2022.164343 (cited on p. 64).

[186] I. S. Tereshina et al. “Effects of composition variation and hydrogenation on magnetocaloric properties of the $(Gd_{1-x}Tb_x)Ni$ (x = 0.1; 0.9) compounds”. In: *J. Magn. Magn.* 574 (2023), p. 170693. ISSN: 03048853. DOI: 10.1016/j.jmmm.2023.170693 (cited on p. 64).

[187] Galina Politova et al. “Investigation of Magnetocaloric Properties in the $TbCo_{2-H}$ System”. In: *Crystals* 12.12 (2022), p. 1783. DOI: 10.3390/cryst12121783 (cited on p. 64).

[188] V. B. Chzhan et al. “New Magnetic Materials Based on RNi Compounds for Cryogenic Technology”. In: *Tech. Phys. Lett.* 46.3 (2020), pp. 303–306. ISSN: 1063-7850. DOI: 10.1134/S1063785020030189 (cited on p. 64).

[189] V. B. Chzhan et al. “Influence of interstitial and substitutional atoms on magnetocaloric effects in RNi compounds”. In: *Mater. Chem. Phys.* 264 (2021), p. 124455. ISSN: 02540584. DOI: 10.1016/j.matchemphys.2021.124455 (cited on p. 64).

[190] S. A. Lushnikov, I. S. Tereshina, and V. N. Verbetskii. “Magnetic Properties of Hydrides of $RNi_{1-x}Si_x$ Compounds (R = Dy, Gd, x = 0.05, 0.02)”. In: *Phys. Solid State* 60.12 (2018), pp. 2517–2523. ISSN: 1063-7834. DOI: 10.1134/S1063783419010153 (cited on p. 64).

[191] A. I. Smarzhevskaya et al. “The Magnetocaloric Effect and Magnetic Transitions in Hydride Compounds: $GdNiH_{3.2}$ and $TbNiH_{3.4}$”. In: *Solid State Phenomena* 233-234 (2015), pp. 243–246. DOI: 10.4028/www.scientific.net/SSP.233-234.243 (cited on p. 64).

[192] WM Swift and WE Wallace. “Magnetic characteristics of laves phase compounds containing two lanthanides with aluminum”. In: *J. Phys. Chem. Solids* 29 (1968), pp. 2053–2061. DOI: 10.1016/0022-3697(68)90055-3 (cited on p. 66).

[193] Adil Murtaza et al. “Magnetocaloric effect in the vicinity of the magnetic phase transition in $NdCo_{2-x}Fe_x$ compounds”. In: *Phys. Rev. B* 101 (2020). DOI: 10.1103/PhysRevB.101.214427 (cited on p. 69).

[194] Peilin Dong et al. “Effect of Dy addition on magnetocaloric effect in $PrCo_2$ compound”. In: *Mater. Res. Express* (2019). DOI: 10.1088/2053-1591/ab455c (cited on p. 69).

[195] Q. M. Zhang et al. “Magnetic properties and magnetocaloric effect of the compound NdSi”. In: *Chin. Phys. B* 456 (2015), pp. 258–260. DOI: 10.1016/j.physb.2014.09.008 (cited on p. 69).

[196] Li-Chen Wang and Bao-gen Shen. “Magnetic properties and magnetocaloric effects of PrSi”. In: *Rare Metals* 33 (2014), pp. 239–243. DOI: 10.1007/s12598-014-0310-7 (cited on p. 69).

[197] X. Q. Zheng et al. “Large magnetocaloric effect of NdGa compound due to successive magnetic transitions”. In: *AIP Adv.* 8 (2018), p. 056425. DOI: 10.1063/1.5006506 (cited on p. 69).

[198] X. Q. Zheng et al. “Nearly constant magnetic entropy change and adiabatic temperature change in PrGa compound”. In: *J. Appl. Phys.* 115 (2014), 17A938. DOI: 10.1063/1.4868203 (cited on p. 69).

[199] Mahmud Khan, K. A. Gschneidner, and V. K. Pecharsky. “Spin reorientation transitions in $Ho_{1-x}Dy_xAl_2$ alloys”. In: *J. Appl. Phys.* 110 (2011). DOI: 10.1063/1.3662949 (cited on pp. 69, 73).

[200] F. Guillou et al. “Non-hysteretic first-order phase transition with large latent heat and giant low-field magnetocaloric effect”. In: *Nat. Commun.* 9 (2018), p. 2925. DOI: 10.1038/s41467-018-05268-4 (cited on pp. 73–75, 79).

[201] L. A. Gil et al. “Conventional and anisotropic magnetic entropy change in $HoAl_2$ ferromagnetic compound”. In: *J. Magn. Magn.* 409 (2016), pp. 45–49. DOI: 10.1016/j.jmmm.2016.02.085 (cited on p. 73).

[202] M. Forker et al. “Magnetic and electric hyperfine interactions in the rare-earth indium compounds R_2In studied by Cd111 perturbed angular correlations”. In: *Phys. Rev. B* 71 (2005). DOI: 10.1103/PhysRevB.71.094404 (cited on p. 73).

[203] Eduardo Mendive-Tapia et al. “First-order ferromagnetic transitions of lanthanide local moments in divalent compounds: An itinerant electron positive feedback mechanism and Fermi surface topological change”. In: *Phys. Rev. B* 101 (2020). DOI: 10.1103/PhysRevB.101.174437 (cited on pp. 73, 77).

[204] Anis Biswas et al. “Correlating Crystallography, Magnetism, and Electronic Structure Across Anhysteretic First-Order Phase Transition in Pr_2In”. In: *ECS J. Solid State Sci. Technol.* 11 (2022), p. 043005. DOI: 10.1149/2162-8777/ac611d (cited on pp. 73, 77).

[205] A. Bhattacharyya, S. Giri, and S. Majumdar. “Field induced sign reversal of magnetocaloric effect in Gd_2In”. In: *J. Magn. Magn. Mater.* 324 (2012), pp. 1239–1241. DOI: 10.1016/j.jmmm.2011.11.023 (cited on p. 75).

[206] J. Ćwik et al. “The influence of Er substitution on magnetic and magnetocaloric properties of $Dy_{1-x}Er_xCo_2$ solid solutions”. In: *Intermetallics* 19 (2011), pp. 1656–1660. DOI: 10.1016/j.intermet.2011.07.012 (cited on p. 75).

[207] F. W. Wang, X. X. Zhang, and F. X. Hu. “Large magnetic entropy change in $TbAl_2$ and $(Tb_{0.4}Gd_{0.6})Al2$”. In: *Appl. Phys. Lett.* 77 (2000), pp. 1360–1362. DOI: 10.1063/1.1290389 (cited on p. 75).

[208] Helen Gamari-Seale, T. Anagnostopoulos, and J. K. Yakinthos. “Magnetic characteristics of rare–earth indium R_2In (R =Y, Nd, Sm, Gd, Tb, Dy, Ho, Er, and Tm) intermetallic compounds”. In: *J. Appl. Phys.* 50 (1979), pp. 434–437. DOI: 10.1063/1.325629 (cited on p. 77).

Acknowledgement

I would like to thank **Prof. Dr. Oliver Gutfleisch** for supervising my Ph. D. and for giving me the opportunity to join the Functional Materials Group where I worked as a student worker in 2017, conducted my master thesis in 2018 and 2019, and later continued as a Ph.D. student till now. I found my passion in magnetism and had a wonderful time in the FM family.

Furthermore, I would like to thank **Prof. Dr. Hongbin Zhang, Prof. Dr. Heiko Wende, and Prof. Dr. Jochen Wosnitza**, who kindly agreed to be the referees for my doctoral thesis.

My special thanks go to my two dear direct supervisors **Dr. Konstantin Skokov** and **Dr. Franziska Scheibel**, and my dear collaborator **Dr. Tino Gottschall**. They were always ready to offer discussions, guidance, and help for my research.

I want to thank my dear Collaborators **Dr. Eduard Bykov** and **Marc Straßheim** and the rest members in Dresden High Magnetic Field Laboratory for helping with my research and my measurements during my stay in Dresden High Magnetic Field Laboratory.

I want to thank **Dr. Alex Aubert** for providing kind help for me during the ”difficult time” in my Ph.D..

Many thanks go to **Dr. Imants Dirba** for helping me with the XRD measurements.

I would like to thank **Dr. Fernando Maccari** for his kind help in the lab.

I thank **Nuno Fortunato** from the Theory of Magnetic Materials group for helping me with the theoretical calculations.

I would like to thank **Prof. Dr. Hongbin Zhang** for his supervision on theoretical calculations, and thank **Prof. Dr. Martin Sahlberg** for bringing me to the field of neutron diffraction.

Many thanks to all the members and former members of the Functional Materials Group for the wonderful and diverse time in Darmstadt. It was a great pleasure to work together with all of you.

My thanks go to the HelmholtzRSF Joint Research Group (Project No. HRSF-0045), the European Research Council (ERC) under the European Union’s Horizon 2020 research and innovation program (Grant No. 743116—Cool Innov), the DFG (Nos. SPP 1599 and CRC/TRR 270 “HoMMage” Project-No. 405553726-TRR 270), the Clean Hydrogen Partnership and its members within the framework of the project HyLICAL (Grant No. 101101461).

Last but not least, I want to thank my family and friends for giving me motivation and assistance particularly in difficult times.

List of publications

- S. Taskaev, V. Khovaylo, K. Skokov, **W. Liu**, E. Bykov, M. Ulyanov, D. Bataev, A. Basharova, M. Kononova, D. Plakhotskiy, M. Bogush, T. Gottschall, and O. Gutfleisch, *Magnetocaloric effect in $GdNi_2$ for cryogenic gas liquefaction studied in magnetic fields up to 50 T*, J. Appl. Phys. **127**, 233906 (2020)

- **W. Liu**, F. Scheibel, T. Gottschall, E. Bykov, I. Dirba, K. Skokov, and O. Gutfleisch, *Large magnetic entropy change in Nd_2In near the boiling temperature of natural gas*, Appl. Phys. Lett. **119**, 022408 (2021)

- E. Bykov, **W. Liu**, K. Skokov, F. Scheibel, O. Gutfleisch, S. Taskaev, V. Khovaylo, D. Plakhotskiy, C. Salazar Mejia, J. Wosnitza, and T. Gottschall, *Magnetocaloric effect in the Laves-phase $Ho_{1-x}Dy_xAl_2$ family in high magnetic fields*, Phys. Rev. Mater. **5**, 095405 (2021)

- **W. Liu**, E. Bykov, S. Taskaev, M. Bogush, V. Khovaylo, N. Fortunato, A. Aubert, H. Zhang, T. Gottschall, J. Wosnitza, F. Scheibel, K. Skokov, and O. Gutfleisch, *A study on rare-earth Laves phases for magnetocaloric liquefaction of hydrogen*, Appl. Mater. Today **29**, 101624 (2022)

- F. Scheibel, **W. Liu**, L. Pfeuffer, N. Shayanfar, A. Taubel, K. Skokov, S. Riegg, Y. Wu, and O. Gutfleisch, *Influence of Gd-rich precipitates on the martensitic transformation, magnetocaloric effect, and mechanical properties of Ni-Mn-In Heusler alloys - A comparative study*, J. Appl. Phys. **133**, 075104 (2023)

- **W. Liu**, T. Gottschall, F. Scheibel, E. Bykov, N. Fortunato, A. Aubert, H. Zhang, K. Skokov, and O. Gutfleisch, *Designing magnetocaloric materials for hydrogen liquefaction with light rare-earth Laves phases*, J. Phys. Energy **5**, 034001 (2023)

- E. Bykov, A. Karpenkov, **W. Liu**, M. Straßheim, T. Niehoff, K. Skokov, F. Scheibel, O. Gutfleisch, C. Salazar Mejía, J. Wosnitza, and T. Gottschall, *Magnetocaloric effect in the Laves phases RCo_2 (R= Er, Ho, Dy, and Tb) in high magnetic fields*, J. Alloy. Compd. **977**, 173289 (2024)

- **W. Liu**, T. Gottschall, F. Scheibel, E. Bykov, A. Aubert, N. Fortunato, B. Beckmann, H. Zhang, K. Skokov, and O. Gutfleisch, *A matter of performance & criticality: reviewing rare-earth-based magnetocaloric intermetallic compounds for hydrogen liquefaction* J. Alloy. Compd. **995**, 174612 (2024)

- **W. Liu**, F. Scheibel, N. Fortunato, I. Dirba, T. Gottschal, H. Zhang, K. Skokov, and O. Gutfleisch, *Role of Debye temperature in achieving large adiabatic temperature changes at cryogenic temperatures: a case study on Pr_2In* Phys. Rev. B **109**, L140407 (2024)

List of Figures

List of Tables

Nomenclature

χ	Magnetic susceptibility
ΔH	Change of magnetic field
ΔM	Change of Magnetization
ΔS_t	Total isothermal entropy change
ΔS_e	Electronic entropy change
ΔS_H	Isofield magnetic entropy
ΔS_L	Lattice entropy change
ΔS_{tot}	Total entropy change
ΔS_T	Isothermal magnetic entropy
ΔT_{ad}	Adiabatic temperature change
δ_{FWHM}	full width at half maximum
η	materials efficiency
γ	Electronic specific heat coefficient
$\hat{H}$	Hamiltonian operator
$\hat{J}$	Angular momentum operator
$\hat{M}$	Atom magnetic moment operator
μ_B	Bohr magneton
μ_o	Vacuum permeability

μ_{eff}	Effective magnetic moment
$\overrightarrow{H}$	Vector of magnetic field
$\overrightarrow{L}$	Angular momentum
$\overrightarrow{S}$	Spin
ρ	mass density
C'	Heat capacity
C_e	Electronic heat capacity
C_H	Magnetic heat capacity
C_L	Lattice heat capacity
C_p	Isobaric heat capacity
C_{tot}	Total heat capacity
E_n	Eigenvalue of the Hamiltonian $\hat{H}$
F	Free energy
G	Gibbs free energy
G	de Gennes factor
g_J	Landé g-factor
H	Magnetic field
J	Total magnetic momentum number
K	Thermal conductance
k_B	Boltzmann constant
L	Azimuthal quantum number
M	Specific magnetization

m	Magnetization
M_J	magnetic moment of an atom
M_R	Molecular mass
N	Number of atoms
N_A	Avogadro Number
n_w	Weiss coefficient
P	Power
p	Pressure
Q	Heat
Q_{REV}	transferable heat
RC	Refrigerant capacity
RCP	Relative cooling power
S'	Entropy
S	Spin quantum number
S_e	Electronic entropy
S_L	Lattice entropy
S_M	Magnetic entropy
S_{tot}	Total entropy
T	Temperature
T_C	Curie temperature
T_D	Debye temperature
TEC	Temperature averaged entropy change
U	Internal energy

W Work

Z Partition function